Seasonal Variations in Saturn's Plasma between the Main Rings and Enceladus

---

A Dissertation

Presented to

the faculty of the School of Engineering and Applied Science

University of Virginia

---

in partial fulfillment

of the requirements for the degree

Doctor of Philosophy

by

Meredith K Elrod

December

2012

APPROVAL SHEET

The dissertation

is submitted in partial fulfillment of the requirements

for the degree of

Doctor of Philosophy

Meredith K Elrod

AUTHOR

The dissertation has been read and approved by the examining committee:

Robert E. Johnson

Advisor

Raul Baragiola

Phil Arras

Anne Verbiscer

H. Todd Smith

Frank Crary

Accepted for the School of Engineering and Applied Science:

Dean, School of Engineering and Applied Science

December

2012

Abstract

The region of Saturn's magnetosphere from the main rings to inside the orbit of Enceladus is populated by oxygen from the ring atmosphere and water products from Enceladus. Therefore, I examined Cassini Plasma Spectrometer (CAPS) data from several equatorial periapsis passes from 2004 to 2012 in the region from 2.4 to 3.8 Saturn radii (~60,300 km) including Voyager 2 in order to separate the contributions from these two sources and to understand the temporal variations in the plasma. Because of the high background signal in this region, only eight orbits were applicable to this study. Using these data, I found large variations in ion density, temperature, and composition. Although the Enceladus plumes may vary by up to a factor of four, I propose that the two orders of magnitude change in the ion density from 2004, at solstice, to 2010, near equinox, was due to the seasonal variation in the ring atmosphere [*Elrod et al.*, 2012]. Furthermore, when I compared the recent 2012 passes with the 2010 passes, I found an increase in ion count rates between 2010 and 2012 possibly consistent with a seasonal variation. However, since the 2012 pass was closer to Enceladus, it is possible that the resulting increase was due to the Enceladus neutral torus. Therefore, later passes closer to the northern hemisphere solstice will be required to confirm that the observed variations are primarily seasonal. My interpretation of the plasma data is supported by our model describing the seasonal variations and plasma chemistry of the O_2 atmosphere generated from the main rings [*Tseng et al.,* 2010; 2012].

This dissertation is dedicated in memoriam to Ron Elrod (1943 – 2008).

My Father, who kept hoping I would figure things out.

Table of Contents

List of Figures

List of Acronyms and Symbols

List of Acronyms Used:

- CAPS Cassini Plasma Spectrometer
- CDA Cosmic Dust Analyzer
- CIRS Composite Infrared Spectrometer
- INMS Ion Neutral Mass Spectrometer
- ISS Imaging Science Subsystem
- MAG Magnetometer
- MIMI Magnetospheric Imaging Instrument
- RPWS Radio and Plasma Wave Science
- UVIS Ultraviolet Imaging Spectrograph
- VIMS Visible and Infrared Mapping Subsystem
- Rs Saturn Radius
- SOI Saturn Orbit Insertion
- ELS Electron Spectrometer
- IBS Ion Beam Spectrometer
- IMS Ion Mass Spectrometer
- SNG Singles
- TOF Time of Flight
- MCP Micro Channel Plate
- W/W^+ Water group (O, OH, H_2O-Neutrals)/(O^+, OH^+, H_2O^+, H_3O^+-Ions)

List of Symbols Used:

- *BKGD* Background fit parameter
- *dt* time step for 1 A-cycle
- *Eff* Efficiency of the CAPS detector
- G_E Geometric Factor of the CAPS detector
- V_E Velocity of the ion in the detector
- *f* Maxwellian distribution function of the ions
- *n* Ion density (subscripted with i, 0, O+, O2+)
- *T* Ion temperature (subscripted, with i, 0 O+, O2+)
- *U* Plasma flow velocity (subscripted with 1, 2, and 3)

- m_i Mass of ion
- k Boltzmann Constant
- E Ion energy
- X^2 Chi squared determined from least squared algorithm
- V_{co} Corotation velocity
- R Radial distance
- ω Saturn Orbital period
- V_{phi_sc} Spacecraft velocity in phi (plasma flow) direction
- V_{orb} Keplerian orbital velocity
- T_{pick} Pick up temperature of ions
- $T_{\backslash\backslash}$ Parallel temperature (along field line)
- T_L Perpendicular temperature (in gyromotion)
- *Vsc* Spacecraft velocity (subscripted with 1, 2, 3)
- C Singles counts
- B Leading constants (term for simplification) $B = dt*Eff*G_E$
- a *Sqrt(2kT/m)* (term for simplification)
- x dummy variable for integration
- Ω solid angle of integration
- V_{max} maximum velocity
- C_{max} maximum counts
- M *U/a* (term for simplification)
- S_i Ionization source rate
- L_i Ionization loss rate
- H_i Scale height
- z Distance from the magnetic equator
- N_i Ion column density

Section 1: Introduction

Section 1.1—Introduction: Background

1] The Cassini Spacecraft launched in 1997, arrived at Saturn July 1, 2004, and is scheduled to be in orbit around Saturn collecting data until mid 2017. The goal of the mission is to create a picture of the Saturn system, from the planet and complex ring system to the numerous and varied moons. Cassini carries 12 major science systems: Cassini Plasma Spectrometer (CAPS), Cosmic Dust Analyzer (CDA), Composite Infrared Spectrometer (CIRS), Ion and Neutral Mass Spectrometer (INMS), Imaging Science Subsystem (ISS), Magnetometer (MAG), Magnetospheric Imaging Instrument (MIMI), Radar, Radio and Plasma Wave Science Instrument (RPWS), Radio Science Subsystem (RSS), Ultraviolet Imaging Spectrograph (UVIS), and Visible and Infrared Mapping Spectrometer (VIMS). These instruments work together to create a complete picture of the Saturn system. While this thesis focuses on data taken from the CAPS instrument, a subsystem designed to examine thermal ions and electrons in the magnetosphere, and data taken from several other subsystems are used in the science described in this project.

2] One major aspect of the Cassini mission is to map the neutral and ion composition throughout Saturn's complex magnetosphere. In order to examine the composition of the ions in this magnetosphere, it is necessary to consider the role that the rings and moons play as particle sources and sinks. Fig. 1.1 provides a diagram of the icy moons as well as the major rings of Saturn in the inner magnetosphere.

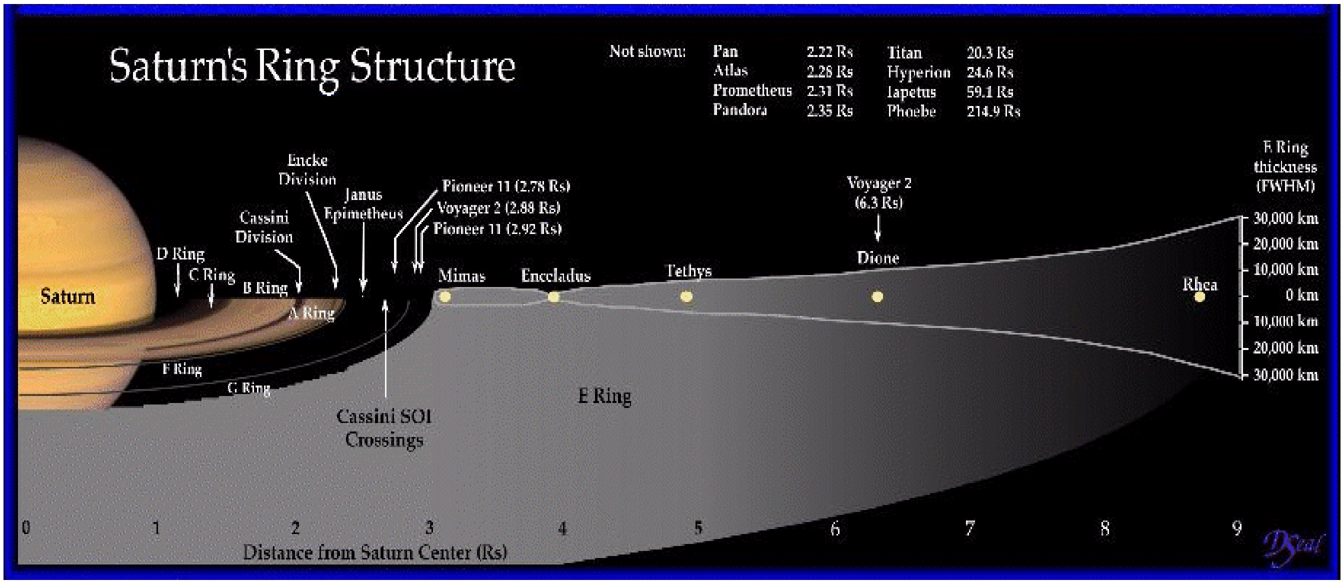

Figure 1.1—Schematic of Saturn's major rings and major moons in the inner magnetosphere inside 9 Rs. Included in this diagram are the locations where the spacecraft that have visited Saturn crossed the ring plane. The region of interest in my thesis is between the main rings at 2.2 Rs out to the orbit of Mimas, to around 3.8 Rs.

3] The inner magnetosphere of Saturn is often defined as the region from the surface of the planet to approximately 9 Rs (1 Rs = 1 Saturn Radius ≈ 60,300 km), as shown in Fig. 1.1. However, this thesis focuses on a smaller region of this inner magnetosphere, specifically from the outer edges of the main rings, around 2.2 Rs, to just inside the orbit of the icy moon Enceladus, around 3.8 Rs. In order to study this region, I carried out the first detailed analysis of the CAPS ion data in this region. Within this region are the optically thin F and G rings, the mid-sized icy moon Mimas, and two small moons at ~2.51 Rs, Janus and Epimetheus, which share a ring and an orbit. Amongst these major rings and moons, are several other smaller moons and rings that could also influence the plasma in this region. In addition to these distinct features, dust and very small ice grains, predominantly from the E-ring, permeate this region. While not optically thick, this ice and dust can have an influence on the lifetime of the plasma particles formed. Another important feature of this region is the prevailing penetrating radiation that affects Cassini's ability to detect ions and electrons. This radiation is further discussed in section 2.

Section 1.2—Previous Findings

4] One of the early discoveries made when the Cassini Spacecraft first entered orbit about Saturn, passing directly over the main rings, was a strong O_2^+ and O^+ signature [*Tokar et al.,* 2005]. The detection of both O_2^+ and O^+ ions over the main rings suggested a source of neutral O_2 forming a 'ring atmosphere' [*Johnson et al.,* 2006a]. Solar UV photons can interact with the ice particles in the main rings to photo-decompose the water, producing O_2 and H_2. The H_2, being lighter, will tend to be more spread out; the O_2 being heavier forms a more dense atmosphere that is confined to within ~0.08 Rs, or ~4800 km of the ring plane. Because in the ring atmosphere model the O_2 is produced by solar photons and the angle of the ring plane to the solar flux varies over the course of Saturn's orbit around the Sun, the density of this 'ring-atmosphere' was predicted to vary seasonally [*Tseng et al.,* 2010, 2012]. With a seasonally varying neutral source, there should be a seasonally varying density of ions in the region near the rings [*Elrod et al.,* 2012; *Johnson et al.,* 2005b]. Such a change should be reflected in the density of the ions detected by the CAPS instrument.

5] Another relevant discovery made by the Cassini spacecraft is that Saturn's small moon, Enceladus, has water plumes emanating from its southern polar region. The gas emitted from these plumes influences most of Saturn's magnetosphere [*Porco et al.* 2006]. These plumes are the source of the tenuous E-ring and a torus of water molecules whose dissociation products extend over a huge region around Enceladus' orbital path and were detected prior to Cassini's arrival at Saturn using the Hubble Space Telescope [*Jurac et al.,* 2001]. Although direct production of O_2 by the water molecules emitted from Enceladus is very low, the water products are spread far enough to interact with the ice particles in the A-ring. These radicals then can interact with the ice grains contributing to the formation of the O_2 ring atmosphere [*Tseng and Ip*, 2011].

6] These two major discoveries, affecting the plasma properties between the edge of the main rings at about 2.4 Rs to approximately 3.8 Rs, are the main focus of this thesis. The oxygen 'ring atmosphere' was shown to be a source for the oxygen observed in the upper atmosphere of Saturn [*Luhmann et al*., 2006; *Moses et al.*, 2000b] and a strong source for the oxygen neutrals scattered into the inner magnetosphere, where they can be ionized and contribute to Saturn's plasma [*Bouhram et al*., 2006; *Elrod et al.,* 2012; *Johnson et al*., 2006a; *Luhmann et al*., 2006; *Martens et al.,* 2008;*Tseng et al.*, 2010, 2012]. The Enceladus plumes are also a significant source of water group neutrals (O, OH, and H_2O) here referred to as W, and the associated water group ions (O^+, OH^+, H_2O^+, and H_3O^+) here referred to as W^+, throughout the magnetosphere including the region from 2.4 to 3.8 Rs. *Farmer* [2009] and *Cassidy and Johnson.* [2010] showed that the neutrals from the plumes have a broad distribution of predominately O and OH throughout the magnetosphere (including the region of interest), and *Smith et al.* [2010] showed that the plume source rates could vary by up to a factor of four, although such variability has not been observed in the UV data [*Hansen et al.* 2011]. Using these modeling efforts, I interpreted the CAPS data in this region.

Section 1.3—Data and Orbits Used

7] I analyzed data from the Cassini Plasma Spectrometer (CAPS) spanning several years and the Voyager 2 Plasma Science Instrument (PLS). When Voyager 2 flew by Saturn in 1982, Saturn was near equinox. The data obtained from several Cassini orbits are from 2004, near southern solstice, through 2007 and 2010 near equinox and finally to 2012 when the sun passed to the northern side of the rings. Northern solstice will occur in 2017 near the end of the Cassini mission.

8] In Fig. 1.2, I show the orbits used for this study. Because of the high amount of penetrating radiation and the icy material in this region, there are few passes of the spacecraft with a periapsis lower than 3.5 Rs that are useful for the CAPS instrument. Between the need for good pointing, and the high background levels in the region, the number of useable passes between Saturn Orbit Insertion (SOI) in 2004 to 2012 was reduced to eight.

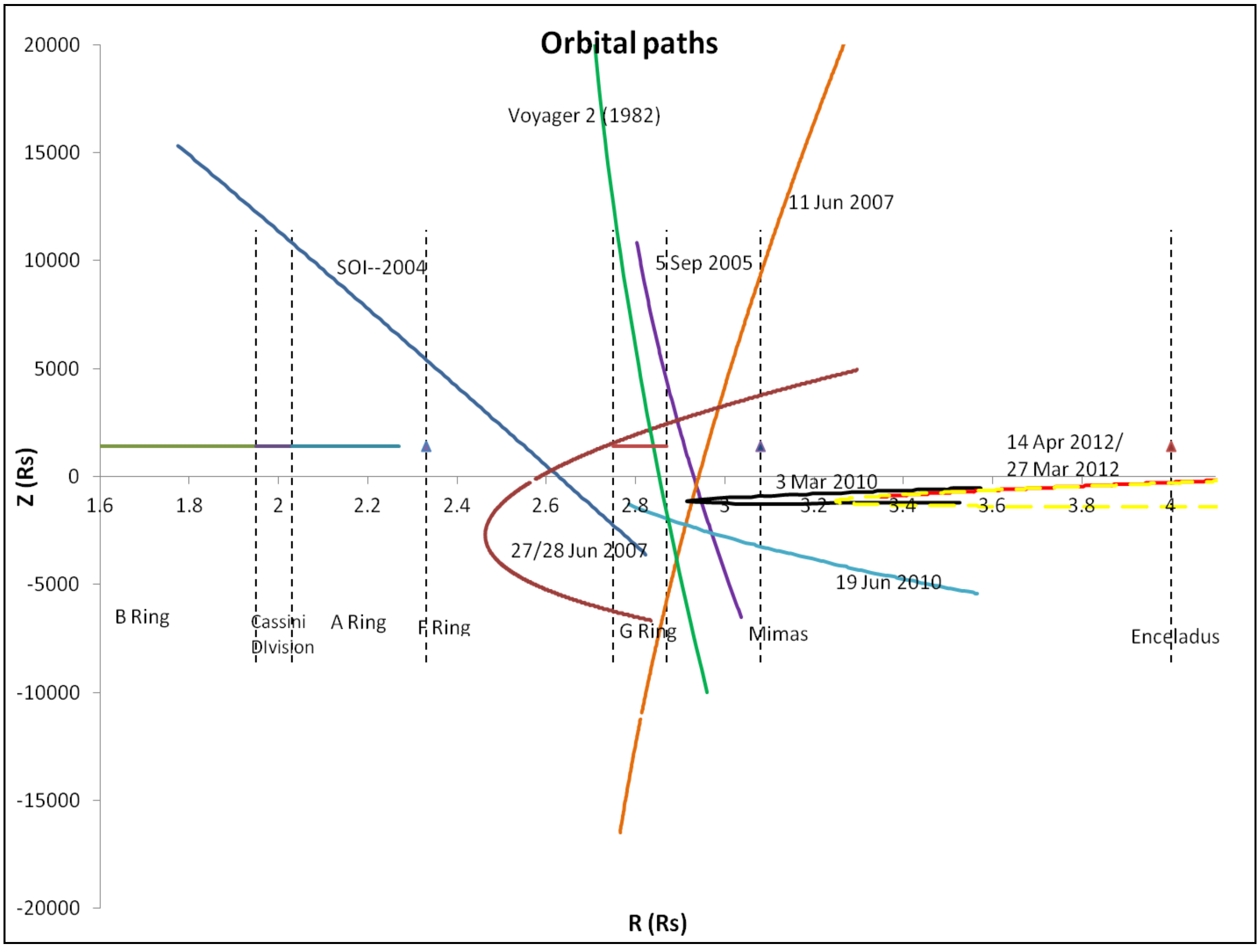

Figure 1.2—Orbits of the data used in this study. All orbits are plotted as a cross-sectional view of the R vs. Z plane. The B-ring, Cassini Division, A-ring, F-ring, G-ring, Mimas, and Enceladus are marked with vertical dashed lines for reference.

Table 1.1—Orbital Data for all passes used in this study

Date (DOY)	Time (Spacecraft) (A-cycles)[1]	Solar Zenith Angle	Solar Activity level	Approximate Ring Temperature
SOI[2] July 2004 (183)	04:15 – 04:44 (479-532)	~24° S (solstice)	Average	~100 K
5 Sept 2005 (284)	10:19-11:04 (963-1047)	~14° S	Low	~75 K
11 June 2007 (162)	22:30-0:00 (2521-2686)	~10° S	Low	~65 K
27 & 28 June 2007 (178/179)	22:22-02:09 (2511-2700, 1-235)	~9° S	Low	~60 K
3 March 2010 (062)	07:19-08:30 (823-957)	~5° N (equinox)	Low	~60 K
19 March 2010 (170)	04:08-5:44 (465-644)	~6° N	Low	~60 K
27 March 2012 (087)	06:00 – 08:32 (2029 – 2312)	~16°N	Average	Not Available
14 April 2012 (105)	14:29 – 23:27 (1419-2639)	~16°N	Average	Not Available
Voyager 2 (1982)	** Ring plane crossing data	~6° N (equinox)	High	**not measured

Solar activity levels found from the Virtual Solar Observatory website [*VSO*]. Approximate ring temperatures derived from CIRS temperatures [*Flandes et al.,* 2010]. Axial tilt angle determined based on determinations of equinox and Saturn's orbital period. Solar activity is returning back to normal during 2011. Voyager 2 data: [*Richardson,* 1986].

[1] An A-cycle is the 32 second instrument collection cycle. Time is the start time of the A-cycle in seconds from J2000 (barycentric dynamic time) converted into a readable format of HH:MM:SS

[2]SOI settings on CAPS slightly different for this pass due to thrusters firing.

9] In early 2011, CAPS experienced a brief period where a short in the instrument required that the system be shut down for several months. After much deliberation between operations at NASA and JPL, it was determined safe to resume operations, and the instrument was turned back on in February of 2012. From February through June of 2012, operations continued as normal until another short occurred that was detectable in the data and the instrument was turned off again. At the time of publication there is no known time for resuming operations. However, future data, if possible could add insight to the seasonal variations in the plasma, as the spacecraft will continue to pass through the region of interest in 2014, 2015 and directly over the main rings near the end of mission in 2016/2017.

Section 1.4—Thesis Statement

10] The photo-produced ring atmosphere was predicted to vary seasonally since the source rate of the neutrals depends on the incident angle of sunlight with the rings and on ring particle temperatures [*Tseng et al.*, 2010, 2012]. Since the extended ring atmosphere is a source of ions for this region, examination of plasma data from 2004, when the Sun was near southern solstice, through 2007 and 2010, as the incident angle decreased toward equinox (August 2009), could reflect the changing source rate (see Table 1.1). Although the Enceladus source rate may or may not be variable [*Smith et al.*, 2010; *Hansen et al.*, 2011], it does not appear to exhibit a seasonal dependence. However, water products from Enceladus deposited on the particles in the A, F, and G rings can enhance the production of O_2 neutrals. [*Tseng et al.*, 2010; 2012, *Tseng & Ip*, 2011].

11] In this thesis I examined the plasma parameters, density, temperature, composition, and bulk flow velocity, detected by CAPS and by the Voyager 2 plasma instrument and compare these results with the models of the distribution of the neutrals throughout this region since the neutrals are the ion sources. As a result I discovered a significant drop in the densities and temperatures of the ions measured between the solstice and equinox. The composition varies such that O_2^+ is dominant at SOI but the W^+ ions dominate closer to Enceladus. I first describe the instrument and my analysis techniques in section 2, then describe the resulting plasma properties in section 3, and finally discuss the results in relation to the published models in section 4 [*Cassidy and Johnson,* 2010; *Smith et al.,* 2010; *Tseng et al.,* 2010; 2012], In section 4 I also describe how my results indicate that there is a seasonal variation in the plasma density in the region between 2.4 and 3.6 Rs. Since this region is filled with many small moons, rings, and ice and dust particles that are affected by the O_2^+ and W^+ ions, my study of the temporal effects on the plasma will help us better understand those process affecting the evolution of the ring particles and surfaces of the moons.

Section 2: CAPS Instrument, Fitting Method, and Background Influences

Section 2.1—CASSINI PLASMA SPECTROMETER

12] The CAPS instrument is primarily responsible for the detection and measurement of thermal plasma ions and electrons while in orbit around Saturn. It is equipped with an Electron Spectrometer (ELS), an Ion Beam Spectrometer (IBS), and an Ion Mass Spectrometer (IMS), which can utilize a Singles (SNG) method of ion detection as well as a time-of-flight (TOF) measurements. This study uses the SNG capability of the IMS, which creates a single count for each ion that enters the IMS sensor and generates a signal, irrespective of whether it creates a start-stop signal pair in the time-of-flight. The SNG function of the CAPS instrument can, in principle, be used to determine the densities, temperatures, and plasma flow velocity of various ion species if the ion mass and charge are known. The ion results analyzed here are compared to the total electron densities determine using Radio Wave Plasma Science (RPWS) data, a separate Cassini instrument.

13] The Ion Mass Spectrometer has eight entrance channels and corresponding eight anodes that open out at 8.3° x 20° each see Table 2.1, giving the instrument an instantaneous Field of View (FOV) of 8.3° x 160° [*Young et al.*, 2004]. The instrument can actuate over the sky for <200° sweep. Fig. 2.2 provides a schematic of the CAPS instrument full field of view including portions where other parts of the Cassini spacecraft block the incoming ions.

TABLE I
CAPS sensor performance summary.

Parameter	IMS Med. Res.	IMS High Res.	ELS	IBS
Energy/charge response				
Range (eV/e)	1–50,280		0.6–28,750	1–49,800
Resolution $(\Delta E/E)_{FWHM}$	0.17		0.17	0.014
Angular response				
Elevation sectors (number)	8		8	3
Instantaneous FOV $(AZ \times EL)_{FWHM}$	$8.3^\circ \times 160^\circ$		$5.2^\circ \times 160^\circ$	$1.4^\circ \times 150^\circ$
Angular resolution $(AZ \times EL)_{FWHM}$	$8.3^\circ \times 20^\circ$		$5.2^\circ \times 20^\circ$	$1.4^\circ \times 1.5^\circ$
Mass/charge response				
Range (amu/e)	$1 \sim 400$	$1 \sim 100$	–	–
Resolution $(M/\Delta M)_{FWHM}$	8	60	–	–
Energy-geometric factor* (cm^2 sr eV/eV)	5×10^{-3}	5×10^{-4}	1.4×10^{-2}	4.7×10^{-5}
Temporal response				
Per sample (s)	6.25×10^{-2}		3.125×10^{-2}	7.813×10^{-3}
Energy-elevation (s)	4.0		2.0	2.0
Energy-elevation-azimuth (s)			180	

*Applies to total field-of-view and includes efficiency factors.

Table 2.1—Table of CAPS Instrument resolution and Field of View. [*Young et al.,* 2004]

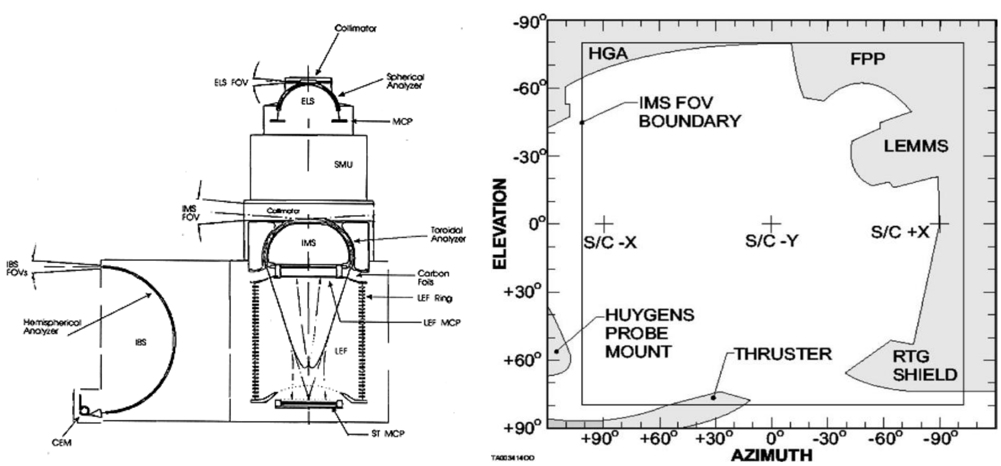

Figure 2.1—CAPS schematic (left) and Field of View of the IMS (right). [*Young et al.,* 2004]

14] The potential voltage used to accelerate the ions into the detector, is varied from 0 to ~8 kV, corresponding to transmitted particle energies of 1 to 50,000 eV, over 63 energy bins with bin 64 as a re-set energy bin. Each sweep of 64 energy bins takes 4 seconds; a set of eight sweeps totaling 32 seconds is defined as an A-cycle. At the beginning of each day the first 32 second A-cycle is labeled as 1 and the rest are numbered sequentially throughout the day. Depending on the telemetry mode of the spacecraft, the singles counts are summed up to 1, 2, 4, or all 8 sweeps per A-cycle. As a result each A-cycle may return a different number of sweeps based on data needs. Therefore to maintain consistency throughout my study, I summed up the data to A-cycle resolution. In other words, I summed up all sweeps within an A-cycle, as is discussed in the fit procedure.

15] In order to determine plasma parameters (density, composition, temperature, and bulk velocity), it is typically assumed that the ions have a flow speed superimposed on an approximate Maxwellian energy distribution. The thermal plasma ion temperature is such that the ions are predominately singly charged [*Young et al.*, 2004], so that the mass per charge ratio can be used to give the mass of the ion detected. From the measured energy spectrum, the ion density, the temperature and the flow velocity can be extracted. Two examples of a single sweep through the 63 bins, one at a point above the rings and one near the rings from the SOI pass, are shown in Fig. 2.2.

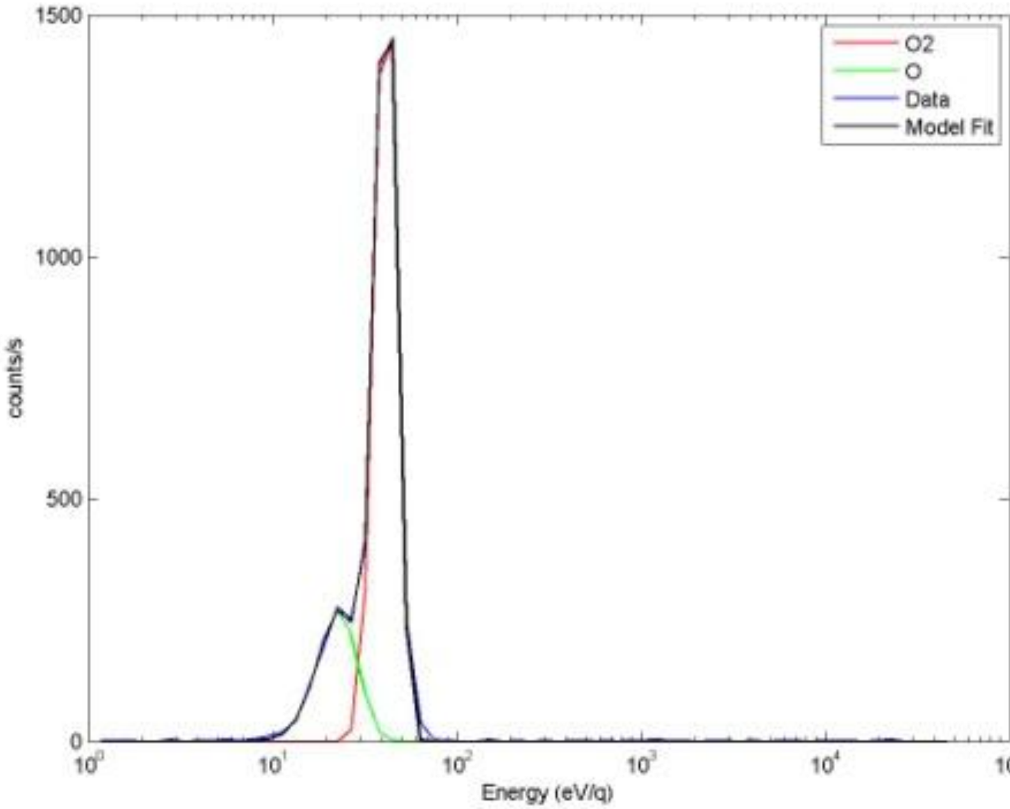

345 (a)

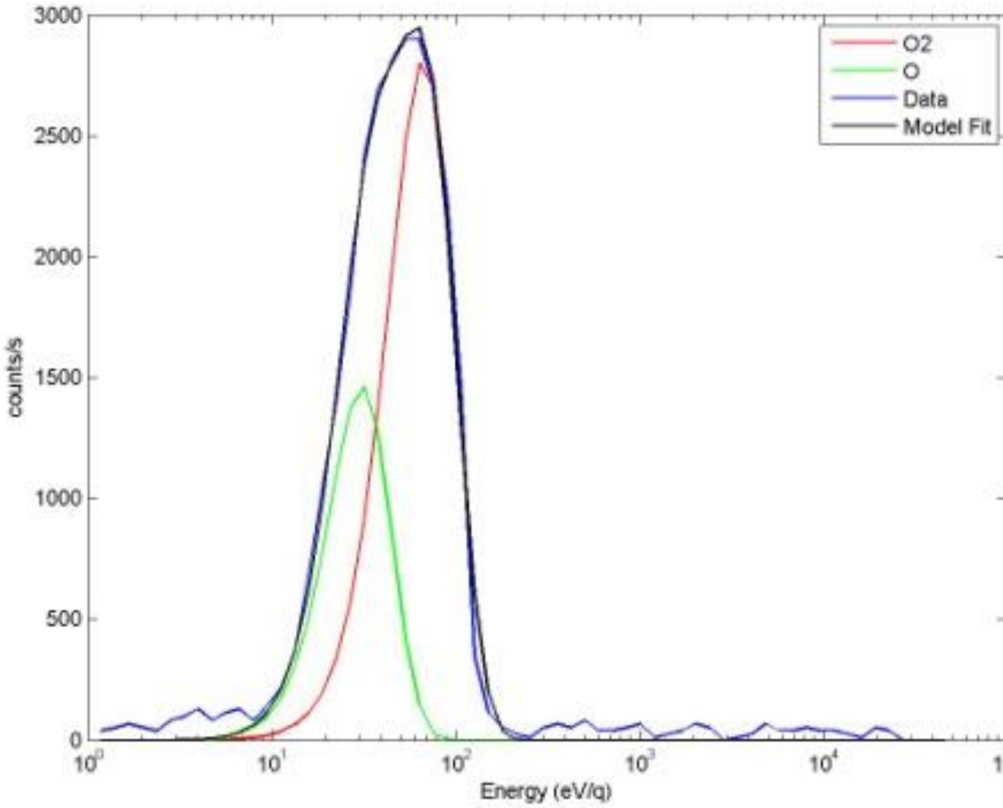

(b)

Figure 2.2— Example sweeps of Singles data with the model fit (section 2.4) of anode 3 (a) and anode 7 (b) from the two points during the SOI pass. (a) A spectrum of counts/s versus energy at time UT 03:46 and at 1.94 Rs directly over the Cassini Division in the main rings. The spectrum in (a) clearly shows two separate peaks at two different energies, which are well fit by Maxwellian energy distributions and the appropriate corotation energies revealing the presence of O_2^+ and O^+(32 amu/e and 16 amu/e). (b) A spectrum of counts/s versus energy at time UT 04:18 and at 2.41 Rs just past the F ring. The two contributions are not as distinct and the broader peak is skewed, strongly suggestive of the presence of water group ions in addition to O_2^+.

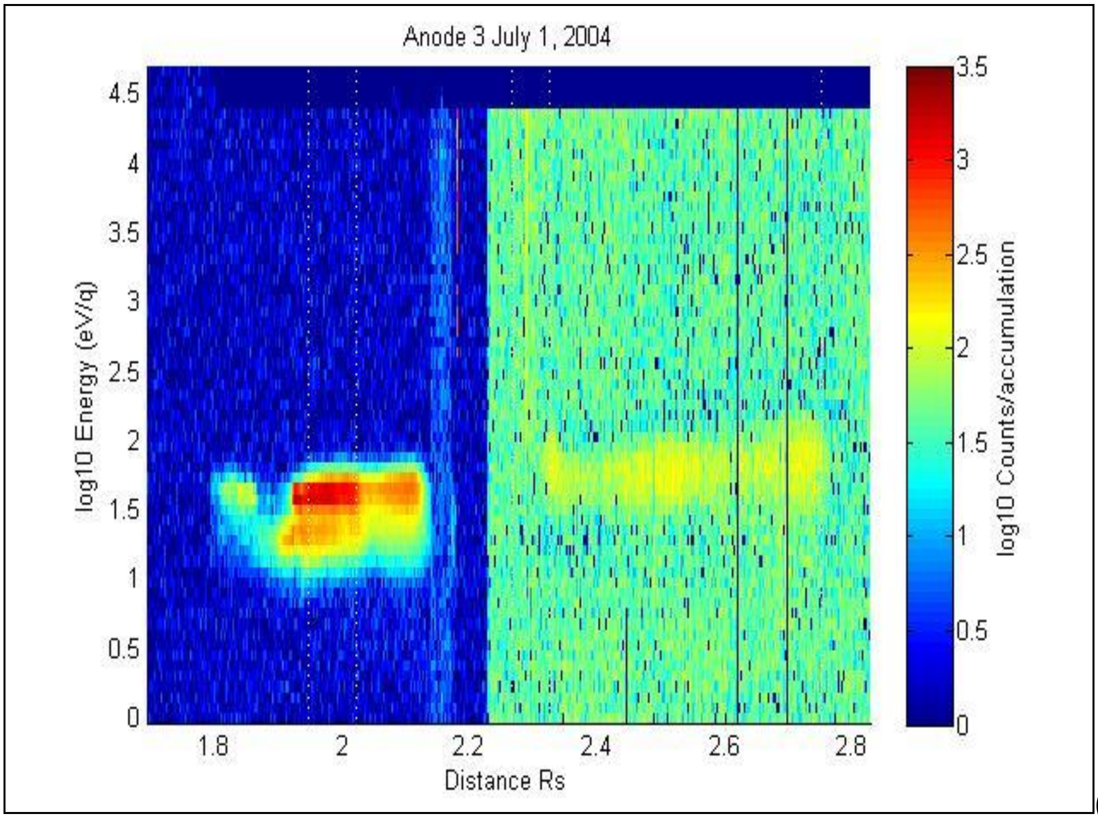
Anode 3 July 1, 2004
log10 Energy (eV/q)
4.5
4
3.5
3
2.5
2
1.5
1
0.5
0
1.8
2
2.2
2.4
2.6
2.8
Distance Rs
log10 Counts/accumulation
3.5
3
2.5
2
1.5
1
0.5
0
(a)

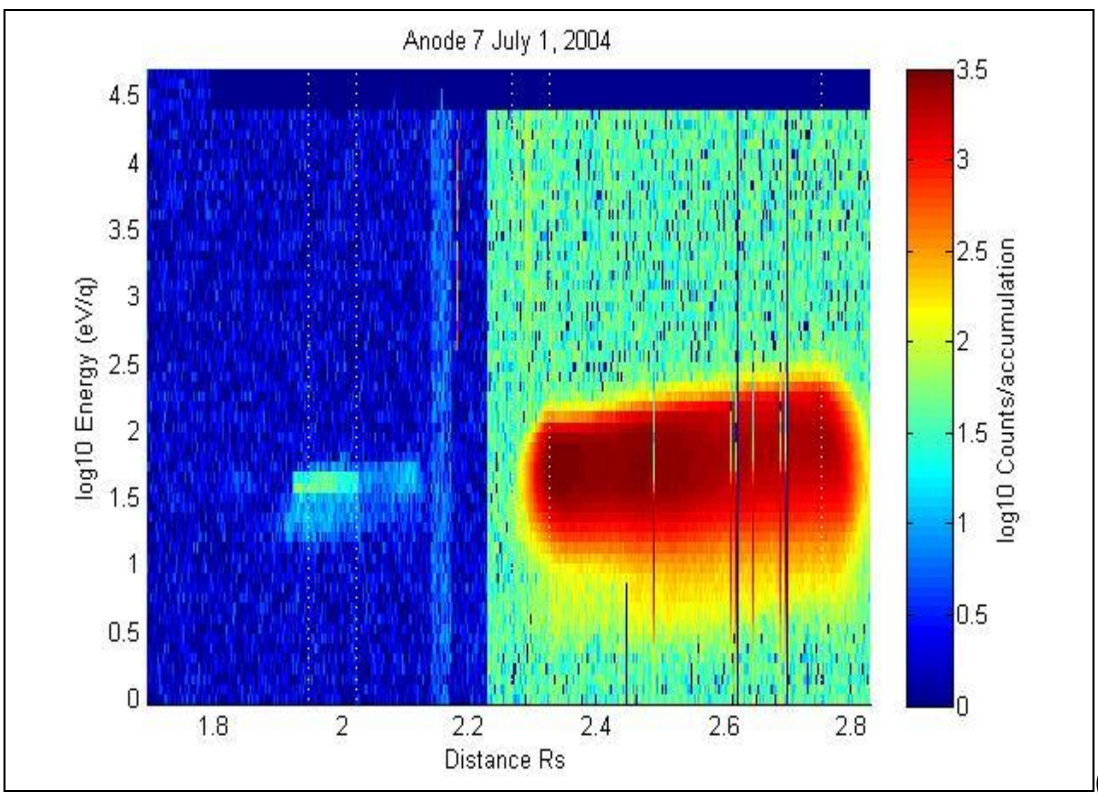
Anode 7 July 1, 2004
log10 Energy (eV/q)
4.5
4
3.5
3
2.5
2
1.5
1
0.5
0
1.8
2
2.2
2.4
2.6
2.8
Distance Rs
log10 Counts/accumulation
3.5
3
2.5
2
1.5
1
0.5
0
(b)

Figure2.3— CAPS Spectrograms of Anode 3 & 7 through SOI. These two spectra show the two regions of the SOI pass where data were collected from the two anodes with the best pointing. Panel (a) shows anode 3 which was best oriented to view the co-rotational plasma flow directly over the main rings before the spacecraft rolled during the ring plane crossing and panel (b) shows anode 7 which had the best pointing while the spacecraft passed between the F and G rings during the second part of the pass.

16] Fig. 2.2 show fits to spectra from the two sweeps at 1.94 Rs and 2.41 Rs respectively. The fit at 1.94 Rs, when the spacecraft is over the B-ring, indicates that the higher peak, in terms of counts/s, belongs to O_2^+ with the smaller secondary peak belonging to O^+ ions in agreement with *Tokar et al.* [2005]. The fit in the second region near 2.41 Rs, which is outside the main rings, again shows O_2^+ signature but both peaks are much broader, suggestive of both a higher plasma ion temperature and, possibly species from the water group W^+, other than O^+ are present.

17] A limitation of the SNG detector makes it nearly impossible to distinguish between the separate species of the W^+ group of ions from mass 16 to 19. This is partly due to the broadening of the peaks from the ion temperature, and partly from the limit in the resolution of the singles mode of the CAPS instrument. As a result, for consistency in this thesis, I chose to use mass 16 or O^+ for the W^+ group peak. I did this for two reasons, one, the Voyager 2 data were analyzed by assuming only mass 16 was present, and, two, over the main rings, O^+ was more likely produced from the photochemistry of the ring atmosphere than other W^+ products [*Tokar et al.,* 2005].

18] Fig 2.3 has two full color spectra of the SOI pass (a) over the main rings and (b) from between the F and G rings. Fig 2.3 (a) uses anode 3, as this had prime pointing into the plasma, while in (b) anode 7 had prime pointing into the plasma. The sharp increase in the background at around 2.2 Rs is due to the high density of ice grains in the main rings is no longer absorbing the penetrating radiation.

Section 2.2—Penetrating Radiation

19] Penetrating radiation is caused by high energy electrons penetrating into the CAPS instrument and is observed when Cassini is outside the main rings but near Saturn and is detected by CAPS as a broad background across all energy channels [*Young et al.,* 2004]. It becomes a significant factor for the detector within 4 Rs of Saturn and extends as far as 6 Rs. Fig. 2.6 shows two examples of full color spectra from this region both before and after correction for the background.

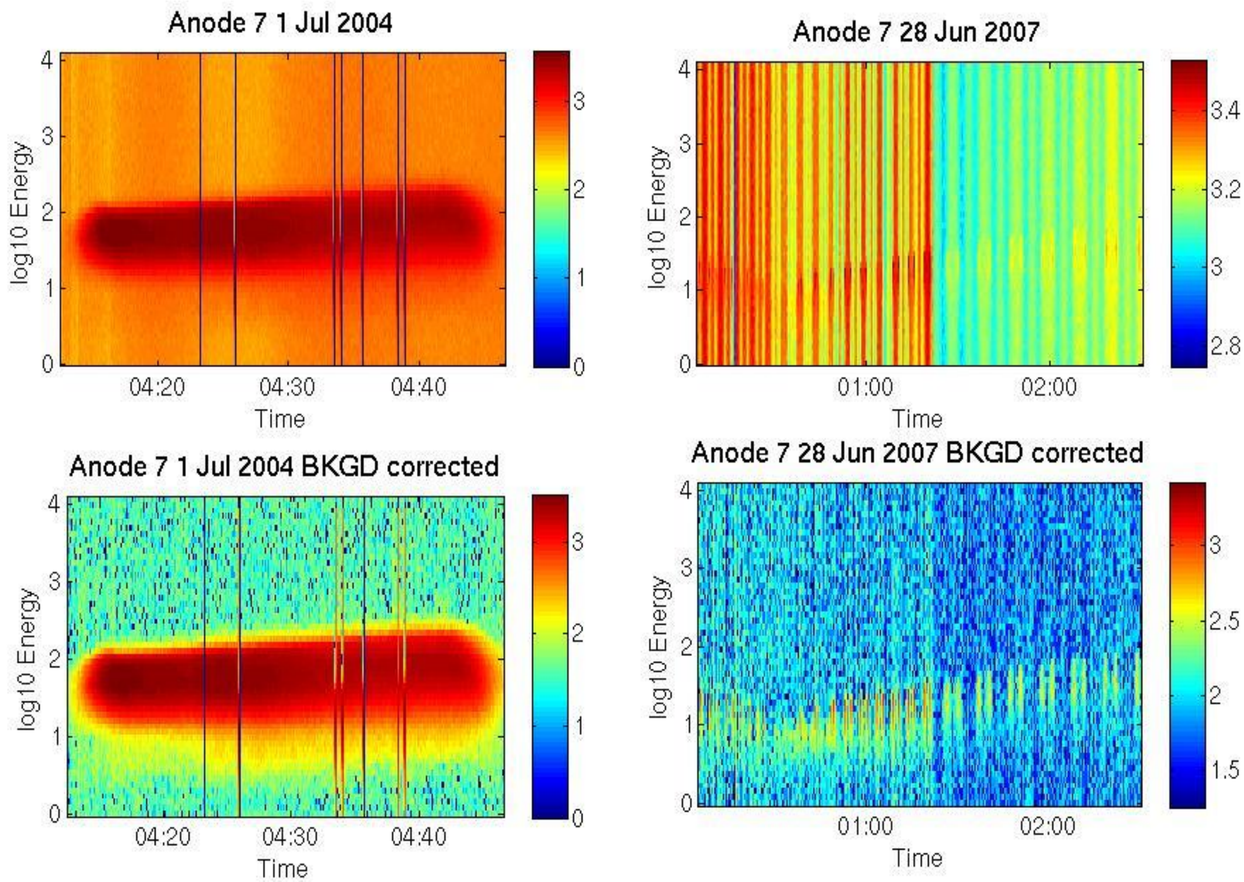

Figure 2.4—Spectra for, from left to right, SOI and 28 Jun 2007, both with background (top) and corrected for background (bottom). The apparent jump in background level in the 27 Jun 2007 images is due to a change in the telemetry mode as well as the spacecraft entering a region of higher penetrating radiation. It is clear from these spectra that unless the spacecraft has a good view of the co-rotational plasma flow, the peaks get lost to this intense background. Color bars are $\log_{10}$ counts/s, x-axis is time, y-axis is $\log_{10}$ energy (eV).

20] Due to limitations in bandwidth, an onboard 2-byte to 1-byte compression schemes of measured counts occurs, resulting in the CAPS detector effectively ‘quantizing’ counts. In other words, the count level increases in ’jumps’ as the number of counts increases. Therefore, as the background levels increase due to penetrating radiation, the count spectrum changes from a linear regime (0-63 counts) to higher jumps and becomes more pronounced. When there is a strong signal and the spectrum is well above the background, these jumps are small compared to the signal. However, for weaker signals as CAPS actuates out of the plasma flow, these jumps have a larger effect on the signal to noise ratio. Inside of ~4 Rs the background levels rise to a point where it becomes critical for the instrument to have sufficient pointing into the plasma flow direction in order to detect the signal as mentioned earlier. Only then do I find a good signal-to-noise ratio well above the background. Table 2.2 shows the background counts, maximum counts, peak width, how high these 'jumps' are max counts, and a signal to noise ratio for each data set used in this study.

Table 2.2: Comparison of maximum counts, background, peak width, signal to noise ratio, and step size at max for the data used in this study.

Data Set	**Average Maximum Counts**	**Average Background**	**Peak Width (ΔE)**	**Signal /Noise (max – bkgd) / bkgd**	**Step size at max(cts)**
Test Case (Rs = 6.3)	3625	45	543	80.5	~116
SOI	17245	587	117	28.3	~550
2005 248	2856	5912	82	7.61	~90
2007 162	9574	4834	76	0.981	~301
2007 178	9575	5912	81	0.619	~301
2007 179	5847	4315	22	0.355	~181
2010 062	1296	261	57	3.96	~41

2010 170	7492	4656	74	0.609	~234
2012 087	8715	3290	114	1.65	~265
2012 105	8495	3790	120	1.24	~265

Comparison of maximum counts, background, peak width and signal to noise ratio of the data sets used for this study. Test case is from 12 October 2005 used by *Wilson et al*., [2008] for production of plasma moments. Peak width determine by full width half max of the peak of the maximum anode of the data analyzed. Signal to noise is the ratio of the maximum counts to background. Background is determined as a fit parameter as described in data fitting section.

Section 2.3—31 Jan 2011 MCP Experiment with Penetrating Radiation

21] The CAPS team carried out an experiment to see if, by lowering the voltage on the micro-channel plates (MCPs) on the entrance to the instrument, we could improve the signal to background ratio of the instrument. By having the charge on the MCPs higher or lower it is possible to collect more or fewer charged particles near the spacecraft. The MCPs at the entrance to the IMS are negatively charged to collect ions, while the MCPs for the ELS are positively charged to collect electrons. During standard operation of the spacecraft the MCP's on the SNG at the entrance to the detector are set at ~-2600 eV.

22] During SOI, due to the thrusters being fired, the instrument was off, after which CAPS ran through the standard turn on sequence just prior to and during the process of passing over the main rings. This means that the voltages on the MCPs were not completely stepped up to full operating potential by the time the spacecraft passed over the main rings, but were nearly at maximum by the time the spacecraft finished passing through the F and G rings. The lower voltage on the MCPs could reduce the number of ions detected by the CAPS instrument. As a result the SOI densities could be slightly skewed by the fact that the MCPs were changing slightly during this pass, however, these lower voltages were accounted for in my analysis of the SOI data.

23] Since the background counts are so high inside of 5 Rs, the CAPS team decided to lower the MCP voltages to see if it was possible to decrease the background and yet still maintain a strong enough signal in order to increase the signal to noise ratio. On 31 Jan 2011 at ~02:00 and at ~03:45 the MCP voltage was lowered to ~-2300 eV. Fig. 2.5 graphs the absolute magnitude of the change in voltage across the MCP for the IMS and the ELS as well as the resulting spectra Fig 2.6.

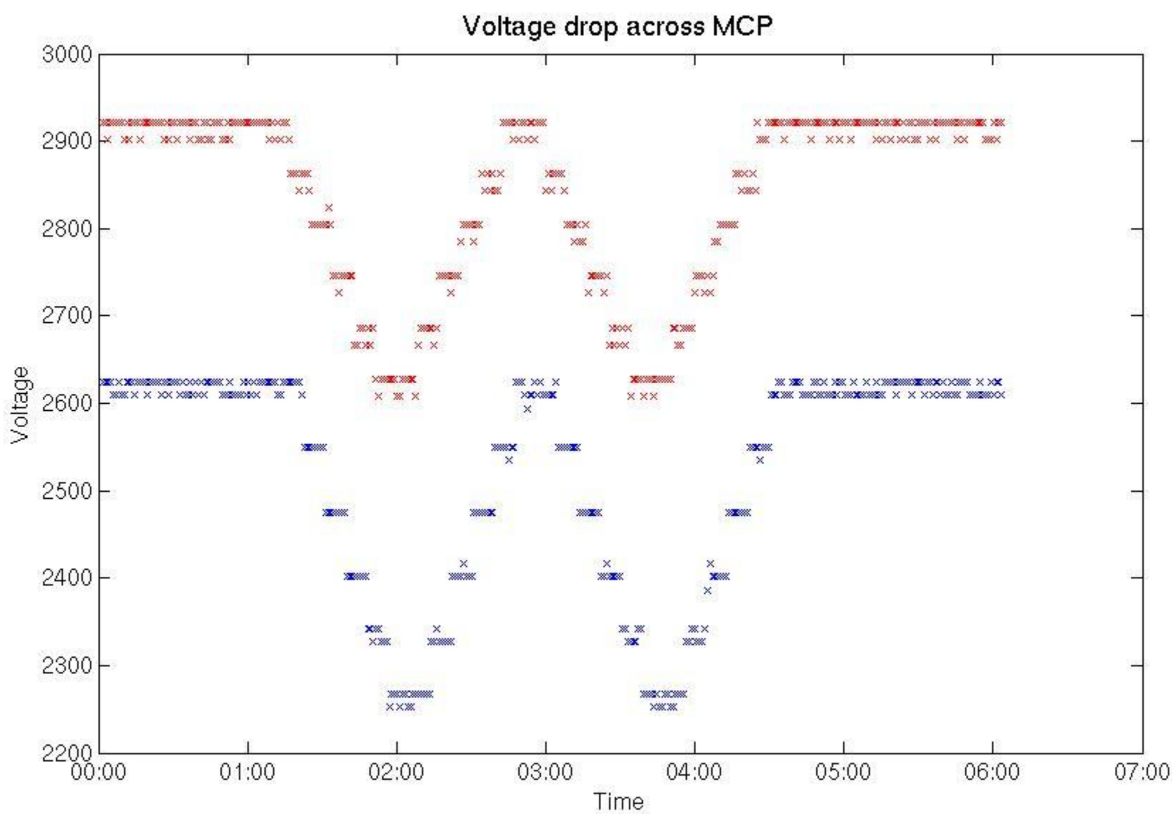

Figure 2.5— The absolute value of the changes in the MCP voltages for the IMS (blue) and ELS (red) during the 31 Jan, 2011 experiment. The IMS voltages are all

negative as it collects positive ions, and the ELS voltages are all positive as it collects electrons.

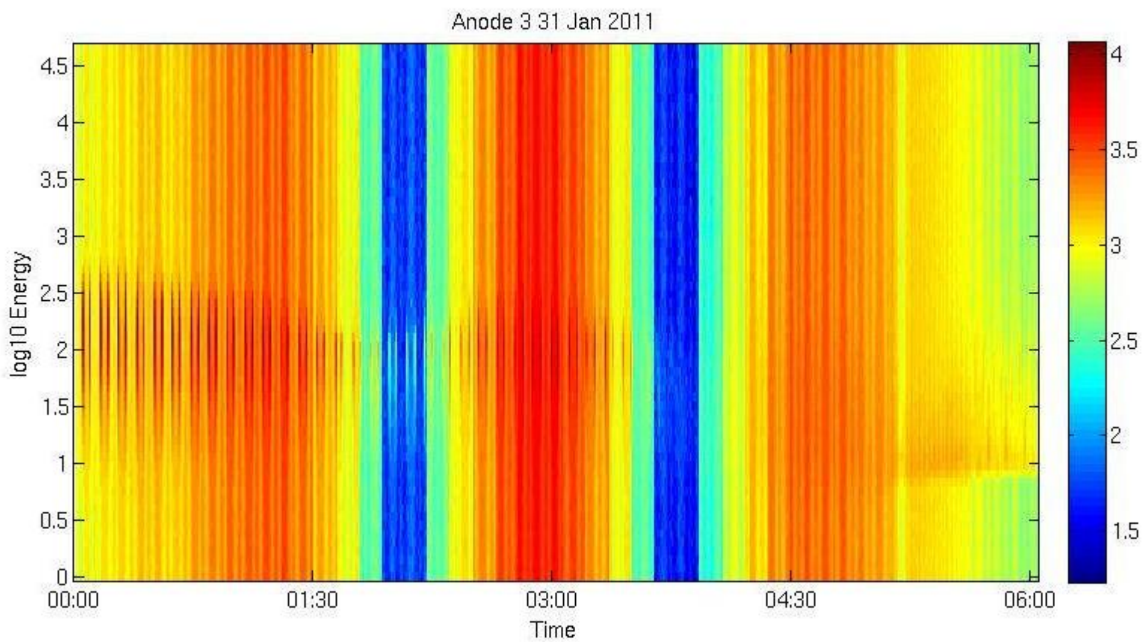

Figure 2.6—The spectrum showing how the drop in the MCP voltage affects the signal and background counts. Where the region drops from orange to blue is the region where the MCP voltage drops from ~-2600eV to ~-2300 eV.

24] As seen in Fig. 2.6, the background for the SNG data dropped for two time intervals for the singles counts. The ion signal, while reduced, was not lost in the process. After some analysis of the signal to noise ratio, the error in the fitting functions used, and closer examination of the peaks for identity characteristics, I also found that the signal to background ratio decreased, as was shown at the CAPS team meeting #42 in 2012 [*Wilson, Elrod, Crary,* 2012]. In addition, we determined that the error in the fitting functions increased. We examined several spectra from both before the MCP voltage is lowered and after the background is lowered. We found that the loss of total counts was more significant than the drop in the background. In addition there was a loss of the O_2^+ peak, indicating that lowering the MCP voltage created a loss of data in the heavier mass ions, which was already a weak signal. Therefore, this change in the MCP voltage was not advantageous as too much of the signal, particularly of the heavier ions, was lost.

Section 2.4—Fitting Procedure: 1D fit

25] In order to determine the principal plasma parameters, density, composition, temperature, and flow velocity the raw data must first be converted from the binary format into a format usable for the fitting program that I use in my data analysis method. I use energy sweeps that are summed up to the A-cycle level from the anode most closely pointed in the incoming plasma direction, i.e. the maximum anode with the most counts of the 8 anodes per A-cycle, is selected for each A-cycle. In an isotropic plasma flow, the direction the anode points is less important as the assumption is that the plasma is the same in all directions, therefore the maximum anode would see the same plasma as all other anodes. However, in an anisotropic plasma flow, as is dominant throughout Saturn’s magnetosphere, the plasma is not the same in all directions, thus the look direction of the anode becomes important. By selecting the maximum anode in an anisotropic plasma, this assures that anode will be looking nearly into the plasma and determine the parameters for the bulk of the plasma.

26] Occasionally an ion entering one anode can be counted by one or more neighboring anodes. This effect, known as instrumental crosstalk, will increase the counts in any one anode. *Thomsen and Delapp* [2005] analyzed this effect and determined a correctional matrix to correct the over counting which can amount to an over count by up to ~13% (see table 2.1). Therefore, I also correct the data for instrumental crosstalk [*Thomsen and Delapp,* 2005] before running any fitting algorithm.

27] In a 1D fit I select just the maximum anode for the purpose of determining the plasma parameters, density, temperature, and plasma flow velocity. In a 3D fit I use multiple anodes to determine the plasma parameters, however in this fitting function I determine the parallel and perpendicular temperatures (along the field lines and with the gyro-motion of the ions) and the full velocity components of the velocity. The 1D is limited in that it will only determine the temperature and velocity in the plasma flow direction. I carried out both 1D and 3D fits to the plasma data and created adequate methods for handling the background. For the 1D fits, rather than subtracting the background from the data and then fitting the spectra, I treated the background as a fit parameter for the data from the prime pointing anode, i.e., a constant term in the fit formula shown in Eq. 2.1 below. However, for the 3-D fitting method, I determined an individual background for each anode using an averaging method described further in section 2.3 and then subtracted the background from the data before obtaining a fit.

28] In the 1D fit I took each spectrum and fit it using a least squares non-linear regression algorithm to determine the ion plasma parameters: density, composition, temperature, and plasma flow velocity. The counts accumulated per A-cycle per anode in each spectrum were fit using the expression in Eq. 2.1

$$Counts(E) = BKGD + \sum_i dt * G_E * Eff(i,E) * (V_E(i))^4 * f(i,E) \qquad (2.1)$$

29] The variables in Eq. 2.1 are the time interval of accumulation, dt, the geometric factor of the instrument, G_E, the efficiency of the ion detection, *Eff* (i), the background count level, BKGD, the speed of the ion entering the detector, V_E, and the distribution function, $f(i, E)$, which is assumed to be a Maxwellian energy distribution, Eq. 2.2, for each ion species, *i*.

$$f(i,E) = n_i * \left(\frac{m_i}{2\pi k T_i}\right)^{3/2} * exp\left[-\frac{m_i (V_E - U)^2}{2kT_i}\right]; V_E = \sqrt{2E/m_i} \qquad (2.2)$$

30] The parameters in Eq. 2.2 are the ion density, n_i, temperature, T_i, and net plasma flow velocity *U*, which includes the spacecraft velocity. All variables in Eqs. 2.1 and 2.2 are in cgs units with k representing the Boltzmann constant. Assuming the two dominant species are O^+ and O_2^+, leads to the six fit parameters (T_{O+}, T_{O2+}, n_{O+}, n_{O2+}, U, and BKGD). The velocity, V_E of the ion entering the detector is determined by the energy bin, E.

31] Eq. 2.1 returns the fit parameters for each ion species. The model that is fit to the data is the sum of the two species that is then fit to the count data spectrum and subject to the χ^2 = (data – model)/data) which is minimized via the least squares non-linear algorithm. Fig. 2.7 has examples of these fits from each data set where the black line is the sum of the two species obtained my fit, the blue line is the data, the red line is the O_2^+ component I obtained from the fit, and the green line is the O^+ component fit.

32] Due to the number of fit parameters, the program does not necessarily give a unique solution. Therefore, I created a set of initial values that are reasonably close to the expected output values for the fit parameters. The plasma flow velocities were typically close to the corotation speed V_{co} = RΩ where R is the radial distance from the center of Saturn and Ω is Saturn's rotational velocity, in radian/s, which is connected with the rotation of the magnetic field. Therefore, the initial value I used for the plasma flow velocity is $U_0 \sim (V_{co} - V_{phi\_sc})$ in Eq. 2.2, where V_{phi_sc}, is the component of the spacecraft velocity in the direction of the plasma flow, near the ring plane, where most of these ions are formed. This is in the so-called corotation direction. Assuming the ions are freshly made, or the lifetimes are short, as is typical in a region that contains a significant neutral density as well as dust and ice grains like this one, the ion temperatures would be close to this initial 'pick-up' temperature, defined in eq. 2.3. Neutral particles are moving at the Keplerian velocity, V_{orb}, as these particles are ionized they are accelerated to the co-rotational speed of the field lines, V_{co}. The energy associated with this so called pick-up of the ions as they are ionized is known as the pick-up temperature.

$$kT_0 \sim {}^1/_2\, m_i (V_{co} - V_{orb})^2 \qquad (2.3)$$

33] Here V_{orb} is the Keplerian orbital velocity. The ion densities were given small rough initial values based on a loose calculation assuming initial T and U values. The initial value of the background parameter, BKGD, is equal to the minimum value of counts from bin 4 to 63 for each spectrum (Note: bins 1 to 3 were often initially erroneously set to 0 counts or contained other faults and have been rejected for the entire study as per CAPS policy [*Wilson et al.*, 2012]). See section 2.8 for further discussion of verification of the validity of these fits.

34] With the initial values provided, the fit algorithm was run through successive iterations to minimize the least squares difference between the model and the counts spectra. The following conditions determined convergence or termination of the fitting algorithm for a given spectrum:

a) The least squares difference between the data and the model falls below the preset tolerance of 1×10^{-7} between iterations, i.e. the difference in χ^2 values between iterations is small.

b) The maximum number of iterations of 1×10^5 was exceeded. Most model fits converged well within this number of iterations, chosen to keep the program running in a reasonable time.

c) The change in the fit parameters between each iteration is less than the preset tolerance of 1×10^{-7}.

35] If any one of these criteria is met the fitting routine was terminated and the results are returned. If the maximum number of iterations is hit or the peak fits on examination are not good (i.e. either significantly higher χ^2 values or by visual examination the model was very different from the data), then the spectral fits were re-run with adjusted initial parameters. In addition I tested the energy ratio between the O^+ and O_2^+ peaks to check if it was close to a factor of two, consistent with the mass ratio of two between these species. As it was possible for other species from the water group, to be present in this region, having masses 17 – 19, this ratio was not precisely 2, but often between 1.5 and 2.2. Therefore, I checked that the energy ratio was in this range to be consistent with a paring of two ions one of mass 32 and one near mass 16.

36] Fig. 2.7 has examples of model fits for several of the passes used in this study. The black line represents the model, the blue is the data, the red line is the mass 32 fit, and the green is the mass 16 fit. Also included in Fig. 2.7 is an example of a test spectrum from a data set from October 12, 2005 from 6.5 Rs where the background was much lower and the primary ions were W^+ and H^+. This test spectrum was used by *Wilson et al.* [2008] in the process to create the CAPS published ion database in the NASA Planetary Database System (PDS). I used this test spectrum to compare my method against published results to confirm that I was returning similar results.

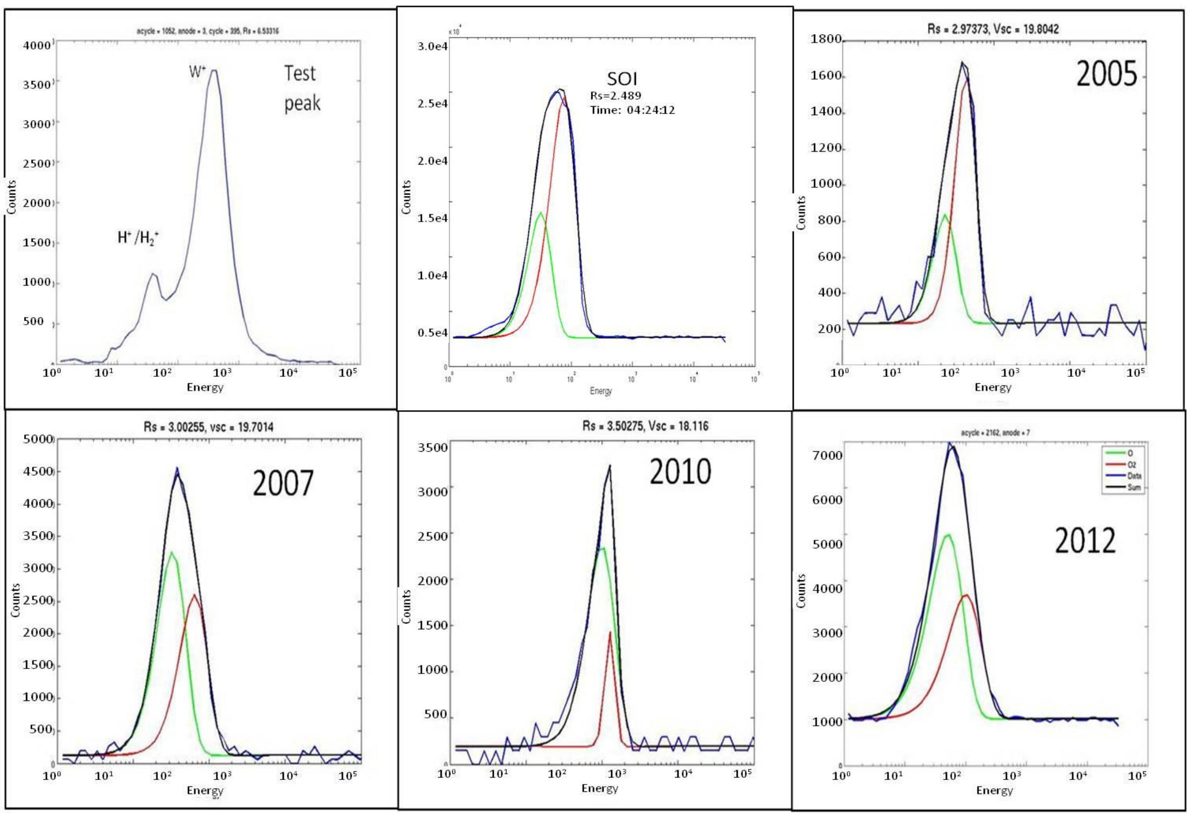

Figure 2.7-- Individual slices of counts/accumulation vs. energy from SOI, 2005, 2007, 2010, and 2012. Top left is a test peak from 12 Oct 2005; I used this spectrum to compare with the *Wilson et al.,* [2008] results. These spectra show the background of the each set where background is added to the fits as a constant parameter. The blue line is the data, the black is the model, a sum of the two ion species O_2^+ and O^+ ions, the green line is fit of the W^+ ion (16 amu) and the red line is fit of the O_2^+ ion (32 amu). X-axis is in Log_{10} energy (eV) and y-axis is counts/accumulation.

Section 2.5—Fitting Procedure: 3D Fits

37] The main difference between the 1D and the 3D fits is our attempt to derive the perpendicular and parallel temperatures: the temperature associated with the gyro-motion of the ions around the field lines and that along the field line. The 3D fit also attempts to return the 3 components of the velocity U. Therefore, it is necessary to simultaneously fit multiple anodes, and not just the anode pointing in the direction of the plasma flow. For the 1D fits I picked the anode with the maximum counts, with the idea that it was pointing into, or at least within 20° of the plasma flow direction. In the 3D fits I used multiple anodes simultaneously covering the plasma flow as far as possible.

38] The purpose of the 3D fitting function was to determine the ion density, the velocity in the r, θ, and ϕ directions as well as resolve the parallel temperature, $T_{||}$ and perpendicular temperature, T_L. This was similar to the goal of the 1D fit but involved a more complex distribution function for fitting the multiple anodes. The new distribution function is described in Eq.2.4.

$$f = n_i \left(\frac{m}{2\pi}\right)^{3/2} \left(\frac{1}{kT_\parallel}\right)^{1/2} \left(\frac{1}{kT_\perp}\right) exp\left(-m_i \left[\frac{(V_{E3}-(U_3-V_{sc3}))^2}{2kT_\parallel} + \frac{(V_{E2}-(U_2-V_{sc2}))^2}{2kT_\perp} + \frac{(V_{E1}-(U_1-V_{sc1}))^2}{2kT_\perp}\right]\right) \quad (2.4)$$

39] In Eq. 2.4 $T_{||}$ is associated with ion motion along the field lines. T_L is associated with gyro-motion of the ions around the field lines. U_r is the component of the flow velocity in the radial direction with positive being outward from the planet. U_θ is the component of the flow velocity associated with the direction along the field lines, (in spherical coordinates this is the polar component). U_ϕ is the azimuthal component of the flow velocity in the plasma co-rotational direction. U_r and U_θ are typically small, as freshly made ions are dominated by motion with the plasma making U_ϕ the dominant component, which is approximately equal to V_{co}. The V_{sci} are the three components of the spacecraft velocity.

40] Another major difference between the 1D and 3D fits is the method I used to determine the background. In the 1D fit, the background I used was a fit parameter for the prime pointing anode. However, since the counts and the background were lower for each anode off the prime pointing direction, it was necessary to calculate the background for each anode in the 3D fitting process. This is further explained in section 2.6.

Section 2.6—Background

41] Treating the background as a fit parameter, as I did for the 1D fits, in Eq. 2.1 gives a slightly more accurate measurement of the background than using a mean of bins outside of the peak. However, it does add an additional fit parameter to the fitting process which can add to the uncertainty of the fit and the difficulty of obtaining a unique fit.

42] The amount of noise in the count spectra in each anode was significant; I estimated the background for the 3D fits by averaging the data sufficiently far from the peak in each anode. Since I had already selected the anodes that had clear peaks, and had summed them to A-cycle resolution, I determined what was sufficiently far away from the peak for each anode by inspection. I found that using bins 35 to 63 and 4 to about 12, as suggested in the PDS CAPS user's guide [*Wilson* et al. 2012], was sufficient for being 'away from the peak.' The background calculated was within 1% of results obtained from the 1D fit. Fig. 2.5 shows these background calculations for each anode for SOI.

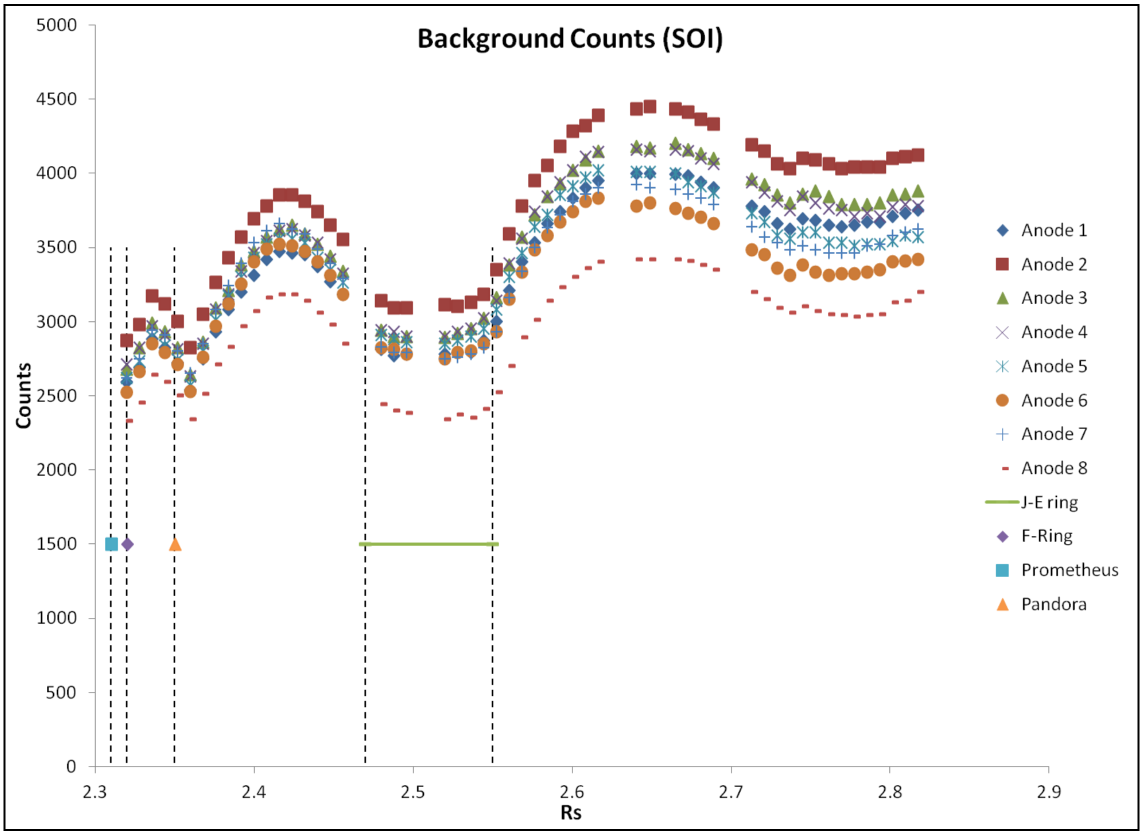

Figure 2.8—Background counts calculated from each anode during the SOI pass from July 1 2004 between the F & G rings. This high background signal causes for difficulty in analyzing the CAPS data in the region. From left to right, the vertical lines mark the small moons Prometheus, Pandora, near the F-ring, Janus, and Epimetheus.

43] The variations in the background in Fig. 2.8 corresponded well with measurements made of the high energy particle flux in this region [*Paranicas et al.,* 2008]. The significant dip at around 2.5 Rs corresponded to the locations of with the Janus-Epimetheus Ring that was also discovered in the high energy particles. The main rings showed that ice particles can absorb the high energy particles that make up background. Therefore, it is possible that the ice grains from the icy moons, and smaller rings throughout the region between the edge of the main rings and

Enceladus could also lower the background by absorbing these high energy particles. It is possible that the background detected by the CAPS instrument is similarly influenced by the high concentrations of ice particles produced by the rings and moons in the region and that by examining the variations in the background throughout the region we could detects some of these features.

Section 2.7—Counts Trends Analysis

44] According to section 2.2 where I discussed the 1D fitting procedure, the singles counts in a given energy channel are modeled using Eq. 2.1, where *dt*, *Eff*, G_E are assumed constant over each A-cycle within the interval, and *f* is the Maxwell distribution function in Eq. 2.2. I combined Eq. 2.1 and 2.2 and used a variable *a,* defined in Eq. 2.5.The leading constants, *dt, Eff, and* G_E combined into the constant term A resulting in the simplified form, Eq. 2.6.

$$a = \sqrt{2kT/m} \qquad (2.5)$$

$$\mathrm{C} = A \frac{n}{\pi^{3/2} a^3} V^4 exp\left[- {(\mathrm{V} - U)^2}/{a^2}\right] \qquad (2.6)$$

45] In order to test the validity of the results from my model, I also examined the relationship between the actual counts and the returned values from the fit parameters of the SOI data. This secondary test is carried out in order to visually check each individual peak to see that the fits appeared good, and that the χ^2 values were minimized.

46] In order to determine the validity of the returned values of the three fit parameters, U, T, and n, I also wrote three analytic expressions for the maximum velocity V_{max}, (eq. 2.9), the maximum counts, C_{max}, (Eq. 2.11), and the integrated counts, $\sum C_i$, (Eq.s 2.14 &2.17). I used my fit values in these expressions and compared them to the expected values to determine if my results were reasonable, e.g. the trends are close and none of the values are extremely different (more than a factor of four or five) from expected.

47] To obtain an analytic expression for the maximum velocity, I took the partial derivative of Eq. 2.6 with respect to V, and set it equal to 0 then solved for V. Using my fit values for U and a, Fig. 2.9 shows the maximum velocities determined using Eq. 2.7 below and the returned parameters U and T for the SOI pass for masses 16 and 32. These calculated velocities were compared to V_{co}.

$$0 = \frac{\partial C}{\partial V} \propto A\left[4V^3 - \frac{2V^4(V-U)}{a^2}\right] exp\left[-{(V-U)^2}/{a^2}\right] \rightarrow \qquad (2.7)$$

$$4 - \frac{2V}{a} - \frac{2VU}{a^2} = 0 \; solve\ for\ V \rightarrow \qquad (2.8)$$

$$V_{max} = 1/2\left[U + \sqrt{U^2 + 8a^2}\right] \qquad (2.9)$$

48] While the velocities for each individual species might be different from corotation, in the expression used in the 1D fit, one flow velocity is assumed for all ions. Therefore the total velocity might differ but will have the same trend vs. V_{co}. As these calculations shown in Fig 2.9, the velocities follow the same trend as V_{co}, even if the magnitudes were not precisely the same, indicating that U and T parameters were reasonable.

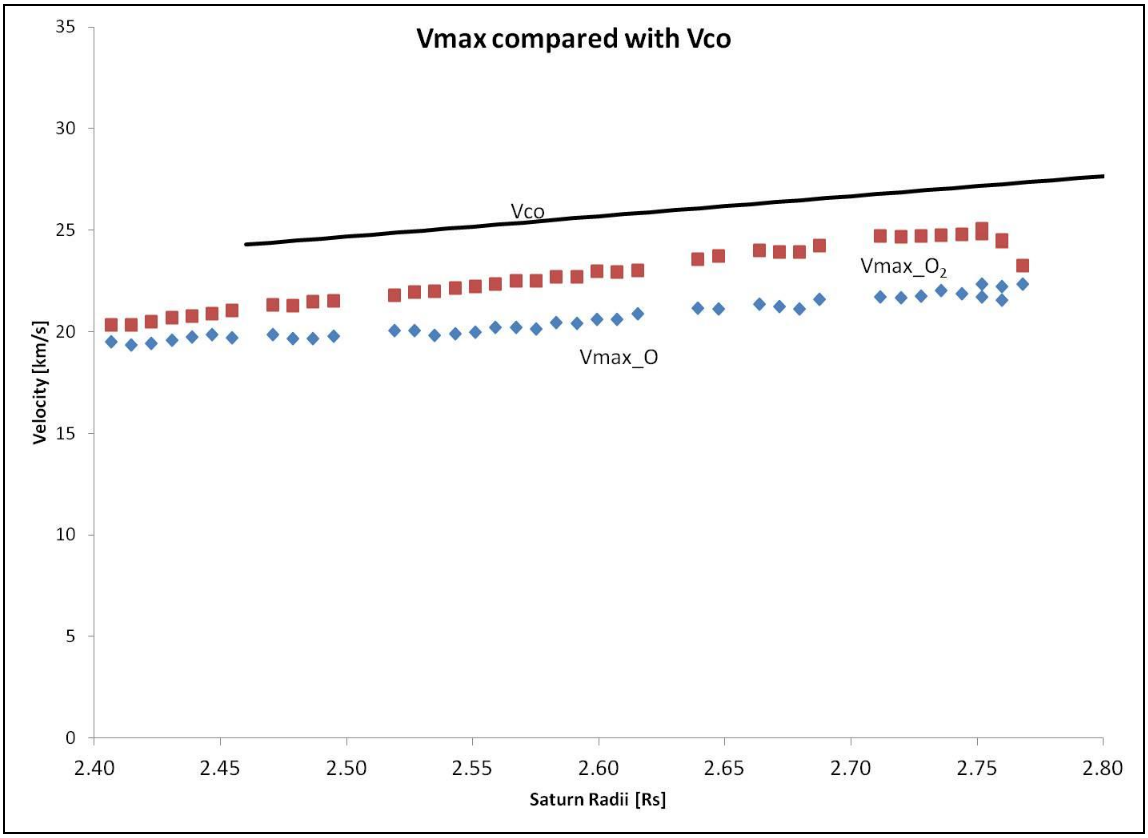

Figure 2.9—Maximum velocity calculated from Eq. 2.9 from the returned fit parameter U, and T for both O (m = 16) and O_2 (m = 32), which determines the position of the peaks. Each individual species velocity is close to V_{co} and follows the same basic trend, indicating that they are good fits and approximated by the expected values.

49] The analytic expression for maximum counts C_{max} given in Eq. 2.10, was determined by using the maximum V, and putting that back into Eq. 2.6. By considering the amplitude only, I could neglect the exponential term. The maximum in the counts spectrum, C_{max}, was then proportional to the expression in Eq. 2.10.

$$C_{max} \propto \frac{n}{\pi^{3/2} a^3} V_{max}{}^4 \qquad (2.10)$$

50] In the limit of a >> U, V_{max} is a constant, and C_{max} is reduced to the expression in Eq. 2.11.

$$C_{max} \propto \frac{n}{T^{3/2}} \qquad (2.11)$$

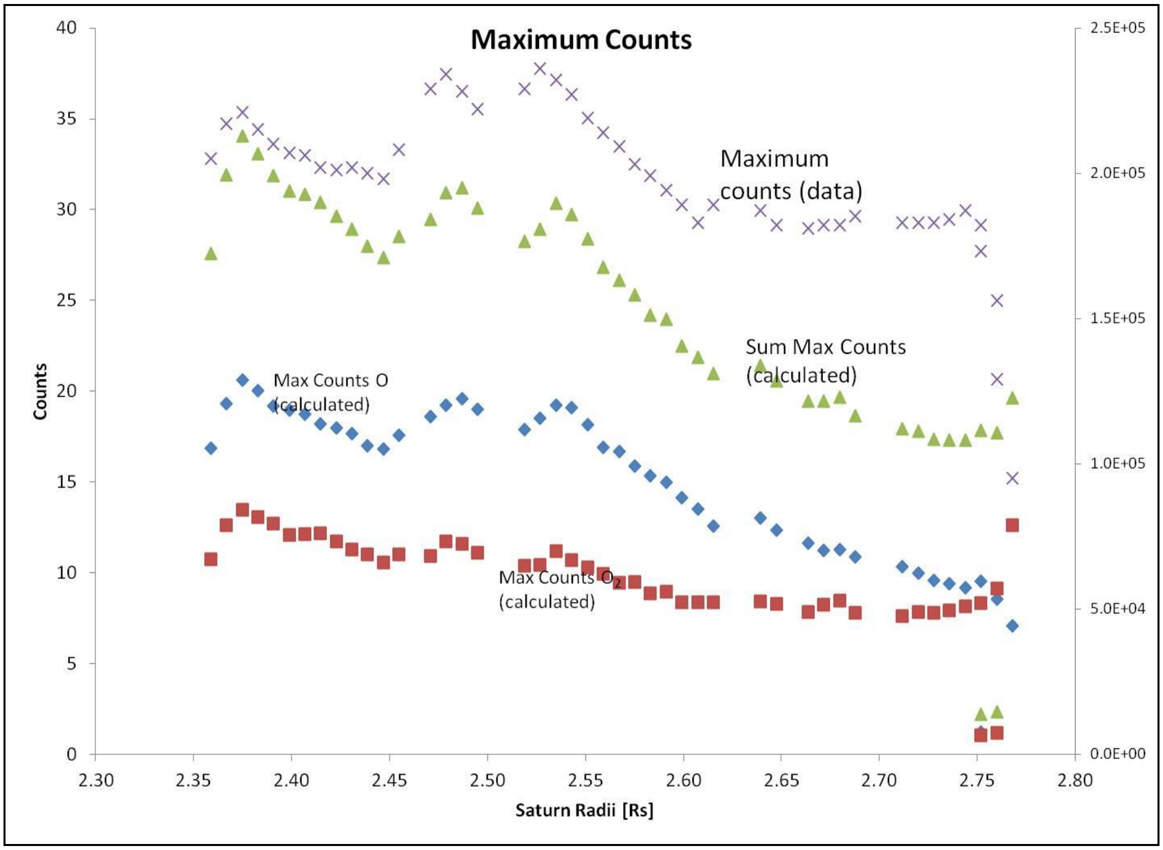

Figure 2.10—Calculated maximum counts are determined using Eq. 2.11 and the fit parameters n and Tare returned from the analysis of the SOI pass. This compares the counts for O^+ and O_2^+, as well as for the sum of the calculated maximum counts, with the maximum counts from the data. The x's represent the maximum counts from the actual data, the green triangles represent the sum of both O^+ and O_2^+ calculated maximum counts, the blue diamonds represent the maximum counts from O^+, and the red squares represent the maximum counts from O_2^+.

51] Fig. 2.10 gives C_{max} for the sum of the two ion species computed values using Eq. 2.11 and the returned values of n and T for SOI. It also shows C_{max} for each species. These are compared with the maximum counts from the SOI data. While the magnitude from the computed value did not exactly match the data, the overall trends of both the computed total and the total data are similar, indicating that the returned n and T values were reasonable. At this point I have used an analytic relationship between U and T, and a relationship between n and T. Finally I needed an analytic expression to test the exponential portion of Eq. 2.2 to the count spectrum, to do this I used the integral form of Eq. 2.6.

$$C = A\int d^3V(Vf) \rightarrow A\int V^2 d\Omega dV\ (Vf) \approx A\Delta\Omega\int V^3 dVf \qquad (2.12)$$

$$\sum_i C_i = \int_0^\infty x^3 dx \exp\left(-(x-M)^2\right)\ ; x = \frac{V}{a};\ M = U/a \qquad (2.13)$$

52] Because of the complexity of this form, I integrated it on Mathematica and evaluated it using the returned a and U values. However, Eq. 2.13 is only valid for a >> U which corresponds with the ions moving very fast. Upon examining the initial graphs I found that the ions move too slowly inside of about 2.5 Rs to justify the use of Eq. 2.13. Therefore, I obtained an expression applicable in the limit a << U. In this limit I needed to use more accurate calculations of the integral for each coordinate which is given in Eq. 2.15. Here I assumed that the plasma was flowing along coordinate V_3.

$$\sum_i C_i = A\int_{-\infty}^{\infty} dV_1 \int_{-\infty}^{\infty} dV_2 \int_0^{\infty} dV_3\ (V_3 f) \qquad (2.14)$$

$$= A\frac{n}{\pi^{3/2}a^3}\int_{-\infty}^{\infty} dV_1 \int_{-\infty}^{\infty} dV_2 \int_0^{\infty} dV_3 V_3\, exp\left[-\frac{(V_3-U)^2}{a^2}\right]$$

$$= A\frac{n}{\sqrt{\pi}\,a}\int_0^{\infty} dV_3 V_3\, exp[-(V_3 - U)^2/a^2] \qquad (2.15)$$

53] Again the integral was carried out using Mathematica to obtain a form that can be simplified in the limit a<< U to Eq. 2.16.

$$C \sim A\frac{n}{\sqrt{\pi}a}\sqrt{\pi}aU = AnU\ . \qquad (2.16)$$

54] Fig. 2.11 shows how the size of the count rate in these two limits relates and how they compare with the integrated counts after background has been removed from the data. While the plots are not an exact match, the trends for much of the region are similar indicating that again the parameters returned from my fits were not unreasonable. The areas of greatest concern, such as around 2.3 Rs to 2.4 Rs or 2.8 Rs, show the difficulty of this fitting algorithm during periods of high background signal.

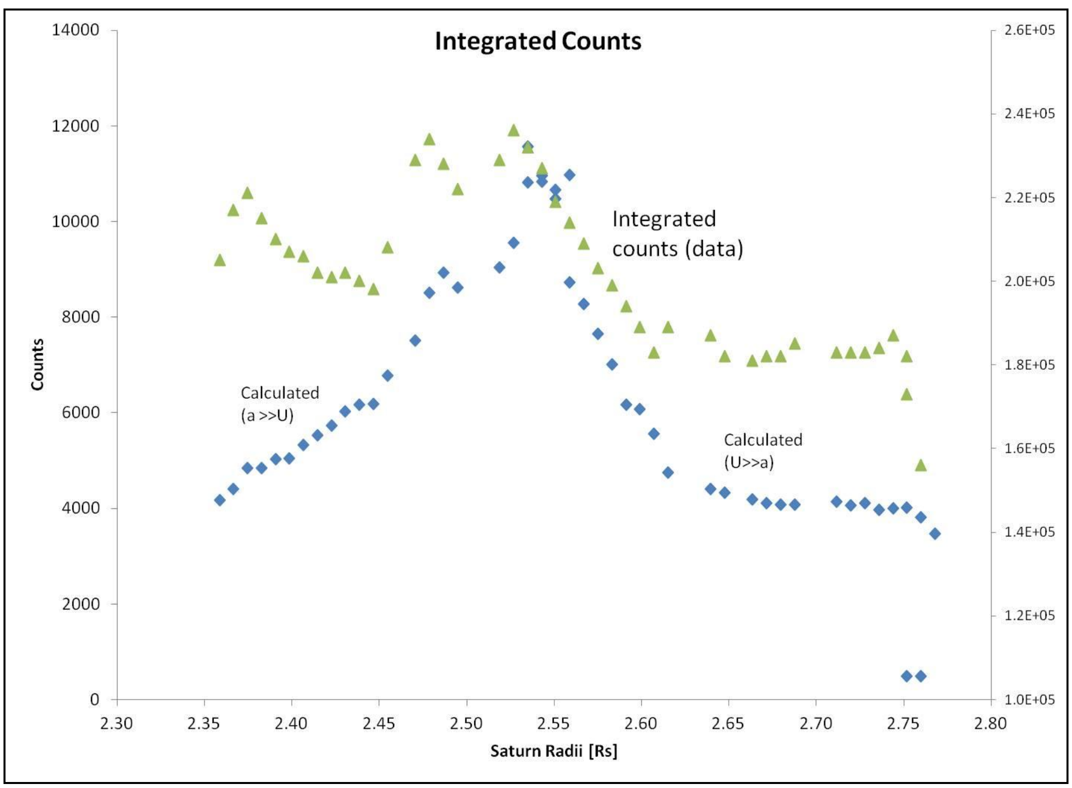

Figure 2.11—Compares the integrated counts from the data (green triangles) and the computed integrated counts determined from Eq.s 2.13 & 2.16 and the returned fit parameters from SOI Eq.s 2.13 and 2.16 (blue diamonds). Eq. 2.16 for a << U dominates up to 2.56 Rs where Eq. 2.13 for a>>U takes over. While the shape is not an exact match to the data, the overall match indicates a good correlation with the parameters.

55] Having now carried out a system of checks on the fit parameters, I assumed that the fits produced by the model from sections 2.4 were reasonable for the selected data. Eq. 2.6 is used to demonstrate that the U and T parameters were reasonable by comparison with the maximum velocity, Eq.s 2.13 and 2.16 were used to show the parameters and the exponential expression by comparing with the integrated counts were reasonable, and finally Eq. 2.11 is used to show the T and n parameters were reasonable by comparing with the maximum counts. By combining these checks, I demonstrated strong confidence in the 1D fitting algorithm I developed.

Section 2.8—Other statistical checks

56] I also made several checks to confirm that the position of the peaks and fit parameters returned by the program were appropriate. Given that O_2^+ is approximately twice the mass of the W^+ ions; the peaks in their respective fit spectra should differ by a factor of 2 as mentioned earlier. This difference in energy corresponds to a difference of only about 3-4 of the 63 logarithmically spaced bins in the Singles detector. Occasionally an error can occur in the fit procedure if the initial parameters produced a model that is outside of the peak region. The program will then find an incorrect solution nearby local minimum, or terminates without finding a solution. Such fits are visibly different and clearly incorrect. To avoid this, constraints were placed on the parameters, e.g. keeping the temperature and density positive, constraining the temperature to never significantly exceed the pick-up temperature, and kept the bulk velocities near corotation. When abnormal fits occur, they were re-run through the fitting program with adjusted inputs that are closer to the expected local minima until the spectral fits appear reasonable. If a reasonable fit to the count spectra cannot be obtained, the fits are not included in the final plots.

57] To confirm that the fits are acceptable, the following tests on each fit were run:

a) The O_2^+ ion peak must have a higher energy than the W^+ peak and that the difference between the peak maximum must be around 3-4 energy bins. As an energy ratio this equated to ~1.682 (3 bins) to 1.997 (4 bins).
b) Fixing the temperature to the pick-up temperature and then fixing the velocity at co-rotation, I also required that changes in the density must be relatively small as these are likely to be freshly produced ions. For instance it is possible to fit the peak with a lower mass like He+ at twice co-rotation. But this is not consistent with the known composition of the plasma in this region.
c) To confirm the presence of O_2^+, each peak was fit with just W^+ and the results and fit quality were compared with the fits with O_2^+ and W^+.

58] I also visually examined the fits to see if they were poor or if there were results that were inconsistent with the data, e.g. getting one peak with temperatures in the thousands of eV's. When this occurred, these data were re-run with refined initial parameters until all peaks returned acceptable fits based upon the above criteria. Preliminary tests were also carried out by comparing fits obtained using O_2^+ at mass 32 and various masses for W^+ at 16 through 19. I ran these tests to confirm my assumptions that mass 32 and mass 16 would return reasonable results. In addition to testing mass 32 and several W^+ masses. I also tested all of my spectra with only W^+ peaks and with only mass 32 peaks and compared the results. Fig. 2.12 is a comparison of these fits using W^+ (mass 17) only and the resulting least squared difference χ^2. It is seen that the χ^2 values generally were better using two peaks with W masses (i.e. 16-19 amu) and more improved when using a mass 32 and a mass (16-19). While the total densities and temperatures were all within approximately 20% to 40% of the values calculated, using two species, the χ^2 values were much higher when using a single peak alone.

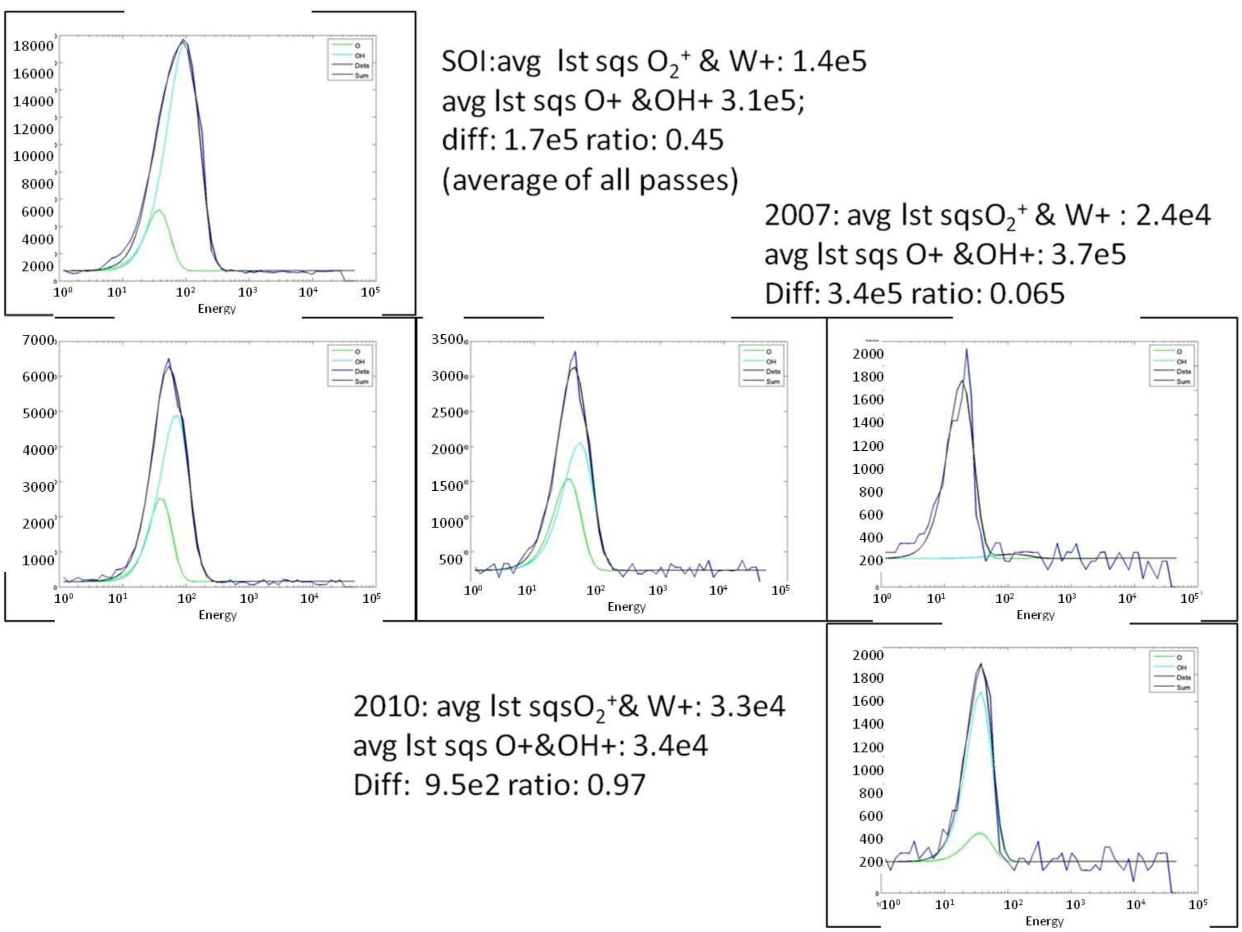

Figure 2.12 Several spectral from SOI, 2007, and 2010 with fits using only W^+. The black line is the model fit, the green line is a mass 16 fit, the cyan line is a mass 17 fit

and the blue line is the data. In comparing the χ^2 values from the W^+ only fits with the W^+ and O_2^+ fits, the χ^2 is reduced, indicating a better fit with mass 32 and mass 16.

59] For SOI, the extracted temperature of the larger mass corresponded to the pick-up temperature for O_2^+ and not for that of water group ions. This indicates the use of O_2^+ and W^+ was valid and that the program was correctly fitting these peaks to the spectra. For later spectra, similar comparisons were run with mass 32 vs. mass 16 or 17 and the temperature ratios were around 2:1 even though both temperatures were somewhat lower than the pick-up temperature. When running a comparison test using 11 & 12 October 2005 for several good A-cycles in the data, where Cassini is about 3.2 Rs from Saturn, the results showed that the velocities agreed with published results [*Wilson et al.,* 2008], which were approximately corotation. The temperatures from these tests were slightly less than, but close to the pick-up temperatures of O^+ ions as expected. As a result of these tests I confirmed that the best fits came from using O_2^+ and O^+ ions for this region.

Section 3: CAPS Ion Data Results

Section 3.1—CAPS Data Used in Study

60] Since Cassini first entered into orbit in 2004, there have been few passes with a periapsis closer to Saturn than 3.5 Rs. As discussed in section 2, the high background inside of 5.5 Rs causes significant interference with the incoming signal, and if the instrument is not pointing directly into the plasma flow, there is often an insufficient signal to noise ratio for analysis. This reduces the number of useable orbits from 2004 to 2012 to eight with a periapsis inside of 3.5 Rs and good pointing into the plasma flow. The orbits for all the data used for this study are shown in Fig.1.2. In addition, Table 1.1 gives the solar zenith angle of the rings, the solar activity level, approximate ring temperature and the time segments of each orbit used in this study. Solar zenith angle is used to determine the changing seasonal tilt and effect on the ring atmosphere and surface temperature of the main rings. It is possible the solar activity level could have an impact on the production of O_2^+ and O^+ ions in the region of interest because varying solar UV photons flux can impact decomposition and ionization rates.

Section 3.2—1D Ion Results: Ion Densities

61] Due to the uniqueness of the SOI orbit, this data set is important to examine. The SOI orbit had a very close periapsis, but the instrument settings differed from those in the subsequent sets used for this study. The MCP voltages were lower, CAPS wasn't actuating, and this was the only pass to go directly over the main rings and between the F and G rings. Because the thrusters were fired to slow the spacecraft for orbit insertion, CAPS was turned off until after the thrusters were off so that it would not be damaged by the fuel. When turned back on, the voltage on the MCP voltage was at half during the collection of the data both over the main rings and through the passage of the F and G rings. This voltage was subsequently increased to the standard running voltage. The result was that the detection efficiency for this pass was reduced to ~56% of the normal. The instrument was also not actuating throughout SOI resulting in anode three pointing closest to the plasma flow when Cassini flew over the rings. After a roll maneuver, which caused a small break in the data just off the A-ring, anode 7 was then pointing closest to the plasma flow as the spacecraft crossed the ring plane.

62] *Tokar et al.* [2005] originally analyzed the SOI data from over the main rings detecting both O^+ and O_2^+ ions. From this data *Johnson et al.* [2006a] determined the existence of an O_2 dominated ring atmosphere with follow-up work done on modeling this atmosphere by *Luhman et al.* [2006], *Bouhram et al.* [2006] and, most recently, *Tseng et al.* [2010; 2012]. Due to the changing illumination on the rings, a seasonal effect on the spatial distribution of this atmosphere beyond the main rings into the region between the F and G rings was predicted in *Tseng et al.* [2010]. Since the analysis in *Tokar et al.* [2005], the efficiency of the detector has been revised to be an ion and energy dependent version. This revision came about through internal CAPS discussions and meetings [*Reisenfeld*, private communication]. Therefore, I re-analyzed the data using the revised efficiencies for each species. I then compared my results with those from the *Tokar et al.* [2005] study (Fig. 3.1).

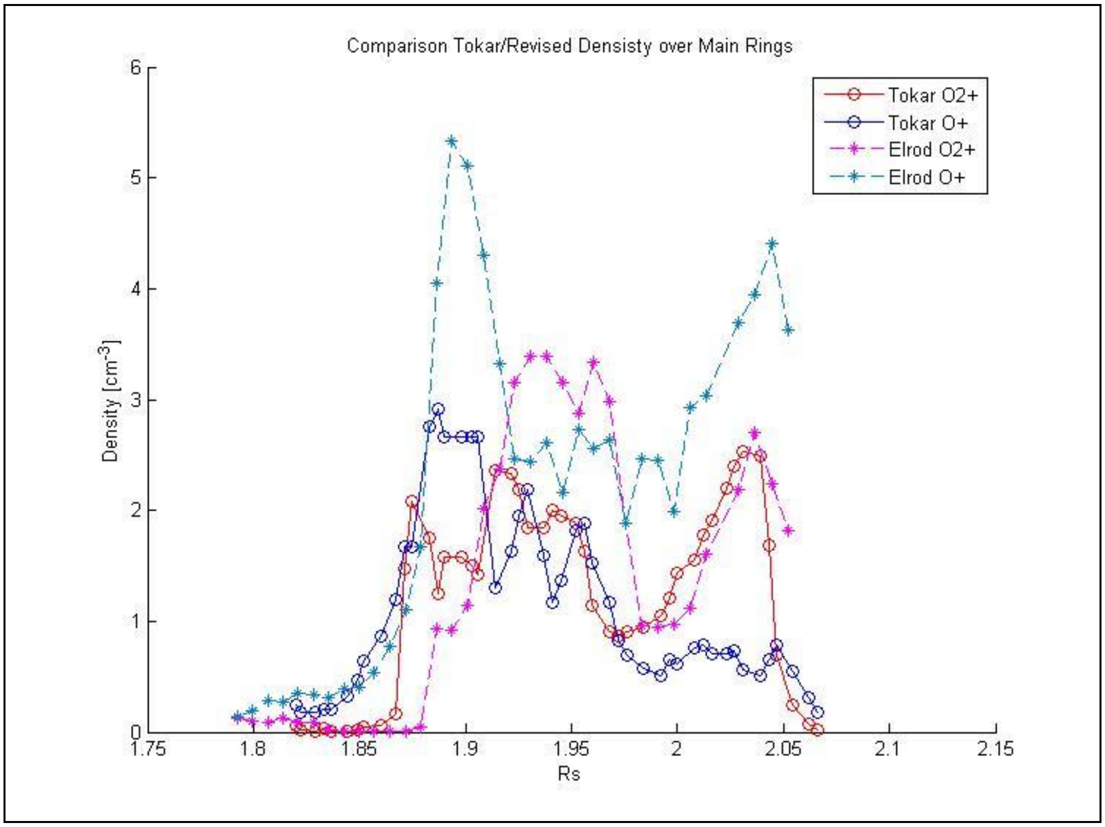

Figure 3.1-- Comparison of SOI data from over the main rings as analyzed here with published data analyzed by *Tokar et al.* [2005]. *Elrod et al.* [2012] is higher by about a factor of 2, accounted for in the revised efficiencies.

63] Over the rings, Fig. 3.1 shows that there are similar trends between the two different analyses of this data. When compared with the *Tokar et al.* [2005] results, the change in efficiency had the effect of increasing the densities by about a factor of two. This accounts for most of the differences seen in Fig. 3.1; slight differences in the fitting techniques account for the fluctuations between the results. In addition, the dip in the O_2^+ data near 2 Rs is now closer to the Cassini Division located between 1.94 and 2.02 Rs where the O_2 source is known to be smaller. Therefore, my new results in Fig 3.1 should be used in future analysis of the ring atmosphere. As discussed in section 4, these data were also used to normalize our modeling of the extended ring atmosphere.

64] Cassini's pass over the main rings occurred at a relatively high altitude, as seen in the orbits in Fig.1.2, so that the density of O^+ at spacecraft position was on average higher than that of O_2^+, which has a smaller scale height (see section 4.2) [*Johnson et al.*, 2006a; *Hill et al.,*1976]. Outside the main rings, as Cassini approached and crossed the magnetic equator, the measured O_2^+ density dominated during SOI. Although *Tokar et al.* [2005] showed that O_2^+ might be present outside the main rings, no analysis was conducted at that time.

65] The total ion density beyond the main rings is presented in Fig. 3.2a for each of the sets examined in this study along with the published ion densities from the Voyager 2 data [*Richardson,* 1986; *Elrod et al.,* 2012]. Since the densities are sensitive to the spacecraft height above the magnetic equator, Fig. 3.2b shows the total densities within 0.05 Rs of the magnetic equator to better compare the data from different passes and to reduce the effect of the position of the spacecraft.

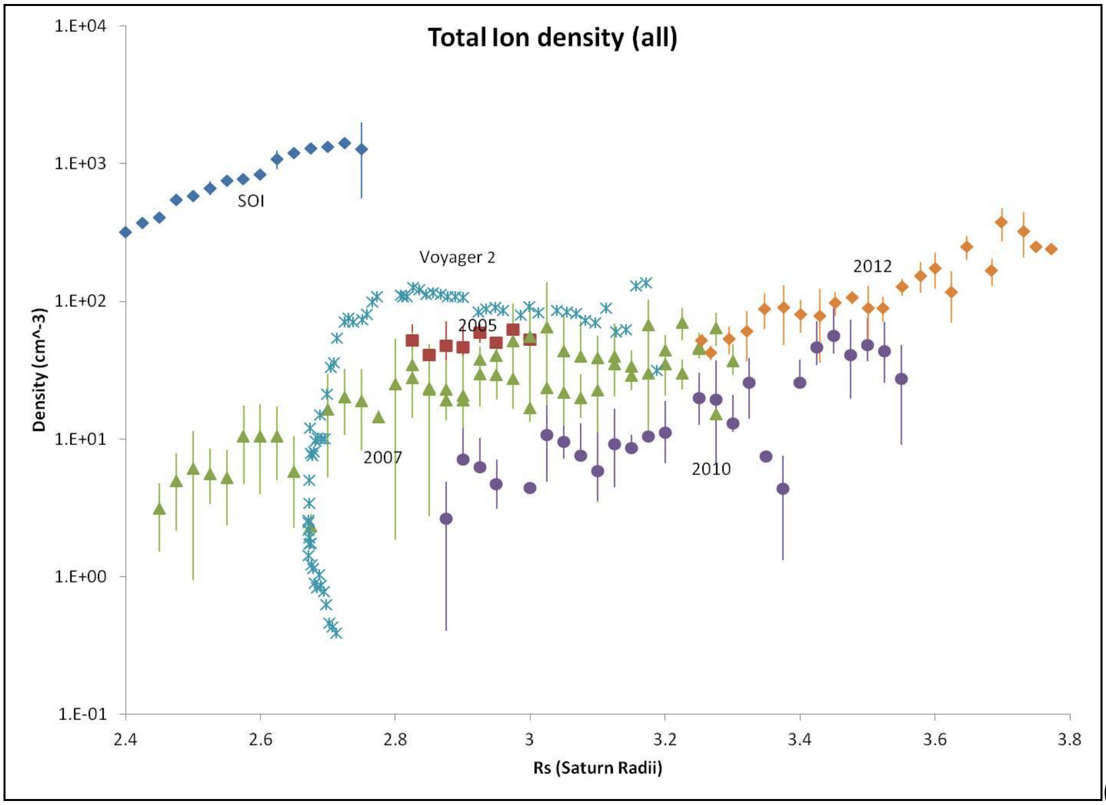

Total Ion density (all)
Density (cm^-3)
1.E+04
1.E+03
1.E+02
1.E+01
1.E+00
1.E-01
SOI
Voyager 2
2012
2005
2007
2010
2.4
2.6
2.8
3
3.2
3.4
3.6
3.8
Rs (Saturn Radii)

(a)

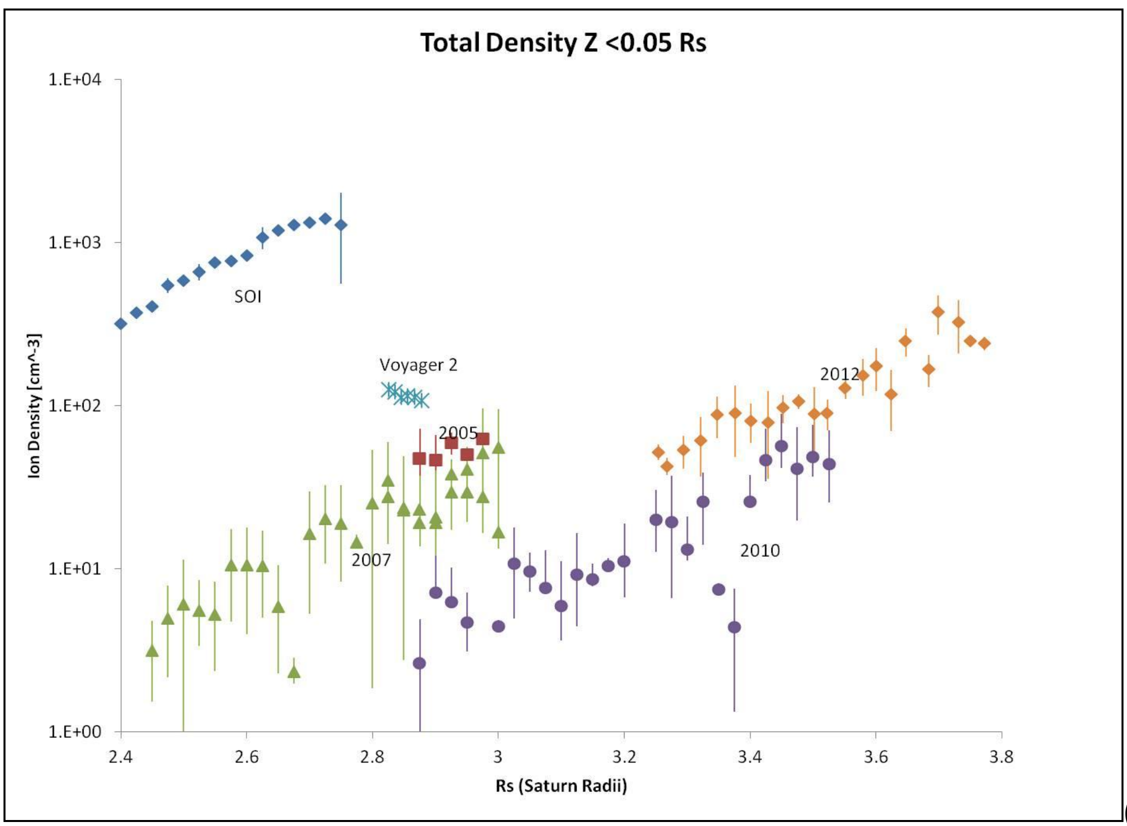

Total Density Z <0.05 Rs
Ion Density [cm^-3]
1.E+04
1.E+03
1.E+02
1.E+01
1.E+00
SOI
Voyager 2
2012
2005
2007
2010
2.4
2.6
2.8
3
3.2
3.4
3.6
3.8
Rs (Saturn Radii)

(b)

Figure 3.2—(a) Total ion density for the data in the region of study throughout the entire trajectory. (b) Total ion densities within ±0.05 Rs of the magnetic equator. SOI is in blue diamonds, 2005 is in red squares, 2007 is in green triangles, 2010 is in purple dots, 2012 in orange diamonds, and Voyager 2 in teal X's. Data are averaged over 0.025 Rs steps and the error bars are generated using one standard deviation over these steps.

66] Surprisingly, I found that the total densities from the 2004 pass are approximately two orders of magnitude above the passes from 2005 and 2007 with the 2010 passes exhibiting the lowest total densities. The Voyager 2 data (1982) near ring plane crossing are also seen to be intermediate to the SOI and the 2005-2012 data: about an order of magnitude higher than 2007-2012 and an order of magnitude lower than SOI. Although the 2005 data are between the Voyager 2 data and the 2007 data, with so few points it is hard to draw conclusions about the time between 2004 and 2007. Although the 2012 densities, on average, are larger than the 2010 densities, they were mostly taken at larger radial distances from the main rings. Where they do overlap, there is a suggestion of an increase in the ion densities. These trends will be discussed shortly in terms of the two likely sources of oxygen, the ring atmosphere and the water products from the Enceladus torus. Unfortunately, due to a technical issue with the CAPS instrument, from June 2012 to the time of publication, the instrument is not functioning and currently has no known timeline for restart.

67] Fig. 3.3a shows the individual densities from all the passes within 0.05 Rs of the magnetic equator. At SOI in 2004, O_2^+ dominates over the W^+ ion densities. In the later data from 2005-2010, the O_2^+ densities are either about the same or less than the W^+ densities. By 2012 the W^+

data dominates over the O_2^+. The Voyager 2 data were fit assuming only O^+ (mass 16) for ions inside of 14 Rs [*Richardson* 1986] and thus it is not included in the ratio Fig. 3.3b. Not only were the detected densities higher by two orders of magnitude at SOI but the O_2^+/W^+ ratio shown in Fig. 3.4b indicates that there was much more O_2^+ at SOI and that this drops off for all the other passes. There is an increase in the O_2^+/W^+ ratio in 2012 from 2010 indicating that the ring atmosphere is recovering. However, the density trend increasing toward Enceladus past about 3.6 Rs indicates that most of the 2012 data are likely water products from the Enceladus torus, which I will discuss in further detail.

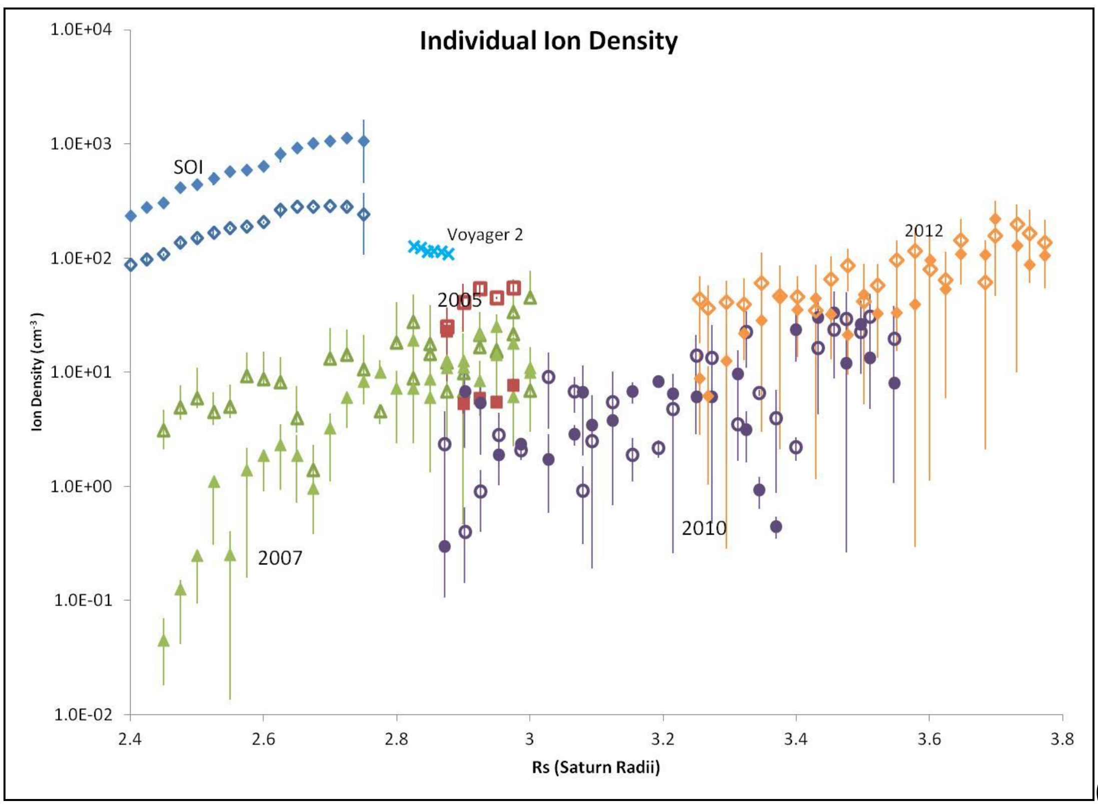

(a)

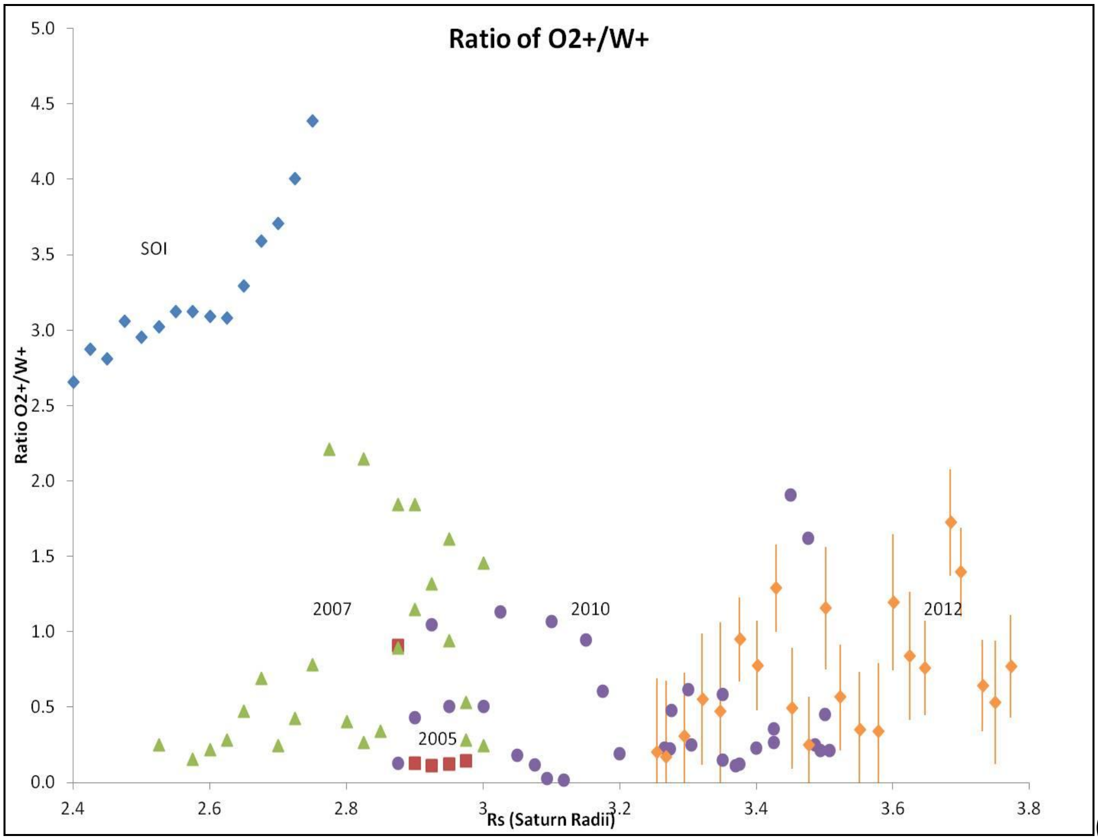

(b)

Figure 3.3—(a) W^+ and O_2^+ ion densities for data in the region between ± 3100 km of the magnetic equator. Open shapes are W^+ and closed shapes are O_2^+. SOI is in blue diamonds, 2005 is in red squares, 2007 is in green triangles, 2010 is in purple dots, 2012 is in orange diamonds, and Voyager 2 in teal X's. (b) Ratio of O_2^+/W^+ for the ion densities in the region. SOI has a significantly higher abundance of O_2^+ over the later passes. The 2007 and 2010 have a particularly low ratio indicating a significant drop in the O_2^+ from the ring atmosphere at equinox. Data are averaged over 0.025 Rs (1500 km) steps and the error bars are generated using one standard deviation over these steps. Note the Voyager 2 data were only fit assuming a W^+ (mass 16) and thus not included in (b).

Section 3.3—RPWS Electron Densities

68] To confirm the trend seen in the total ion densities, I compared the ion densities to the electron densities obtained using Radio Plasma Wave Science (RPWS) data [*Persoon et al.,* 2006 & private communication]. Since the ions are singly ionized in this region, charge neutrality implies that the total electron and total ion densities should be approximately equal. If there are significant H^+ and H_2^+ densities in the region, which are not accounted for in this study, the electron densities would be larger than the total ion densities. In addition, electrons can be absorbed by the ice and dust produced primarily in the E, F, and G rings, resulting in charged grains thereby affecting the comparison. This may explain why there is such a significant discrepancy between the SOI electrons and ions. Finally, due to the high background radiation within the instrument, it is also difficult to obtain accurate RPWS electron densities in this region; thus there is very little overlap with RPWS data in the region of principal interest with the data available.

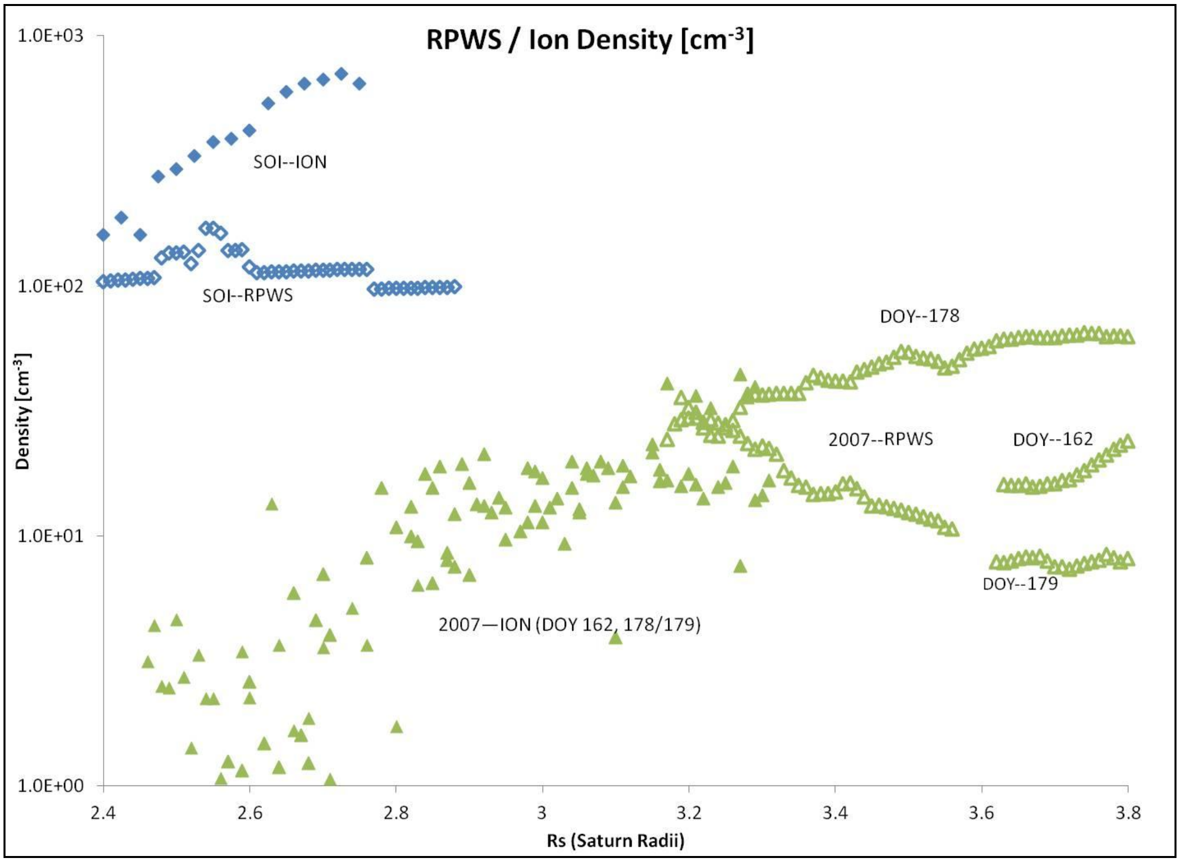

Figure 3.4—Electron density from RPWS compared to my total ion densities. SOI total ion densities are shown in solid blue diamonds, RPWS are in open blue diamonds. 2007 total ion densities are shown in green triangles, with the corresponding RPWS densities shown in open green triangles. 2005, 2010, and 2012 were not available for this study due to difficulty in obtaining data in this region. [*Persoon,* private communication]

69] Fig. 3.4 shows the electron densities determined by RPWS from the SOI and the 2007 orbits. The 2007 RPWS data does not extend in as far as the CAPS data; however the trends between the two are comparable. The differences seen in Fig. 3.4 between the ion and electron densities at SOI could be due to the presence of a significant density of ice grains from the F and

G rings, which can absorb electrons. Between the ice grains and the high radiation background, which affects the analysis from both instruments in the region, it is possible that the electron densities could be higher. Allowing for these uncertainties, Fig.3.4 demonstrates rough agreement between the trends in the ion and the electron densities. That is, the electron densities exhibit a similar drop between SOI and 2007 after which they exhibit and trend of increasing toward Enceladus.

Section 3.4—Ion Temperatures

70] The 'pick-up' temperature, as described in section 2.4, Eq. 2.3, is the kinetic energy of gyro-motion around the field lines for freshly created ions. Fig. 3.5 is a plot of my extracted values of kT_i/m_i compared with the pick-up temperature divided by the mass: e.g., ½ $(V_{co}-V_{orb})^2$. The ion temperatures were plotted in 0.025 Rs (1500 km) increments using only the results within ± 3100 km of the magnetic equator to reduce the effect due to the position of the spacecraft in Saturn's magnetic field. If the ions all have short lifetimes and are dominated by pick-up, then kT_i/m_i should be approximately equal for each pass. However, it was seen that although the variation with increasing distance follows that of the pick-up temperature, the extracted temperatures were always lower, except for SOI.

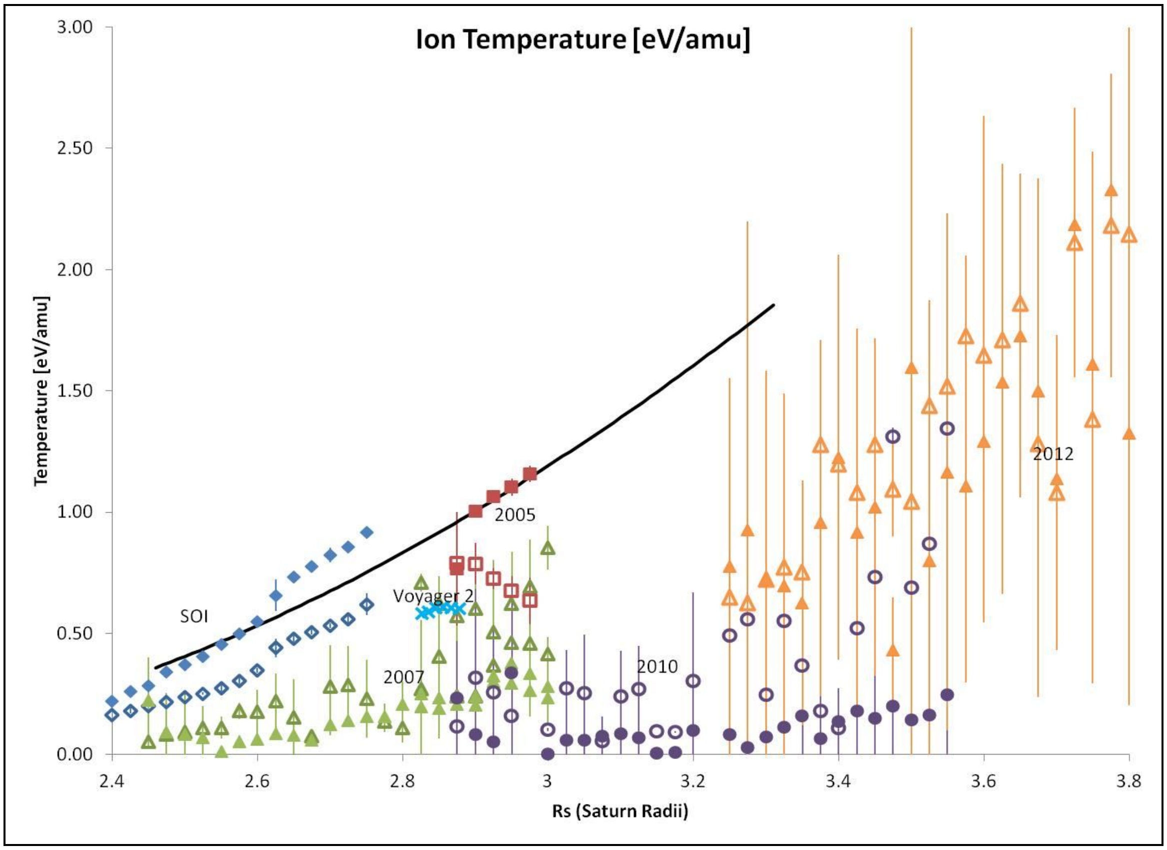

Figure 3.5—Ion temperatures/ion mass [kT_i/m_i] for all data sets within z = ± 3100 km of the magnetic equator compared to ½ $(V_{co} – V_{orb})^2$ (the solid line). Open shapes are W^+ and closed shapes are O_2^+. SOI is in blue diamonds, 2005 is in red squares, 2007 is in green triangles, 2010 is in purple dots, 2012 is in orange diamonds, and Voyager 2 in teal X's. Data are averaged over 0.025 Rs (1500 km) steps and the error bars are generated using one standard deviation over these steps.

71] The temperatures shown in Fig. 3.5 were higher at SOI in 2004 than they are for 2007 to 2010, and it can be seen that the 2012 temperatures were starting to rise back to the 'pick-up' temperature as the spacecraft gets closer to Enceladus' orbit. In this plot, the SOI and 2005 values for kT_i/m_i, particularly for O_2^+, were much closer to the pick-up temperatures. As will be discussed in section 4, this was consistent with freshly ionized O_z from the ring atmosphere particularly at SOI. The temperature difference between the W^+ and O_2^+ ions, however, was large at SOI. In the later passes the W^+ temperatures and O_2^+ temperatures were closer to being equal, but the overall values are much lower than the local pick-up temperatures. Since the analysis is 1D, the extracted temperatures were closer to a perpendicular temperature (gyro-motion temperature) where $T_{tot} \sim 2/3\ T_L$. The temperature was affected by the uncertainties of the extracted flow speeds discussed below. However, the trends pointed out here are consistent with the energy spectra being narrower in Fig. 2.7 in 2007 and 2010 than in SOI, and 2012. The effects on the temperatures and possible causes for this will be discussed further in Section 4.

Section 3.5—Plasma Flow Velocity

72]   The parameter U in Eq. 2.2 depended on the plasma flow velocity and the spacecraft velocity. Fig. 3.6 depicts U extracted from the fitting procedure with a correction for the V_ϕ (corotational plasma flow direction) component of the spacecraft velocity, all converted into spherical coordinates. As these results were obtained from one-dimensional fits, the correction to the flow velocity does not include the V_r or V_θ component (as described in section 2.5) of the spacecraft velocity. The results were compared to a line depicting the corotation velocity, V_{co} (red), and a line for the Keplerian orbital velocity of the neutrals, V_{orb} (green). Although the data showed no clear trend, the size of the extracted speeds were roughly consistent with the size of the expected plasma flow (V_{co}) and much larger than the neutral orbital speeds as they should have been.

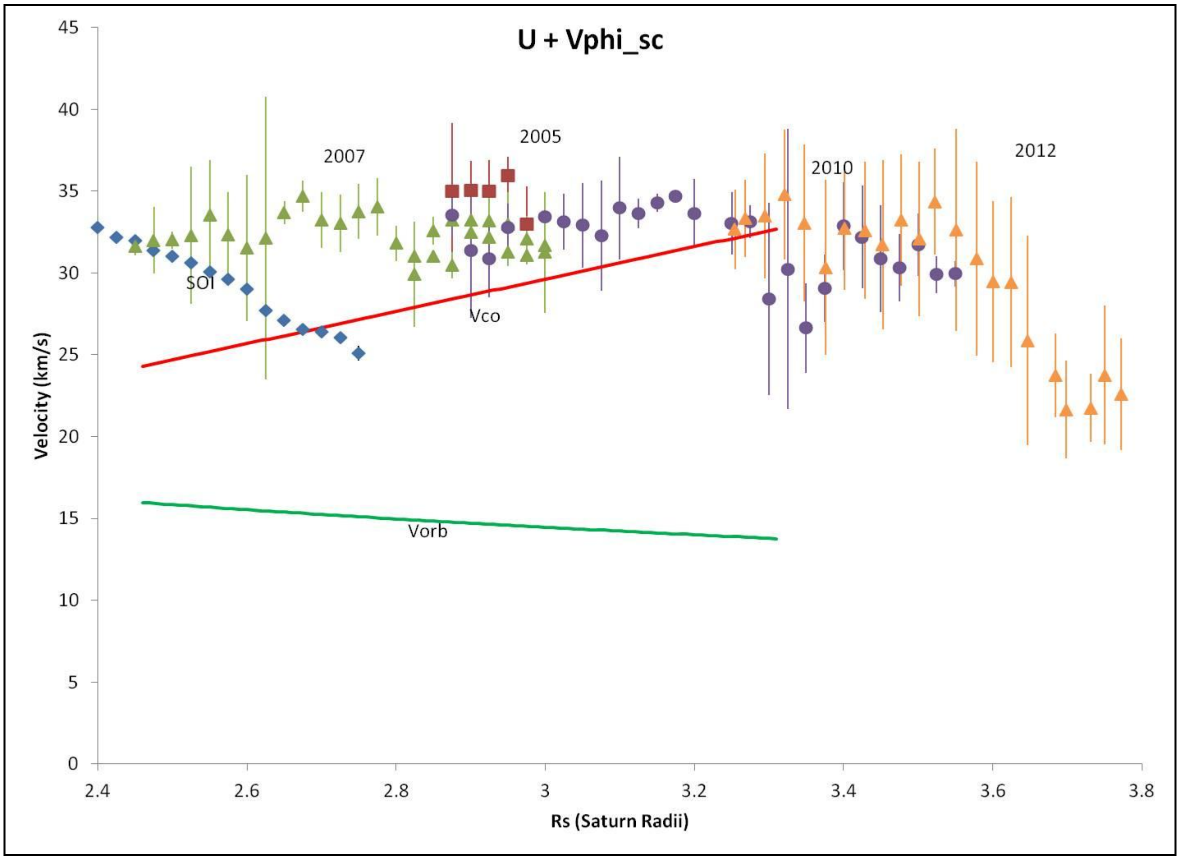

Figure 3.6-- Flow speed of the ions corrected for the V_ϕ component of the space craft velocity. V_{co} is the solid red line and V_{orb} is the solid green line. SOI is in blue diamonds, 2005 is in red squares, 2007 is in green triangles, 2010 is in purple dots, and 2012 is in orange diamonds. The speeds are close to corotation as expected. These are for the data within 0.05 Rs of the magnetic equator. Data are averaged over 0.05 Rs and the error bars are generated using one standard deviation over these steps.

Section 3.6—3D Fits: Anomalies and Errors

73] In section 2.5 I described how the 3D fits were calculated and the nine parameters used in determining the plasma parameters. With an increase in the number of parameters from five to nine when transitioning from the 1D fits to the 3D fits, the difficulty of obtaining a unique solution became significantly more uncertain. The fits obtained in Fig. 3.7 were all created using different initial conditions, and slightly different constraints. For simplicity these initial conditions and constraints are listed in table 3.1 and the results of the fits are listed in table 3.2.

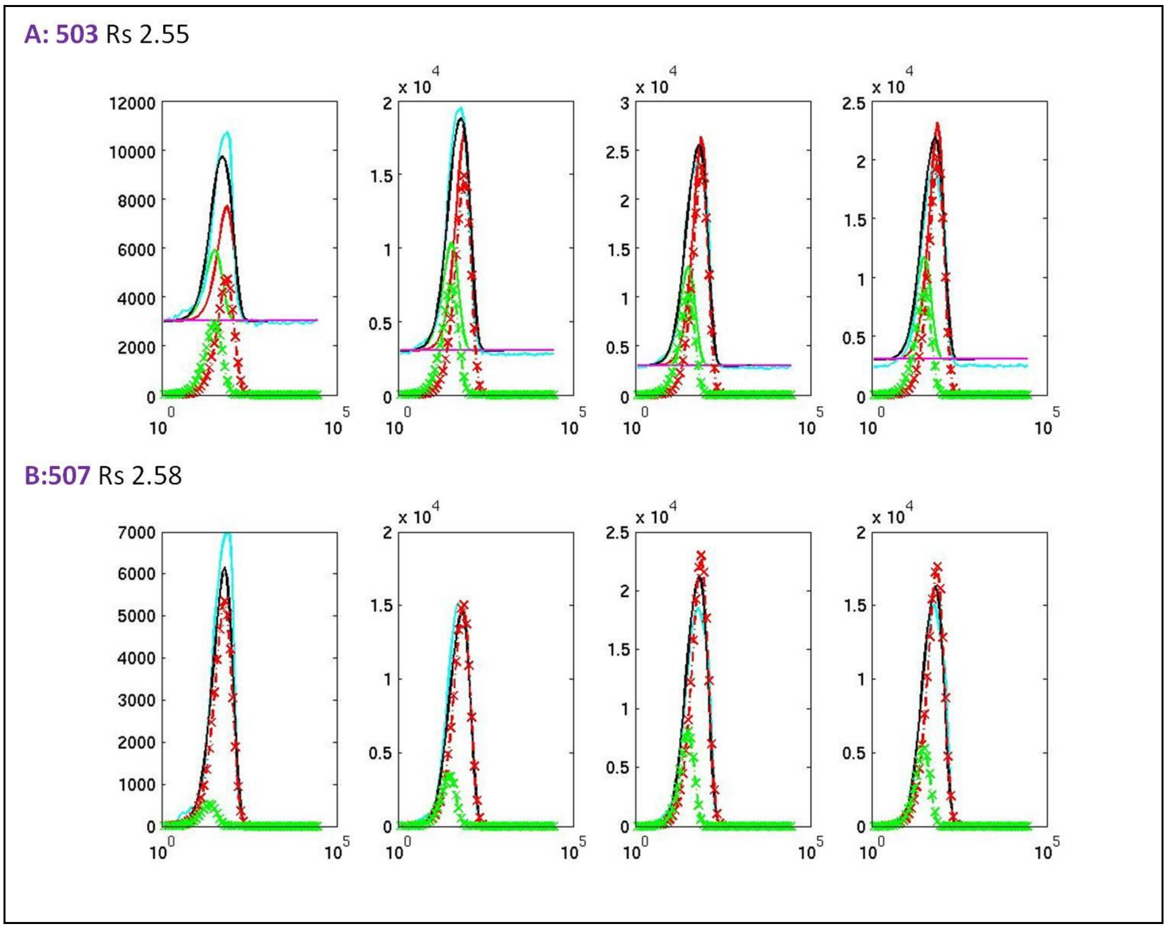

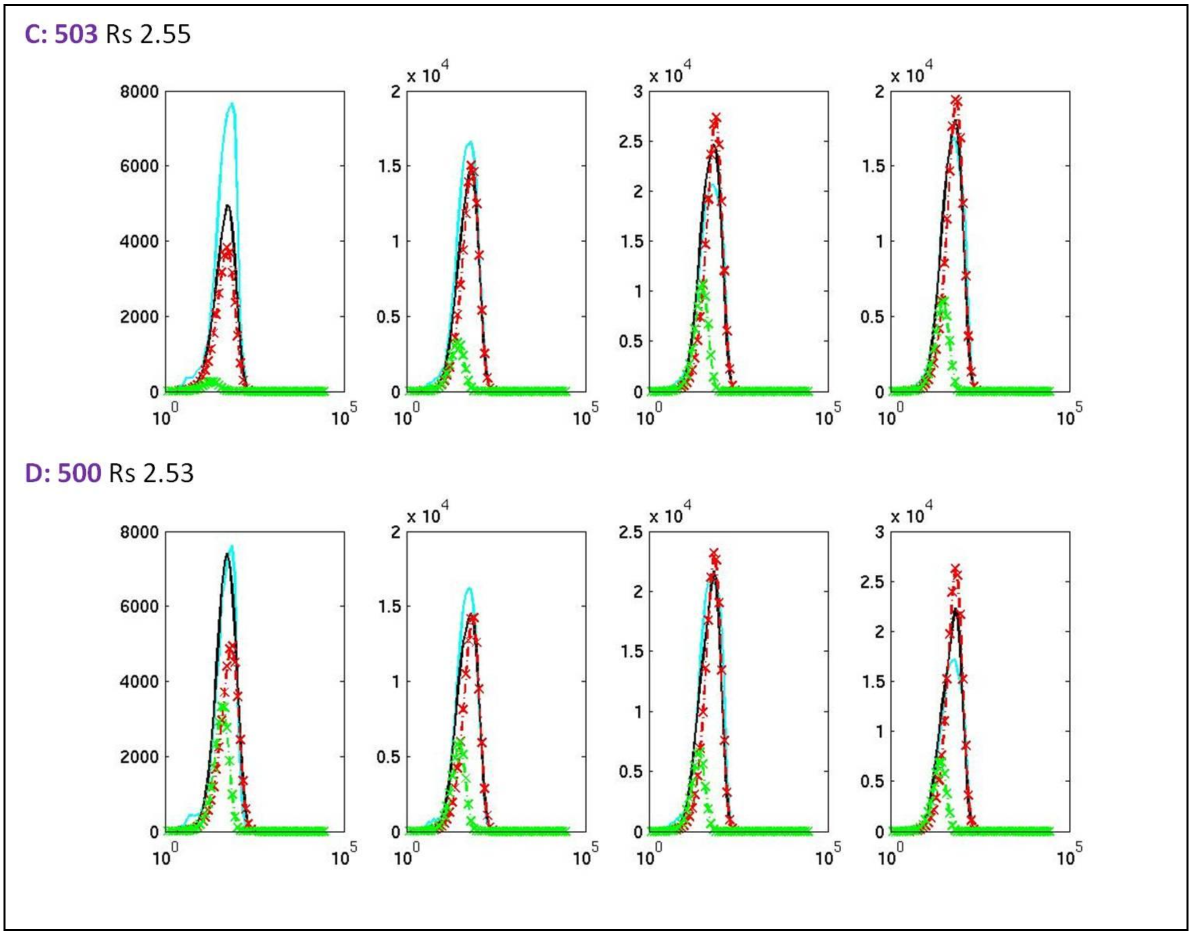

Figure 3.7—3D fits for anodes 5 through 8 of the SOI pass at 2.55 and 2.58 Rs. During this pass as the instrument was not actuating, anodes 1 through 4 were mostly background noise and therefore were not used. The cyan line is the data, black is the summed model fit, red is the O_2^+ ion fit and green is the O^+ ion fit, the returned fit parameters are printed above each, as well as in table 3.2. All four of these represent different initial parameters and different constraints on the fit parameters in an effort to obtain consistent and reasonable results as indicated in table 3.1 & 3.2.

Table 3.1—Initial conditions and Limits for 3D fits										
Test Acycle	nO2	nO	T_LO_2	$T_{\|\|}O2$	T_LO	$T_{\|\|}O$	Ur	Uϕ	Uθ	Anodes
A:init	300	100	17.4	15.6	8.21	0.75	0.0	0.0	Vco	All 8
Min	0	0	0.02* Tpick	0.2* T_L	0.02* Tpick	0.2* T_L	-Vco	-Vco	0.56* Vco	Fixed
Max	1E5	1E5	5* Tpick	0.2* T_L	5* Tpick	0.2* T_L	Vco	Vco	1.4* Vco	BKGD
B:init	558.9	194.3	0.75* Tpick	0.2* T_L	0.75* Tpick	0.2* T_L	0.0	0.0	Vco	ALL
Min	0.95*n_o	0.95* n_o	0.002* Tpick	0.1* T_L	0.002 * Tpick	0.2* T_L	-Vco	-Vco	0.2* Vco	Bkgd
Max	1.05*n_o	1.05* n_o	100.9* Tpick	0.8* T_L	100.9 * Tpick	0.2* T_L	Vco	Vco	2.0* Vco	Sub
C:init	558.9	176.7	0.65* Tpick	0.2* T_L	0.65* Tpick	0.2* T_L	0.0	0.0	Vco	6 TO 8
Min	0.95*n_o	0.95* n_o	0.002* Tpick	0.2* T_L	0.002 * Tpick	0.2* T_L	-Vco	-1.5	0.1* Vco	Bkgd
Max	1.05*n_o	1.05* n_o	100.9* Tpick	0.8* T_L	100.9 * Tpick	0.2* T_L	Vco	1.5	2.5* Vco	Sub
D:init	300	100	0.5* Tpick	0.5* Tpick	0.5* Tpick	0.5* Tpick	0.0	0.0	Vco	6 to 8
Min	0	0	0.01* Tpick	0.01* Tpick	0.01 * Tpick	0.01 * Tpick	-Vco	-0.325	0.55* Vco	Bkgd
Max	1E5	1E5	2* Tpick	2* Tpick	2* Tpick	2* Tpick	Vco	0.325	1.55* Vco	Sub

Table 3.1—Initial conditions and limits for 4 examples of 3D fits. V_{co} refers to the corotation velocity, Tpick refers to the pick-up temperature calculated for each species, and n_o refers to an initial input density determined by the 1D fits (section 3.2). As SOI had only strong signal for anodes 6 through 8 to reduce noise, I often chose to limit the fitting procedure by selecting only those anodes or by running it with all 8 anodes. The very

large values allowed for an effective 'unbound' case, as I expected the fitting program to converge to a solution well within these values.

Table 3.2—Results from SOI 3D fits

Acycle #	nO2	nO	$T_{L}O2$	$T_{\|\|}O2$	$T_{L}O$	$T_{\|\|}O$	Ur	Uϕ	Uθ	BKGD (an 7)	X^2
A: 503	150	127	18	3.61	8.72	1.33	-2.56	4.08	27.8	3020	12889.6
B 507	589	194	15.8	8.92	4.39	3.43	0.99	9.17	26.2	3630	13510.9
C:503	559	177	12	13.8	3.16	5.47	2.21	11	25.8	2930	21823.3
D:500	45	16.4	21.1	2.11	13.4	0.354	2.75	0.2	21.8	2790	26877.4

Table 3.2—Results from 3D fits. The four different fits have different initial conditions and occasionally different constraints on the fit parameters as outlined in table3.2. The large disparity in the results indicated a lack of confidence in the consistency in the returned plasma parameters. χ^2 was determined using the sum of all anodes (in use) subject to: $\Sigma(\text{data} - \text{model})^2/(\text{data})$.

74] Because these fits were all very similar in quality, but yielded very different results, drawing a conclusion based on any of these results was very difficult. When running a similar test with the 1D results, i.e. different initial conditions and constraints, my final results were all similar, building confidence in the model. However, the inability of the 3D model to return similar results from multiple iterations caused me concern about the ability of the model and the ability of this data set to converge to a correct solution.

75] The fact that during SOI the instrument was not actuating also led to difficulty when fitting this particular data set because the noise effectively limited the number of anodes collecting data to three instead of the normal eight. To get an accurate picture of the perpendicular and parallel temperatures it was best to have data from anodes nearly perpendicular to the plasma flow direction. The parallel temperatures are determined from anodes pointing along the field lines, which is off the plasma flow directions. The perpendicular temperatures are determined by anodes pointing perpendicular to the field lines which includes into the plasma flow direction. If the plasma flow is isotropic the perpendicular and parallel temperatures will be equal. If, however, it is anisotropic, like most of the plasma in Saturn's magnetosphere $T_{||}/T_{L}$ can be much less than one. In many regions of the magnetosphere it has been shown that the plasma temperatures tend toward a ratio of 1:5 for $T_{||}:T_{L}$ [*Johnson et al.,* 2006a]. Due to the lack of actuation for this pass, the only anodes available for determining $T_{||}$ were within ~ 20° of the plasma flow. Therefore, the other anodes obtain only a glimpse, but not a very accurate measure of flow along the field lines. As for the later passes, despite the fact that they were actuating throughout the passes, 2007 and 2010, the data are noisy enough that the off anodes again have very poor signal to noise ratio so that they too become nearly impossible to fit. The conclusion was that in order to obtain good 3D fits of the Singles CAPS data, it was necessary to have multiple anodes with sufficient signal to noise ratio. With the significant background, and the difficulty in getting sufficient signal to noise ratio in multiple anodes, it is unlikely that the 3D fits would be effective in this region. Therefore, for this thesis I will only use the analysis I performed on the 1D fits.

Section 4: Discussion of Neutral Models and Comparison with Ion Data

Section 4.1—Formation of Oxygen from Main Rings to Enceladus

76] The main rings of Saturn, as well as the F, G, and several other smaller rings, which are present in the region from 2.2 to 3.8 Rs, are predominantly composed of water ice particles. When UV light from the sun or energetic ions and electrons interact with the ice in this region, they can cause photo-decomposition producing neutral H_2 and O_2 (e.g. *Cassidy et al.,* 2010). Over the main rings especially, where the energetic plasma densities are low, the production of O_2 and H_2 is primarily due to the solar UV [*Johnson et al.,* 2006a]. Due to its lighter mass, the H_2 tends to spread out where it can be swept up by the planet or be scattered outward through the magnetosphere via collisions. The O_2, however, is much heavier and, therefore, is less readily dispersed. Over the main rings this results in the form of a fairly stable, thin atmosphere: the so called 'ring atmosphere' discovered during SOI by the CAPS instrument [*Tokar et al.,* 2005]. According to *Tseng et al.* [2010] the O_2 atmosphere remains bound to the rings within about 0.08 Rs (4800 km) of the ring plane. But due to the northern offset (by 1400 km) of Saturn's magnetic field, there is a slight asymmetry to the ions produced from the ring atmosphere. The neutral O_2 formed from the ring particles is lost primarily by photo-ionization and dissociation. However, it can also be dispersed beyond the rings where it interacts with the ice particles and is eventually ionized through photo-ionization, electron impact ionization, and ion-neutral collisions.

77] In addition to the O_2 produced through photo-decomposition of icy ring particles, the moon Enceladus has active geysers that emit a significant amount of water that permeates this region. As the water molecules are dispersed, they can be dissociated so that water molecules and radicals are deposited on the A, F, and G-ring particles and other ice grains throughout the region [*Cassidy and Johnson,* 2010]. Since dissociated species are precursors to the formation of O_2 in ice (e.g. *Johnson et al.* 2010), and this appears to occur preferentially in the near surface region [*Teolis et al.,* 2009] we assume that radicals deposited on the outer edges of the A-ring can react with the ice grains to enhance the production of O_2. Similarly, we have assumed that the dissociated O from O_2 over the rings can react with the ice grains and be recycled on ice particles back into O_2 [*Tseng and Ip*, 2011]. It is through a combination of the recycling on the ice grains and the photo-decomposition of these grains that it was possible to explain the CAPS measurements of O_2^+ and O^+ over the main rings. The atmosphere so produced then leads to a rather significant source of neutral O_2 scattered into the region of interest. However, as it is primarily produced by UV photons, this source is seasonal [*Tseng et al.* 2012].That is, it depends on the solar zenith angle as seen from the ring plane which changes throughout Saturn's orbit.

78] Unfortunately, due to the extremely low density of the neutrals in the region, they are nearly undetectable by our current Cassini in-situ instruments. Therefore, to verify the neutral models of the ring atmosphere and the Enceladus neutral torus, examination of the ion densities and ion formation in the region of interest is necessary. Ions are formed through three main processes: photo-ionization, ion-neutral charge exchange, and electron impact ionization. Due to the low density of the electrons in this region, and due to the relative velocities between ions and neutrals, photo-ionization dominates [*Thomsen et al*, 2010]. According to *Huber et al.* [1992], 80% of photo-ionizations of O_2 produce O_2^+ and an electron: Eq. 4.1. Thus, the ions created from this source will be predominately O_2^+ with about 20% being O^+.

$$O_2 + h\nu \rightarrow O_2^+ + e^- \ (80\%)$$

$$O_2 + h\nu \rightarrow O + O^+ + e^- \ (20\%) \qquad (4.1)$$

79] In the region I am studying, the ring atmosphere is not the only source of ions. The water group neutrals from the Enceladus torus are ionized producing a strong source of W^+ ions. Therefore, in this thesis I consider models that examine how the plume spreads outside of the Enceladus orbit [*Cassidy and Johnson,* 2010; *Smith et al.,* 2010]. I use the results from my analysis of CAPS data to compare to the neutral densities produced by the Enceladus models as well as the ring atmosphere models on which I collaborated [*Tseng et al.*, 2010; 2012]. In this way I can determine where the seasonally variable ring atmosphere is dominant over the water products from the Enceladus torus.

Section 4.2—Description of Neutral Cloud Model: Enceladus Models

80] Initial modeling of the Enceladus neutral cloud [*Johnson et al.*, 2006b; *Smith et al.*, 2010] considered ion-neutral scattering, charge exchange, and molecular dissociation to be the necessary elements to spread the neutrals in this cloud from their initial orbits into a larger and extended torus. However, because of the long lifetimes for the neutrals, *Farmer* [2009] and *Cassidy and Johnson* [2010] showed that neutral-neutral collisions were also essential for creating a complete model of the neutral torus created by Enceladus. Therefore *Cassidy and Johnson* [2010] created a model using a direct simulation Monte-Carlo (DSMC) model that incorporated all four processes: of ion-neutral scattering, charge exchange, molecular dissociations, and neutral-neutral interactions. This revised model showed that the Enceladus neutrals were spread farther than in previous models, and was in better agreement with the observed UVIS observations of O and electron data [*Melin et al.,* 2009; *Rymer et al.,* 2007; *Persoon et al*., 2006].

81] In addition, *Smith et al.* [2010] used the CAPS data to show that the Enceladus plumes may have a variable source rate. Through the use of three CAPS data encounters of Enceladus, labeled, E2, E3 and E5, *Smith et al.* [2010] showed that the plume source rate appeared to vary by approximately a factor of four over a seven month observational period in 2008. These findings indicated that previous estimates of the size of the plume sources, specifically from E2 were slightly over estimated. This possible variability has also been taken into account, as a lower bound, in my analysis.

Section 4.3—Description of Neutral Cloud Model: Ring Atmosphere

82] In the process of modeling the ring atmosphere I worked with colleague W. Tseng [*Tseng et al.,* 2010; 2012] to help produce a model that took into account the changing solar zenith angle of the rings, the recycling of the water products from Enceladus on the A-ring, ion-molecule charge exchange reactions, changes in the solar activity, the changes in temperature on the rings, and plasma chemistry in the region. Our initial model [*Tseng et al.,* 2010] examined the effects of the changing solar zenith angle and ion molecule exchange, in order to determine an initial estimate of spread of the ring atmosphere. The magnetic equator is offset from the ring plane by 0.04 Rs (2400 km) northward, which impacts the spatial distribution of ion production from the gravitationally bound neutral cloud and was taken into account in our efforts. This indicates that during SOI when the sun was illuminating the southern side of the ring plane, there would be a higher dispersion rate of ions throughout the region, than when the sun illuminated the northern side of the rings and the ions seemed to be more confined to the magnetic equator. Fig 4.1 from *Tseng et al.* [2010] shows how these distributions varied as the solar zenith angle changed from the south at SOI to the north.

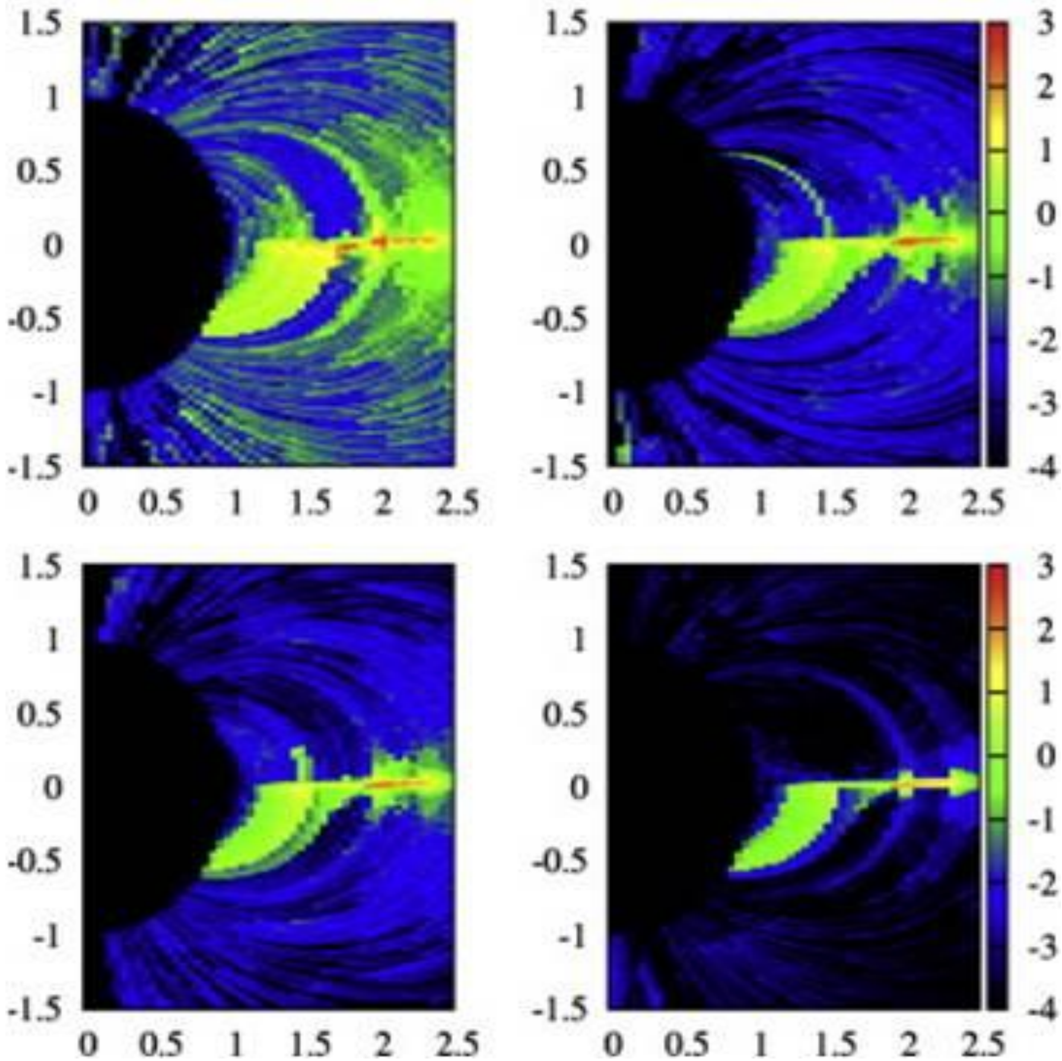

Figure 4.1—*Tseng et al.* [2010] model of ring atmosphere variations due to solar zenith angle. From top to bottom, the O_2^+ ion density for the solar zenith angle changing from 24° south (top left), 24° north (top right), 14° north (bottom left), and 4° north (bottom right). The color is number density (cm^{-3}) in a log scale.

83] *Tseng and Ip* [2011] considered the effect of water products from Enceladus deposited onto the icy ring particles which could increase the production of O_2 in the region of interest.

Combining this effect with the recycling of O on the ring particles described in Johnson et al. (2006a), the source rate over the main rings was increased by about a factor of 5 to 10 from previous estimates and became more consistent with my analysis of the CAPS densities in Fig 3.1. In order to explain the large variation observed in the CAPS ion densities between 2004 and 2010 we also took into account the observed temperature changes of the ring particles. CIRS data [*Flandes et al.*, 2010] showed that the surface temperature of the rings dropped from 100K to 60K from 2004 to 2009. While the ions stick and are re-neutralized when they collide with the ice grains, the neutrals are usually re-emitted into the atmosphere at the temperature of the ice grains. However at lower temperatures, O_2 has longer residence time on the grains and, more importantly, laboratory studies have shown that the radiation induced decomposition of ice is strongly dependent on its temperature [e.g. *Johnson* 2010]. Our revised ring atmosphere model took into account the effects of the changing ring particle temperature, the observed changes in solar activity level, and a simple one-box plasma chemistry model described below.

84] We developed a one-box ion chemistry model to simulate the plasma environment between 2.5 and 3.5 Rs near the equator. The model is described by the following parameters: the neutral densities, the diffusion loss timescale, and the density and temperature of hot electrons. The ionization, recombination, and charge exchange for the major neutral torus species (W, H, H_2, and O_2) are also accounted for in the model. The output was the steady state plasma composition (W^+, H^+, H_2^+, and O_2^+). These are obtained from chemical rate equations for plasma density. A set of equations like that in Eq. 4.2, is solved for a set of initial test parameters, where n_i is the ion density, S_i is the source rate, and L_i is the loss rate for a type of ion, i. To determine S_i and L_i we took into account the surface temperature of the rings, the solar activity level at both SOI and at equinox (2010) and the solar zenith angle with the ring plane. Table 1 from *Tseng et al.* [2012] describes the various sources rates determined by taking these factors into consideration. In addition the appendix 1 from *Tseng et al.* [2012] details how the loss rates were determined as well as the appropriate chemical rate equations as the applied to the generic equation, Eq. 4.2.

$$\frac{dn_i}{dt} = S_i - L_i, \qquad 4.2$$

85] The ion sources are photo-ionization, electron-impact ionizations (both thermal and hot electrons), and charge exchange reactions with the neutrals. Loss occurs by charge exchange, radial diffusion, and recombination. The time-dependant equations for the ions were solved iteratively using the fourth order Runge-Kutta method until steady-state is reached.

86] As stated earlier, primary ion source in this region is photo-ionization, while the hot electron impact ionization can only account for ~30%. Inside of ~4 Rs, the radial diffusion is ~ 1-2 months [*Rymer et al.*, 2009] so it is not a major loss process for plasma. However, due to the low electron temperatures [*Lewis*, private communication], recombination which is on the order ~ 6 to 15 months (see table A4 from *Tseng et al.* [2012]) is a major loss process in agreement with *Sittler et al.* [2008].

87] As a result, we were able to create a comprehensive model of the ring atmosphere in the region between the main rings and Enceladus. Unlike the *Cassidy and Johnson* [2010] model for the Enceladus torus, the ring atmosphere model did not include neutral-neutral collisions, and it remains to be seen if this is a significant factor in the determining of the distribution of the O_2 neutrals. Future work would include this effect. Fig. 4.2 shows a comparison of the neutral column densities from the *Tseng et al.* [2012] ring atmosphere model. The highest level is at solstice and the lowest level is at equinox. Also shown is the *Cassidy and Johnson* [2010] Enceladus torus, included in this figure as a dashed line which is a lower bound allowing for the factor of four variation expected by the *Smith et al.* [2010] model.

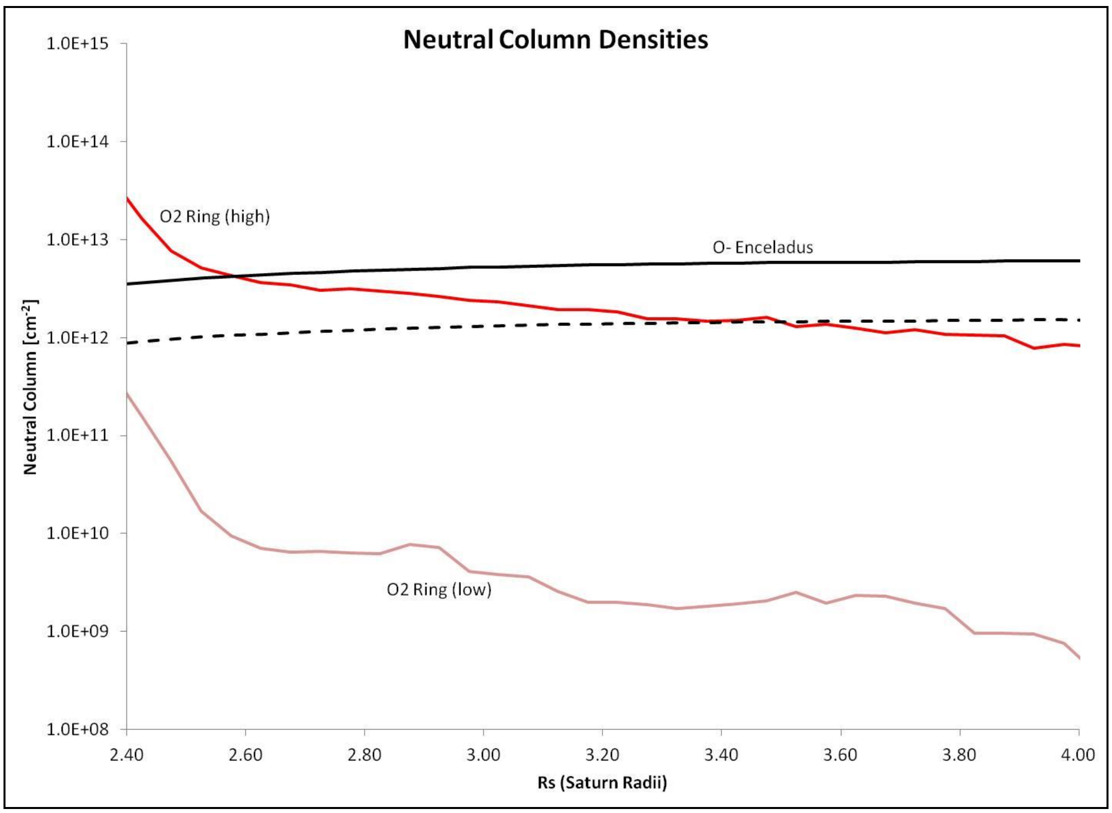

Figure 4.2—Neutral columns densities from the models for the Enceladus torus and the ring atmosphere. The higher ring atmosphere column densities are at solstice and the lower are at equinox [*Tseng et al.,* 2010; 2012]. The solid black line is the column density for the Enceladus torus from *Cassidy and Johnson* [2010] and, the dashed line indicates a lower bound on the Enceladus torus due to a factor of four variation in the plume source [*Smith et al.,* 2010].

Section 4.4—Ion Column Density and Comparison with Models

88] Because the ion data are often taken from various locations above and below the ring plane, and the ion density drops off farther away from the magnetic equator, it is necessary to calculate the ion column densities using the scale height for each ion species, H_i, in Eq. 4.3. Assuming the loss rates for each ion species are comparable and vary only slowly with R, I will compare the ion column density, to the neutral column densities in order to help determine how these sources produce plasma in the region of interest. Using the scale height and Eq. 4.4, it is then possible to calculate the column density, N_i for each species using the vertical distance from the magnetic equator, z, at which I analyzed the data, ion density, n, at that position, and the ion temperature T_i, and the rotational velocity of Saturn, Ω [*Johnson et al.,* 2005a; *Hill et al.,* 1976]. Given that this region is so close to the planet, this column density was determined by assuming the magnetic field is an approximate dipole and that most ions are formed near the ring plane.

$$H_i = \sqrt{\frac{2kT_i}{3m_i\Omega^2}} \qquad (4.3)$$

$$N_i = \sqrt{\pi}n_i exp\left(\left(\frac{z}{H_i}\right)^2\right)H_i \qquad (4.4)$$

89] In Fig. 4.3 I display the column densities for the individual ion species using my results for SOI to 2012 and Voyager 2. The solid shapes are O_2^+ and the open shapes are O^+. The SOI column density is dominated by the O_2^+ whereas the later data have a ratio of O_2^+/W^+ that is closer to one.

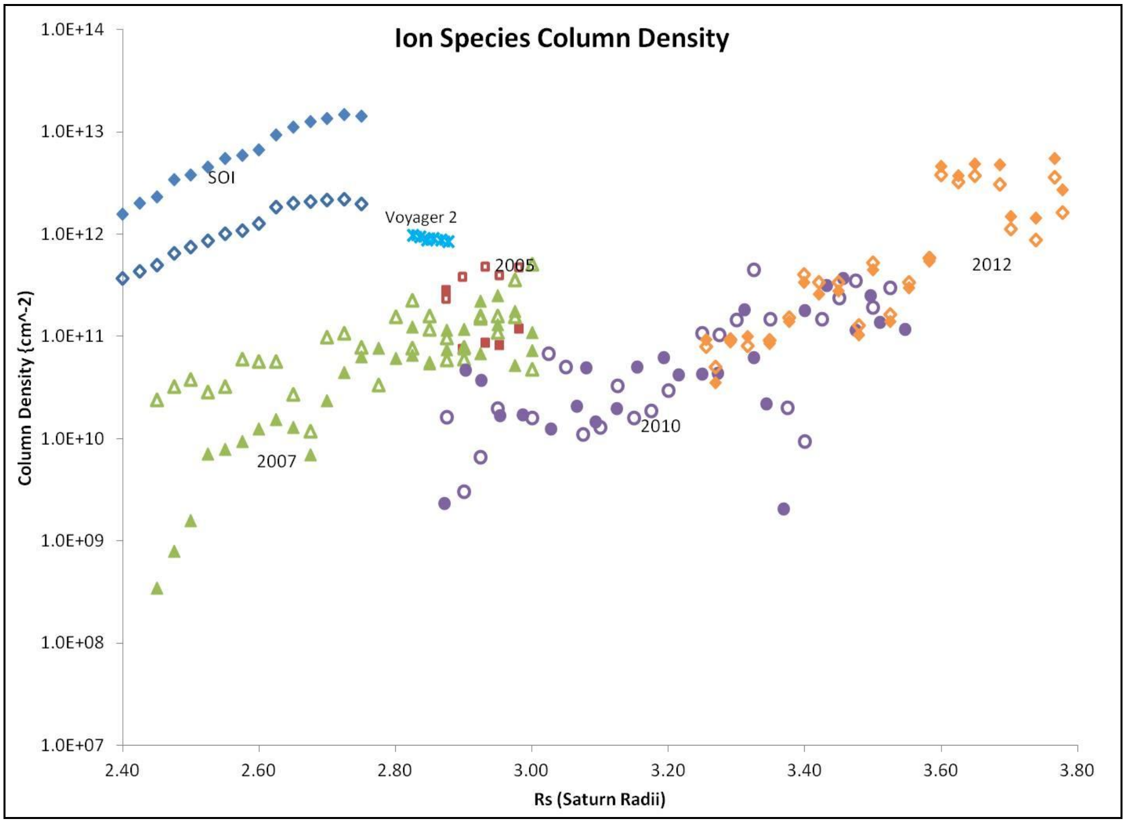

Figure 4.3—Ion column densities for each species. Open shapes indicate O^+ closed shapes indicate O_2^+. Blue diamonds are SOI, green triangles are 2007, red squares are 2005, purple dots are 2010, orange diamonds are 2012 and teal crosses are Voyager 2.

90] Although the calculated modeled neutral O_2 column densities from the ring atmosphere are smaller than the modeled O or OH neutral column densities from Enceladus throughout much of the region as seen in Fig 4.4a, there is a point inside 3.6 Rs where the seasonal effect seems more pronounced than the Enceladus torus. I note that the ion column densities have a two orders of magnitude drop from SOI to 2007 and lower again to 2010. This much larger drop from solstice at SOI to equinox near 2007 and 2010 is much more consistent with the ring atmosphere model between 2.4 Rs and 3.6 Rs than with the Enceladus models. The 2010 data seems to be the lowest point, as the 2012 data seems to be rising again from the 2010 data. However, since most of the 2012 data was taken close to Enceladus, the radial increase in the column density could be from the neutral torus. Fig. 4.4b compares the equatorial densities of both the neutrals and the ions. We find that the neutral O_2 is higher than O near the equator due to scale height, which is consistent with the analysis here, i.e. that model O_2^+ ion density is the dominant ion at SOI. The model O_2^+ ion density [*Tseng et al.,* 2010] is about a few hundred cm^{-3} at SOI in rough agreement with CAPS data in Fig 3.4a.

91] Fig. 4.4a compares the neutral column densities with the ion column densities. The SOI, data have a closer agreement with the ring atmosphere model than with the Enceladus model, and the drop between SOI and 2007, and 2010 agrees with the seasonal effects modeled by *Tseng et al.* [2010, 2012]. However, the trends that all the data show of increasing toward Enceladus support the strong influence from the water source from Enceladus. By 2012 at around 3.7 Rs the data are much closer to the Enceladus models [*Cassidy and Johnson,* 2010; *Smith et al.,* 2010; *Tseng et al.,* 2010; 2012].

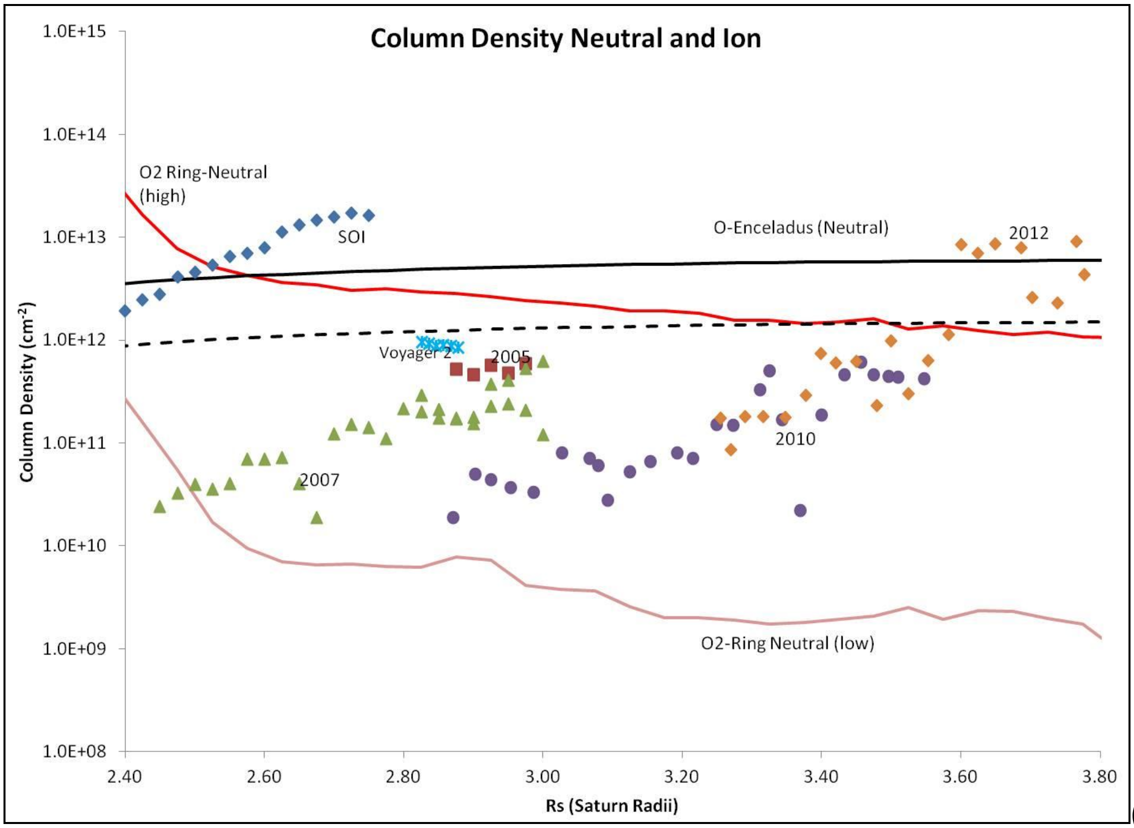

Column Density Neutral and Ion
Column Density (cm^{-2})
Rs (Saturn Radii)
1.0E+15
1.0E+14
1.0E+13
1.0E+12
1.0E+11
1.0E+10
1.0E+09
1.0E+08
2.40
2.60
2.80
3.00
3.20
3.40
3.60
3.80
O2 Ring-Neutral (high)
SOI
O-Enceladus (Neutral)
2012
Voyager 2
2005
2007
2010
O2-Ring Neutral (low)

(a)

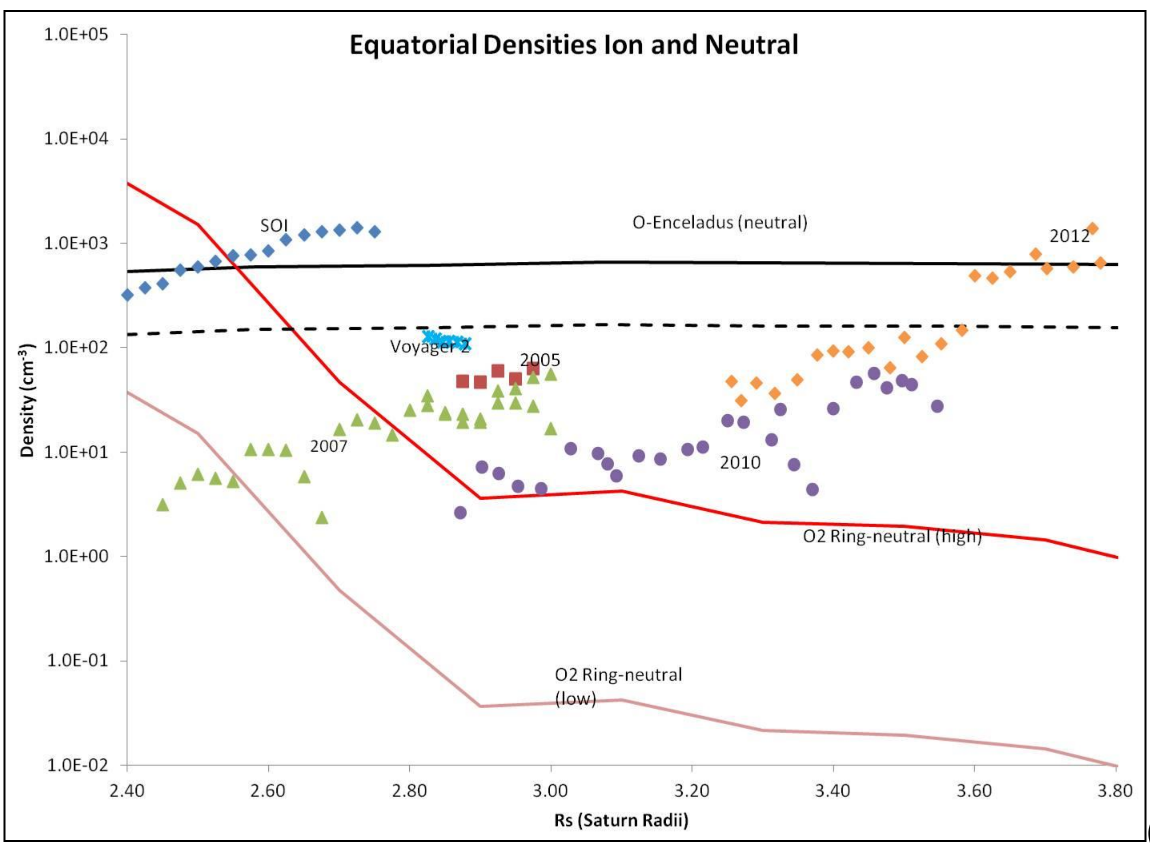

Equatorial Densities Ion and Neutral
Density (cm^{-3})
Rs (Saturn Radii)
1.0E+05
1.0E+04
1.0E+03
1.0E+02
1.0E+01
1.0E+00
1.0E-01
1.0E-02
2.40
2.60
2.80
3.00
3.20
3.40
3.60
3.80
SOI
O-Enceladus (neutral)
2012
Voyager 2
2005
2007
2010
O2 Ring-neutral (high)
O2 Ring-neutral (low)

(b)

Figure 4.4—(a) Total ion column densities summed for each pass, Voyager 2 was only O^+. Blue diamonds are SOI, green triangles are 2007, red squares are 2005, purple dots are 2010, orange diamonds are 2012 and teal crosses are Voyager 2. Neutral O from Enceladus is in the black solid line [*Cassidy and Johnson,* 2010]; ring atmosphere sourced from southern solstice (high) in red and equinox (low) in pink [*Tseng et al.,* 2010; 2012]. (b) Equatorial ion densities from the same passes compared with the ring atmosphere and the Enceladus torus equatorial densities with the lower bound [*Smith et al.,* 2010] in the dashed line.

92] The extended O_2 ring atmosphere in our region at equinox in Fig. 4.1 is seen to be about one percent of the atmosphere at southern solstice. Thus, near equinox, our model O_2^+ ion density is ~5 - 10 cm^{-3} while an average Enceladus torus source, the total water group ion density is ~10-20 cm^{-3}. This result is also remarkably consistent with the data shown in Fig 3.4 and indicates that unless the ring atmosphere contribution of O_2 is large, as at SOI, the O_2^+ is formed primarily from the ion-molecule collisions between OH^+ and O. We have also shown that the lifetime of the ions is short, which is consistent with our observation that the O_2^+ temperatures at SOI are close to the pick-up temperature. On the other hand, when the ring atmosphere contribution is small most ions have experienced a number of relatively low speed ion-neutral collisions, each of which can reduce the ion temperature [*Johnson et al.,* 2006a; *Tseng et al.,* 2012]. This explanation could account for ion temperatures being well below the pick-up temperatures in the data closer to equinox (2007 – 2010), although interactions with the charged grains in the E, F, G rings, as well as the smaller rings and moons responsible for the ice grains throughout the region could also contribute.

Section 4.5—Conclusions from Ion Data and Model Comparison

93] The seasonal variation in the ring atmosphere described in *Tseng et al.* [2010] and updated in *Elrod et al.* [2012] and *Tseng et al.* [2012] by accounting for the effect of the change in temperature on the decomposition of ice, the plasma chemistry within the region, and the solar activity level have allowed me to estimate the ion formation rates in the region of interest. Due to considerable uncertainties in the importance of recycling of radicals on the icy ring particles, we re-normalized the ring atmosphere to CAPS O_2^+ data at SOI. This pass, which occurred close to solstice, resulted in the highest O_2 densities in Fig. 4.2, about two orders of magnitude higher than our estimate at equinox.

94] The Enceladus plume source may also experience variations, but these have been estimated to be only about a factor of four over a seven-month observational period [*Smith et al.,* 2010]. This variability has not been verified in UVIS observations; therefore it is possible that the Enceladus plumes are less variable over the long term as has been suggested [*Hansen et al.,* 2011]. In principle, larger variations could occur, but it has been shown that the source rate is relatively stable as the E-ring, which is also produced by the Enceladus geysers, was present during the Voyager 2 pass, and an OH torus discovered between Voyager and Cassini, appeared to be relatively stable [*Jurac et al.,* 2001] and consistent with recent estimates of the neutral column density [*Johnson et al.,* 2006b]. In effect the Enceladus plume is considered to be much less variable than the ring atmosphere.

95] Given the relative stability of the Enceladus model [*Cassidy and Johnson,* 2010; *Smith et al.,* 2010; *Hansen et al.* 2011] and the two order of magnitude drop in the ring atmosphere model [*Tseng et al.,* 2010; 2012], my ion data appear to confirm that the ring atmosphere exhibits a significant seasonal variability. That is, my examinations of the CAPS data from the edge of the main rings at about 2.2 Rs to about 3.6 Rs support the idea of a seasonally variable atmosphere and O_2^+ and O^+ plasma. The plasma appears to begin to be dominated by the Enceladus source around 3.7 Rs. In addition, as Saturn approaches equinox, the ring atmosphere decreases in importance and the region is dominated by the Enceladus torus. Although the 2012 results occur well after equinox the solar zenith and the distance from Saturn are such that the Enceladus torus dominates in the region covered by this data set. Therefore, the observed increase could be due to variability in the Enceladus source, or more likely, the seasonal increase in the ring atmosphere contribution.

Section 5: Summary and Conclusion

Section 5.1—Summary

96] To determine the plasma density temperature, bulk flow velocity and composition, and how these characteristics have changed over time from over the main rings and into the region outside of the main rings from 2.2 Rs to 3.8 Rs, I used Cassini Plasma Spectrometer and Voyager 2 plasma data. By analyzing the data selected from 2004 to 2012, in addition to the Voyager 2 data from 1986, I showed for the first time that there is a seasonal variation of the O_2^+ and O^+ plasma in this region. This in turn led me to conclude that the ring atmosphere is seasonal, confirming the hypothesis in *Johnson et al.* [2006a] that the oxygen is very likely to be produced by photo-decomposition of ice by solar UV.

97] In the work for this thesis, I first created 1D and 3D algorithms to analyze the data from the CAPS instrument to extract the plasma parameters. Considering the significant penetrating radiation throughout the region I also determined effective methods for measuring and adjusting for the background. I then analyzed CAPS data taken from 2004 -2012. Once I determined the plasma parameters for each of the passes, I then compared the resulting ion densities to models of the neutral sources from the ring atmosphere and the Enceladus plumes [*Cassidy and Johnson,* 2010; *Smith et al.,* 2010; *Tseng et al.,* 2010; 2012]. This confirmed my hypothesis that the observed plasma exhibited a significant seasonal variability. This process is reviewed below.

Section 5.2—Summary of Data Analysis Methods

98] To extract the plasma parameters from the CAPS data I created a 1D plasma data analysis technique. This technique required that I determine the anode pointing nearest to the plasma flow, and select A-cycles exhibiting clear peaks above the high penetrating radiation in the region. To effectively measure the background, I treated it as a fit parameter. The result was the returned values of ion density, composition, temperature, and the bulk flow velocity. This model does not return the perpendicular and parallel temperature associated with the gyro-motion of the ions around the field lines, nor does it return the full 3D components of the flow velocity. This can only be determined through the full 3D moments.

99] I also developed a full 3D moment model in an attempt to determine the perpendicular and parallel temperatures as well as the three velocity components. The full 3D model requires the use of multiple anodes. In this noisy region, however, it is difficult to obtain data with a sufficient signal to noise ratio from anodes pointing away from the plasma. To obtain a solution for both the perpendicular and parallel temperatures, as is the goal of this model, it is necessary to have a viable signal from multiple anodes. In this region, however, because of the high background, most of the off anodes (i.e., anodes pointing away from the plasma flow), did not register strong enough peaks above the noise to be very useful. As a result, the model was unable to converge to a solution and the results were deemed unreliable.

Section 5.3—Summary of Data Analysis Results

100] The ion densities in Fig. 3.3b as well as the electron densities in Fig. 3.5, indicate that there was a significant change in the plasma densities in this region from 2004 to 2010. The plasma also seems to be rising again from 2010 to 2012; however most of the 2012 data was taken much closer to Enceladus so that the increase was well within the variability in the Enceladus out gassing suggested by *Smith et al.* [2010]. The plasma also appeared to change in character over the period studied as the relative composition and the ion temperatures also varied considerably, as shown in Figs. 3.6 and 3.7. I also note that the higher than normal background for SOI indicates there were higher levels of penetrating particle radiation at that time. If only Cassini data were available, then the SOI data might be considered anomalous. However, the Voyager 2 data within 0.05 Rs (3000 km) of the magnetic equator was also much higher than the 2007 and 2010 data. In addition, the 2012 data, where it overlaps with the 2010 data, is slightly higher than the 2010. The *Tseng et al.* [2010] model predicts that these levels could be approximate to the 2005 levels if this plasma is subject to the seasonal effects. Therefore, my results suggest that the significant variations in the plasma density, composition, and temperature have occurred which appear to be consistent with the predicted seasonal variation in the extended ring atmosphere from solstice to equinox rather than the variability of the Enceladus source. The 2012 data, likely dominated by the Enceladus source, might also include a seasonal effect.

Section 5.4—Summary of Ion Data Comparison with Neutral Modeling

101] Since the formation of the neutrals and ions from the main rings has been suggested to be mainly due to solar UV photons, the production rate will depend on the angle of incidence of the solar flux with the ring plane, the ring particle temperatures, and the level of solar activity. In 1981, when Voyager 2 encountered the Saturn system, the Sun was near solar maximum and Saturn was near equinox making a low incidence angle. In 2004, for the SOI pass, Saturn was at southern solstice so the incident angle with the southern half of the ring plane was at its largest and the solar activity was average. In addition, late in 2003 there was a unique short period of high solar activity that might have had a sustained effect. By 2010, Saturn was near equinox again so the illumination of the rings was at a minimum. However, by 2006 the solar activity had reached a minimum, possibly affecting the later passes, and it did not return to normal activity until mid 2011.

102] In *Tseng et al.* [2010] we described the variation with solar incident angle of the O_2 component of the ring atmosphere accounting for the reduced UV flux as equinox approached, which affects the oxygen production rate. Data taken from Composite Infrared Spectrometer (CIRS) and ring occultation data [*Flandes et al*., 2010], indicate that the average ring particle temperature dropped from ~100 K at southern solstice in 2004 to ~60K at equinox. This drop in temperature dramatically affects the photo-decomposition rate for ice, as well as the chemical reaction rates on the ice grains, and hence, the ring atmosphere density.

103] In section 4 I described the models used to calculate the neutral sources from which the plasma ions are formed in this region. Fig 4.2 has neutral densities from *Cassidy and Johnson* [2010], *Smith et al.* [2010], and *Tseng et al*. [2010; 2012] models. The Enceladus models include the neutral-neutral collisions and ion-neutral collisions, and they have been normalized to the observational data. In Fig 4.2 I also include a lower boundary to account for the possible variations of the plume sources [*Cassidy and Johnson,* 2010; *Smith et al.,* 2010]. The ring atmosphere model includes solar zenith level, ring temperature, spreading due to ion-molecule collisions, interactions with the dust grains, solar activity angle, and plasma chemistry [*Tseng et al.,* 2010; 2012].

104] The ring atmosphere normalized to my analysis of CAPS O_2^+ data at SOI resulted in the highest O_2 densities in Fig. 4.3. These are about two orders of magnitude higher than at equinox. The modeled neutral densities included the effect of the deposition of dissociated neutrals [*Tseng and Ip,* 2011] and ions [*Farrell et al.,* 2009] from Enceladus onto ice particles in the A-ring, which can enhance the production of O_2. However, such an enhancement, which requires the production of O_2 from radical reactions on the grains, is also less efficient with decreasing ring particle temperatures when Saturn approaches equinox.

105] The Enceladus plume source might experience a variation of about a factor of four over a seven-month observational period [*Smith et al*., 2010]. These variations are small in comparison to the seasonal variations observed in ring atmosphere models. In addition, the average ion ratio calculated in the *Tseng et al*. [2012] model, were consistent with the ratios of O_2^+/W^+ reported in Fig 3.4b.Therefore, the seasonal variation in the ring atmosphere model is consistent with the variations in the ion densities from 2.2 Rs to 3.6 Rs.

Section 5.5—Summary, Conclusions, and Future Work

106] In conclusion, it is the two order magnitude drop in densities between SOI in 2004 (solstice) and 2007 (equinox) and possible increase, inside of 3.7 Rs, again in 2012 that indicates the temporal variations in the plasma in this region are likely to be primarily a seasonal effect. Despite the strong, continuous water source from the Enceladus plumes, the ring atmosphere has been shown to have a significant influence over this region. From approximately 2.2 to 3.6 Rs the variability in the plasma ion density appears to be influenced mainly by the variable ring atmosphere; starting around 3.7 Rs the region appears to be more influenced by the Enceladus torus.

107] Future work could include modifying our model in *Tseng et al.* [2012] to include neutral-neutral collisions within the ring atmosphere. In addition, this study did not take into account the Cassini spacecraft electric potential and its impact on the ion data. According to measurements made by the ELS whenever the spacecraft moves within 5 Rs, the spacecraft electric potential becomes negative, which could affect the detection of ions. And finally, if the CAPS instrument returns to a functioning state in the next year, it is possible that new data obtained in 2014, 2015, and especially 2017, when the spacecraft is due to pass directly over the rings again, could lend additional insight into the seasonal variability of the region.

108] While current models of the ring atmosphere do not account for neutral-neutral collisions as the *Cassidy and Johnson* [2010] model does, it is possible this cloud could spread farther outward than currently predicted. However, current models do include interactions with dust grains and the icy rings, which are prominent throughout the region. It is likely that the interaction with the ice and dust grains in the regions will outweigh any neutral-neutral collisions.

109] The spacecraft electric potential changes the net charge of the spacecraft from and overall positive charge throughout the majority of the magnetosphere to a net negative charge inside of 5.5 Rs from photoelectrons near Saturn. Therefore, a 1D model is currently in development to take into account the change in electric potential and the effect it has on the detection of ions [*Levi et al.,* in progress]. Preliminary findings have shown that a negative spacecraft electric potential could increase the measured ion population, as much as a factor of 2 to 4. Even if one accounts for a factor of four increase in the counting of ions at SOI, there is still a significant drop from SOI to 2007 and 2010. Future work could, however, examine this data with a newly developed model that accurately takes the spacecraft electric potential into account.

110] In 2014 and 2015, Cassini has a few orbits with close periapses scheduled that could potentially gather further information on this region. In addition in 2017, at the end of mission, there are several orbits where Cassini will pass successively over the main rings until it crashes into the planet's atmosphere. If CAPS returns to operation by this time, it is possible that data taken from these passes could confirm the seasonal variability hypothesis as Saturn approaches northern solstice in 2017. If, however, CAPS were unable to return to operation by the time of these passes, it is possible that some further confirmation could be obtained by examination of data through MIMI, INMS, or possibly RPWS data. One current study of MIMI data has also shown seasonal variations in the O_2^+ and mass 28 ions from around 3.5 Rs through 20 Rs [*Christon et al.,* submitted]. This indicates that MIMI and specifically the Charge Energy Mass Spectrometer (CHEMS) subsystem could also be used to study varying seasonal plasma processes.

Bibliography

Bouhram, M., R. E. Johnson, J.-J. Berthelier, J.-M. Illiano, R. L. Tokar, D. T. Young, and F. J. Crary (2006), A test-particle model of the atmosphere/ionosphere system of Saturn's main rings,*Geophys. Res. Lett.*, *33*, L05106, doi:10.1029/2005GL025011.

Bunce, E. J., S. W. H. Cowley, D. M. Wright, A. J. Coates, M. K. Dougherty, N. Krupp, W. S. Kurth, and A. M. Rymer (2005), In situ observations of a solar wind compression-induced hot plasma injection in Saturn's tail, *Geophys. Res. Lett.*, 32, L20S04, doi:10.1029/2005GL022888.

Burger, M. H., E. C. Sittler Jr., R. E. Johnson, H. T. Smith, O. J. Tucker, and V. I. Shematovich (2007), Understanding the escape of water from Enceladus, *J. Geophys. Res.*, 112, A06219, doi:10.1029/2006JA012086.

Cassidy, T., P. Coll, F. Raulin, R.W. Carlson, R.E. Johnson, M.J. Loeffler, K.H. Hand, R.A. Baragiola, (2010) Radiolysis and photolysis of icy satellites surfaces: Experiments and theory, *Space Sci Rev.,* DOI 10.1007/s11214-009-9625-3 .

Cassidy, T. A., R.E. Johnson, (2010), Collisional spreading of Enceladus' neutral cloud, *Icarus*, Volume 209, Issue 2, Pages 696-703, ISSN 0019-1035, 10.1016/j.icarus.2010.04.010.

Cassidy, T.A. and R.E. Johnson, A.R. Hendrix, (2011), Collisional Evolution of the Enceladus Neutral Cloud, *27th International Symp on Rarefied Gas Dynemics*, AIP Conf. Proc. 1333, 1133-1138 doi: 10.1063/1.3562796.

Christon, S., D. Hamilton, D. Mitchell, R. DiFabio, S. Krimigis, (2012) Saturn suprathermal O_2^+ and mass-28^+ molecular ions: Seasonal and long term variation, *J. Geophys. Res.* Submitted.

Coates, A.J., G.H. Jones, G.R. Lewis, A. Wellbrock, D.T. Young, F.J. Crary, R.E. Johnson, T.A. Cassidy, T.W. Hill, "Negative ions in the Enceladus plume", *Icarus* 206, 618-622 (2010) .

Coates, A.J. et al., "Plasma electrons above Saturn's main rings: CAPS observations", *GRL* 32, L14S09, doi:10.1029/2005GL022694(2005).

Cuzzi, J., R. Clark, G. Filacchione, R. French, R. Johnson, E. Marouf, and L. Spilker, "Ring Particle Composition and Size Distribution", Chapter 15 in *Saturn from Cassini-Huygens* (ed. M.K. Dougherty) pp459-509 (2009).

Elrod, M. K., W.-L. Tseng, R. J. Wilson, and R. E. Johnson (2012), Seasonal variations in Saturn's plasma between the main rings and Enceladus, *J. Geophys. Res.*, *117*, A03207, doi:10.1029/2011JA017332.

Farmer, A. J., (2009), Saturn in hot water: Viscous evolution of the Enceladus torus, *Icarus*, Volume 202, Issue 1, Pages 280-286, ISSN 0019-1035, 10.1016/j.icarus.2009.02.031.

Farrell, W. M., M. L. Kaiser, D. A. Gurnett, W. S. Kurth, A. M. Persoon, J. E. Wahlund, and P. Canu (2008), Mass unloading along the inner edge of the Enceladus plasma torus, *Geophys. Res. Lett.*, *35*, L02203, doi:10.1029/2007GL032306.

Farrell, W.M., W.S. Kurth, D.A. Gurnett, R.E. Johnson, M.L. Kaiser, J.-E. Wahlund, and J.H. Waite Jr., (2009), Electron density dropout near Enceladus in the context of water-vapor and water-ice, *GRL* 36, L10203, doi:10.1029/2008GL037108, 2009.

Farrell, W. M., W. S. Kurth, R. L. Tokar, J.-E. Wahlund, D. A. Gurnett, Z. Wang, R. J. MacDowall, M. W. Morooka, R. E. Johnson, and J. H. Waite Jr. (2010), Modification of the plasma in the near-vicinity of Enceladus by the enveloping dust, *Geophys. Res. Lett.*, *37*, L20202, doi:10.1029/2010GL044768.

Flandes, A., L. Spilker, R. Morishima, S. Pilorz, C. Leyrat, N. Altobelli, S. Brooks, S. G. Edgington, (2010), Brightness of Saturn's rings with decreasing solar elevation, *Planetary and Space Science*, Volume 58, Issue 13, Pages 1758-1765, ISSN 0032-0633, 10.1016/j.pss.2010.04.002.

Fletcher, L. N., R. K. Achterberg, T. K. Greathouse, G. S. Orton, B. J. Conrath, A. A. Simon-Miller, N. Teanby, S. Guerlet, P. G.J. Irwin, F.M. Flasar, (2010) Seasonal change on Saturn from Cassini/CIRS observations, 2004–2009, *Icarus*, Volume 208, Issue 1, Pages 337-352, ISSN 0019-1035, 10.1016/j.icarus.2010.01.022.

Hansen, C. J., et al. (2011), The composition and structure of the Enceladus plume, *Geophys. Res. Lett.*, *38*, L11202, doi:10.1029/2011GL047415.

Hansen, C. J., et al. (2006), Enceladus' water vapor plume, *Science*, *311*, 1422–1425, doi:10.1126/science.1121254.

Hill, T. W., and F. C. Michel (1976), Heavy Ions From the Galilean Satellites and the Centrifugal Distortion of the Jovian Magnetosphere, *J. Geophys. Res.*, 81(25), 4561–4565, doi:10.1029/JA081i025p04561.

Huebner, W.F., Keady, J.J., Lyon, S.P., (1992), Solar photo rates for planetary atmospheres and atmospheric pollutants, *Kluwar Academic Publishing*, DOI: 10.1007/BF00644558.

Huestis, D.L., S.W. Bougher, J.L. Fox, M.Galand, R.E. Johnson, J.I. Moses, J.C. Pickering, (2008), Cross Section and Reaction Rates for Comparative Planetary Aeronomy, *Space Sci Rev* 139: 63-105, DOI 10.1007/s11214-008-9383-7.

Johnson, R.E., (2010), Photolysis and Radiolysis of Water Ice, Chapter in *Physics and Chemistry at Low Temperatures,* L. Khriachtchev (Ed.) , World Scientific, Singapore.

Johnson, R. E., P. D. Cooper, T. I. Quickenden, G. A. Grieves, and T. M. Orlando, (2005a) Production of oxygen by electronically induced dissociations in ice, *Journal of Chemical Physics,* dx.doi.org/10.1063/1.2107447

Johnson, R. E., M. Liu, and E. C. Sittler Jr. (2005b), Plasma-induced clearing and redistribution of material embedded in planetary magnetospheres, *Geophys. Res. Lett.*, *32*, L24201, doi:10.1029/2005GL024275.

Johnson, R.E., J.G. Luhmann, R.L. Tokar, M. Bouhram, J.J. Berthelier, E.C. Sittler, J.F. Cooper, T.W. Hill, H.T. Smith, M. Michael, M. Liu, F.J. Crary, D.T. Young, (2006a) Production, ionization and redistribution of O2 in Saturn's ring atmosphere, *Icarus*, Volume 180, Issue 2, Pages 393-402, ISSN 0019-1035, 10.1016/j.icarus.2005.08.021.

Johnson, R.E., Smith, H.T., Tucker, O.J., Liu, M., Burger, M.H., Sittler, E.C., Tokar, R.L., (2006b), The Enceladus and OH torus at Saturn, Astrophysical Journal, 644, doi:10.1086/505750

Jurac, S., and J. D. Richardson (2005), A self-consistent model of plasma and neutrals at Saturn: Neutral cloud morphology, *J. Geophys. Res.*, *110*, A09220, doi:10.1029/2004JA010635.

Jurac, S., and J. D. Richardson (2007), Neutral cloud interaction with Saturn's main rings, *Geophys. Res. Lett.*, *34*, L08102, doi:10.1029/2007GL029567.

Jurac, S., R. E. Johnson, and J. D. Richardson (2001), Saturn's E ring and production of the neutral torus, *Icarus*, *149*, 384–396, doi:10.1006/icar.2000.6528.

Lewis, G.R., ELS moments, Private communication (2010).

Lewis, G.R., Andre, N., Arridge, C.S., Coates, A.J., Gilbert, L.K., Linder, D.R., Rymer, A.M., (2008), Derivation of density and temperature from the Cassini-Huygens CAPS electron spectrometer, *Planetary and Space Science*, 56, doi:10.1016/j.pss.2007.12.017

Livi, R, J Goldstein, A. M. Rymer, T.W. Hill, A. D. DeJong, (2011), Electron injection and associated moment analysis in Saturn's magnetosphere, *AGU Fall Meeting* (In Progress)

Luhmann J. G., R.E. Johnson, R.L. Tokar, S.A. Ledvina, T.E. Cravens, (2006),A model of the ionosphere of Saturn's rings and its implications, *Icarus*, Volume 181, Issue 2, Pages 465-474, ISSN 0019-1035, 10.1016/j.icarus.2005.11.022

Luna, L., McGrath, M.A., Shah, M.B., Johnson, R.E., Liu, M., Latimer, C.J., Montenegro, E.C., (2005). Dissociative charge exchange and ionization of o_2 by fast H^+ and O^+ ions: energetic ion interactions in europa's oxygen atmosphere and neutral torus, *Astrophys. J.*,Vol 628, #2, doi:10.1086/431140.

Martens, H. R., D. B. Reisenfeld, J. D. Williams, R. E. Johnson, and H. T. Smith (2008), Observations of molecular oxygen ions in Saturn's inner magnetosphere, *Geophys. Res. Lett.*, *35*,L20103, doi:10.1029/2008GL035433.

Mauk, B.H., D.C. Hamilton, T.W. Hill, G.B. Hospodarsky, R.E. Johnson, C. Paranicas, E. Roussos, C.T. Russell, D.E. Shemansky, E.C. Sittler, R.M. Thorne, (2009), Fundamental Plasma Processes in Saturn's Magnetosphere, Chapter 11 in *Saturn from Cassini-Huygens* (ed. M.K. Dougherty) pp 281-331.

Melin, H., D. E. Shemansky, and X. Liu (2009), The distribution of atomic hydrogen and oxygen in the magnetosphere of Saturn, *Planet. Space Sci.*, *57*, 1743–1753, doi:10.1016/j.pss.2009.04.014.

Moses, J. I., B. Bézard, E. Lellouch, G. R. Gladstone, H. Feuchtgruber, M. Allen, (2000), Photochemistry of Saturn's Atmosphere: I. Hydrocarbon Chemistry and Comparisons with ISO Observations, *Icarus*, Volume 143, Issue 2, Pages 244-298, ISSN 0019-1035, 10.1006/icar.1999.6270.

Moses J. I., E. Lellouch, B. Bézard, G.R. Gladstone, H. Feuchtgruber, M. Allen, (2000), Photochemistry of Saturn's Atmosphere: II. Effects of an Influx of External Oxygen, *Icarus*, Volume 145, Issue 1, Pages 166-202, ISSN 0019-1035, 10.1006/icar.1999.6320.

Paranicas, C. , D.G. Mitchell, S.M. Krimigis, D.C. Hamilton, E. Roussos, N. Krupp, G.H. Jones, R.E. Johnson, J.F. Cooper, T.P. Armstrong, (2008), Sources and losses of energetic protons in Saturn's magnetosphere, *Icarus*, Volume 197, Issue 2, Pages 519-525, ISSN 0019-1035, 10.1016/j.icarus.2008.05.011.

Persoon, A.M. "RPWS densities" Private communication (2010).

Persoon, A. M., D. A. Gurnett, W. S. Kurth, and J. B. Groene (2006), A simple scale height model of the electron density in Saturn's plasma disk, *Geophys. Res. Lett.*, 33, L18106, doi:10.1029/2006GL027090.

Porco, C.C. et al., (2006), Cassini Observes the Active South Pole of Enceladus, *Science* Vol. 311 no. 5766 pp. 1393-1401 DOI: 10.1126/science.1123013

Reisenfeld, Private communication, CAPS Revised Efficiences, *CAPS Team Meeting*.

Richardson, J. D. (1986), Thermal ions at Saturn: Plasma parameters and implications, *J. Geophys. Res.*, *91*, 1381–1389, doi:10.1029/JA091iA02p01381.

Rymer, A. M., et al. (2007), Electron source in Saturn's magnetosphere, *J. Geophys. Res.*, *112*, A02201, doi:10.1029/2006JA012017.

Rymer, A. M., H. T. Smith, A. Wellbrock, A. J. Coates, and D. T. Young (2009), Discrete classification and electron energy spectra of Titan's varied magnetospheric environment, *Geophys. Res. Lett.*, *36*, L15109, doi:10.1029/2009GL039427.

Schippers, P. N. Andre, R.E. Johnson, M. Blanc, I. Dandouras, A.J. Coates, S.M. Krimigis, and D.T. Young, (2009), Identification of photoelectron energy peaks in Saturn's inner neutral torus, JGR 114, A12212, doi:10.1029/2009JA014368.

Sittler, E.C., N. Andre, M. Blanc, M. Burger, R.E. Johnson, A. Coates, A. Rymer, D. Reisenfeld, M.F. Thomsen, A. Persoon, M. Dougherty, H.T. Smith, R.A. Baragiola, R.E. Hartle, D. Chornay, M.D. Shappirio, D. Simpson, D.J. McComas, and D.T. Young, (2008), Ion and neutral sources and sinks within Saturn's *inner* magnetosphere: Cassini results, *Planet. Space Sci*. 56, 3-18. doi:10.1016/j.pss.2007.06.006.

Sittler, E.C. Jr., M. Thomsen, R.E. Johnson, R.E. Hartle, M. Burger, D. Chornay, M.D. Shappirio, D. Simpson, H.T. Smith, A.J. Coates, A.M. Rymer, D.J. McComas, D.T. Young, D. Reisenfeld, M. Dougherty, N. Andre, (2006), Cassini observations of Saturn's inner plasmasphere: Saturn orbit insertion results, *Planetary and Space Science*, 54,. doi:10.1016/j.pss.2006.05.038.

Sittler, E.C., R.E. Johnson, S. Jurac, J.D. Richardson, M. McGrath, F. Crary, D.T. Young, and J.E. Nordholt, (2004), Pickup ions at Dione and Enceladus: Cassini Plasma Spectrometer simulations, *J. Geophys. Res.* 109, A01214, doi:10.1029/2002JA009647.

Smith, H. T., R. E. Johnson, M. E. Perry, D. G. Mitchell, R. L. McNutt, and D. T. Young (2010), Enceladus plume variability and the neutral gas densities in Saturn's magnetosphere, *J. Geophys. Res.*, *115*, A10252, doi:10.1029/2009JA015184.

Teolis, B.D., J. Shi, R. A. Baragiola, (2009) Formation, trapping and ejection of radiolytic O_2 from ion-irradiated water ice studied by sputter depth profiling, *J. of Chemical Physics*, 130,pp. 134704-9, dx.doi.org/10.1063/1.3091998

Thomsen, M.F., Delapp, D.M., (2005), Numerical moments computation for CAPS/IMS, *Unpublished report for limited distribution from CAPS web page*.

Thomsen, M. F., D. B. Reisenfeld, D. M. Delapp, R. L. Tokar, D. T. Young, F. J. Crary, E. C. Sittler, M. A. McGraw, and J. D. Williams (2010), Survey of ion plasma parameters in Saturn's magnetosphere, *J. Geophys. Res.*, *115*, A10220, doi:10.1029/2010JA015267.

Tokar, R. L., et al. (2005), Cassini observations of the thermal plasma in the vicinity of Saturn's main rings and the F and G rings, *Geophys. Res. Lett.*, 32, L14S04, doi:10.1029/2005GL022690.

Tokar, R.L., R.E. Johnson, T.W. Hill, D.H. Pontius, W.S. Kurth, F.J. Crary, D.T. Young, M.F. Thompsen, D.B. Reisenfeid, A.J. Coates, G.R. Lewis, E.C. Sittler, D.A. Gurnett, (2006) The Interaction of the Atmosphere of Enceladus with Saturn's Plasma, *Science* 311, 1409-1412.

Tokar, R.L., R.E. Johnson, M.F. Thomsen, R.J. Wilson, D.T. Young, F.J. Crary, A.J. Coates, G.H. Jones, and C.S. Paty, (2009), Cassini detection of Enceladus' cold water-group plume ionosphere, *Geophys. Res. Lett.* 36, L13203, doi:10.1029/2009GL038923.

Tokar, R.L., R.J. Wilson, R.E. Johnson, M.G. Henderson, M.F. Thomas, M.M. Cowee, E.C. Sittler, Jr., D.T. Young, H.J. McAndrews, H.T. Smith, (2008), Cassini Detection of Water-group pick-up ions in Saturn's torus , *GRL* 35, L14202, doi:10.1029/2008GL034749.

Tokar, R.L., and 12 colleagues, (2005), Cassini Observations of the Thermal Plasma in the Vicinity of Saturn's Main Rings and the F and G Rings. *Geophys. Res. Lett.* 32, doi:10.1029/2005GL022690. L14S04.

Tseng, W.-L., R.E. Johnson, M.K. Elrod, Modeling the seasonal variability of the plasma environment in Saturn's magnetosphere between main rings and Mimas. *Planetary and Space Science* (2012), http://dx.doi.org/10.1016/j.pss.2012.05.001

Tseng W.-L., W.-H. Ip, R.E. Johnson, T.A. Cassidy, M.K. Elrod, (2010), The structure and time variability of the ring atmosphere and ionosphere, *Icarus*, Volume 206, Issue 2, Pages 382-389, ISSN 0019-1035, 10.1016/j.icarus.2009.05.019.

Tseng, W.-L., W.-H. Ip,(2011), An assessment and test of Enceladus as an important source of Saturn's ring atmosphere and ionosphere, *Icarus*, Volume 212, Issue 1, , Pages 294-299, ISSN 0019-1035, 10.1016/j.icarus.2010.12.003.

Virtual Solar Observatory, UCAR, Boulder, CO.

Weiss, J.W., Porco, C.C., Tiscareno, M.S., (2009). Ring edge waves and the masses of nearby satellites, *Astronomical Journal*, doi:10.1088/0004-6256/138/1/272.

Wilson, R.J. M.K. Elrod, F.Crary, Results from 2011031 MCP experiment, CAPS Team Meeting #42 , Glacier, MT.

Wilson, R.J, (2009), Interface control document for CAPS IMS Singles (SNG), private communication.

Wilson, R. J., R. L. Tokar, M. G. Henderson, T. W. Hill, M. F. Thomsen, and D. H. Pontius Jr. (2008), Cassini plasma spectrometer thermal ion measurements in Saturn's inner magnetosphere, *J. Geophys. Res.*, 113, A12218, doi:10.1029/2008JA013486.

Wilson, R. J. , M. K. Elrod, F. J. Crary, (2012) Investigations of MCP voltages changes on IMS signal, *CAPS Team Meeting*, Glacier, MT, 2012.

Wilson, R.J. et al., PDS User's Guide for Cassini Plasma Spectrometer (CAPS), (2012), PDS Planetary Plasma Interactions (PPI) Node CAPS Data Archive website

Young, D.T. et al., (2005), Composition and Dynamics of Plasma in Saturn's Magnetosphere, *Science* 307, 1262-1266 .

Young, D. T., J. J. Berthelier, M. Blanc, J. L. Burch, A. J. Coates, R. Goldstein, M. Grande, T. W. Hill, R. E. Johnson and V. Kelha, and 48 more authors., (2004), Cassini Plasma Spectrometer Investigation. *Space Science Reviews.,* 114: 1–112, 2004. DOI: 10.1007/s11214-004-1406-4.